The Cosmic Radio Dipole

Dissertation an der Fakultät für Physik der Universität Bielefeld

vorgelegt von

Matthias Rubart

Mai 2015
Supervisor: Prof. Dr. Dominik Schwarz

Gedruckt auf alterungsbeständigem Papier "DIN-ISO 9706"

To my parents.

Abstract

The velocity of the Milky Way with respect to the (at large scales) homogeneous universe seemed to be well known from observations of the cosmic microwave background. Such a peculiar motion also affects radio observations and should lead to a dipole anisotropy in number counts of radio sources. This anisotropy has been estimated in this thesis using the NRAO VLA Sky Survey and the Westerbork Northern Sky Survey. On the one hand the obtained directions agree with the expectation within the measurement uncertainties. The radio dipole amplitudes on the other hand show a significant excess, which would correspond to an increased velocity of the Milky Way with respect to those radio sources, if no other explanation can be found.

In this thesis, a general introduction to the topic is given and the relations to other scientific questions (e.g. large bulk flows) are discussed. Previous results concerning the cosmic radio dipole are presented, compared and analysed. The radio dipole is estimated by means of linear estimators, including a newly developed two-dimensional version, and the obtained amplitudes are analysed in detail. Certain issues (i.e. shot noise contributions) of the linear estimator are revealed and the effects of masking sources and calibration errors on the dipole estimation are discussed.

A quadratic estimator was developed and the radio dipole was re-obtained, refining the results from linear estimators. It is shown that the quadratic estimator has many advantages compared to the linear ones. The quadratic estimator is more stable w.r.t. masking effects and reveals new insights concerning the dipole in radio surveys. For example the radio sky cannot be described well by a mono- and dipole term alone.

In a final step the effect of local structures ($z \ll 1$) on the dipole estimation is investigated. For example, the effect of a local void contribution on the dipole amplitude is analysed. Such structures may reduce the discrepancy between the dipole in radio and microwave observations. At the end, all obtained results are compared and discussed.

Cosmological notation

a	scale factor
H_0	Hubble constant
h	Hubble parameter
t	cosmological time
t_0	age of the universe
d_l	luminosity distance
Ω_m	matter density relative to critical density
Ω_b	baryon matter density relative to critical density
Ω_c	cold dark matter density relative to critical density
Ω_Λ	vacuum energy density relative to critical density
Ω_k	curvature parameter
z	redshift
$f_{\rm baryon}$	baryon fraction
σ_8	density fluctuation at 8 h^{-1} Mpc
$n_{\rm scalar}$	density fluctuation spectral index
τ	optical depth
G	gravitational constant

Used acronyms

AGN	Active Galactic Nucleus
ASTRON	ASTRonomisch Onderzoek in Nederland
CiS	Catalogue in Spherical coordinates
	Cosmic Microwave Background
FR I & II	Fanaroff and Riley class I & II
GC	Galactic Center
GN	Galactic North pole
HBA	High-Band Antenna
LBA	Low-Band Antenna
LOFAR	LOw Frequency ARray
ΛCDM	Λ (cosmological constant) Cold Dark Matter
NVSS	National radio astronomy observatory VLA Sky Survey
MSSS	Multi-frequency Snapshot Sky Survey
SF	Star Forming galaxy
SKA	Square Kilometre Array
SKADS	European Square Kilometre Array Design Study
S^3	SKADS Simulated Skies
VLA	Very Large Array
WENSS	WEsterbork Northern Sky Survey
WSRT	Westerbork Synthesis Radio Telescope

Contents

Chapter 1

Introduction

> *The trouble with having an open mind, of course, is that people will insist on coming along and trying to put things in it.*
>
> — Terry Pratchett, Diggers

Some of the most interesting questions in physics are those, which have counterintuitive answers. Human intuition is based on our everyday experience here on Earth. We all do have an idea of the concept called velocity. For instance when we ride a bicycle, we experience the wind in our hair, we see the land passing by and we hear the tires rolling in the street. When we ride faster, we cover more distance in shorter time intervals. There is a certain difference between going with 30 km/h and 15 km/h or even standing still. From this practical experience one would expect to be able to assign an absolute velocity to an observer. After all that seems to be what a tachometer does.

It turns out that the situation is slightly more complicated. The velocity of an object is the change of its position in a certain time interval, which can be measured with some clock. But in order to be able to measure the change of position we need a coordinate system. Such a coordinate system consist of an origin and (for example) three axes, pointing in different directions. Now we can measure the change in position of the object relative to this coordinate system. In the above example the velocity of the bike relative to the road, which corresponds to a coordinate system, was measured. But this coordinate system is not unique, since one could imagine using various different coordinate systems. The critical point now is that those coordinate systems can have a relative velocity to each other. In this case, the object's velocity relative to the first coordinate system may differ from the velocity measured with the second one. Hence, one cannot assign a unique velocity, independent of the coordinate choice, to any object.

Therefore apprentices of physics learn that the concept of velocity only has some meaning when it is combined with a reference frame. An appealing idea is, to define a special reference frame for all velocity measurements and thereby obtain a kind of absolute velocity notion. Something like the Earth's centre or the Sun could define such a frame, but typically physicists search for the most general concepts and so a universal frame should not be based on our position in the Universe.

1.1 Cosmic microwave background

In 1964 the Cosmic Microwave Background (CMB) was discovered by Arno Penzias and Robert Wilson (Penzias & Wilson 1965). They found radiation coming from every direction on the sky, presenting photons obeying an almost perfect black-body spectrum of roughly 3 Kelvin. Today we recognize this radiation as a kind of echo from the very early universe, when it was roughly 3×10^5 years old. At that time the content of the universe was so hot that neutral atoms were not stable. The universe consisted of plasma, which was in thermal equilibrium. Due to its expansion, the universe cooled down and at some point the positively charged nuclei (consisting of protons and neutrons) combined with the negatively charged electrons to form atoms which are neutral overall. This process is called recombination (even so, these atomic components have never before been combined). After this recombination, the photons decoupled from the thermally equalized plasma and began to travel freely through the transparent universe. Today we can observe this background radiation coming from the very edge of the observable universe. After a four-year observation with the COBE satellite, the NASA published a picture of the CMB, shown in figure 1.1.

We can see here that the temperature of the CMB, inferred from the temperature of the corresponding black body spectrum, is not isotropic. The main anisotropy is of order 3.4 mK or 0.1% and has the form of a dipole modulation, with two extreme values at opposite directions on the sky. Between the maximum and the minimum value, the temperature

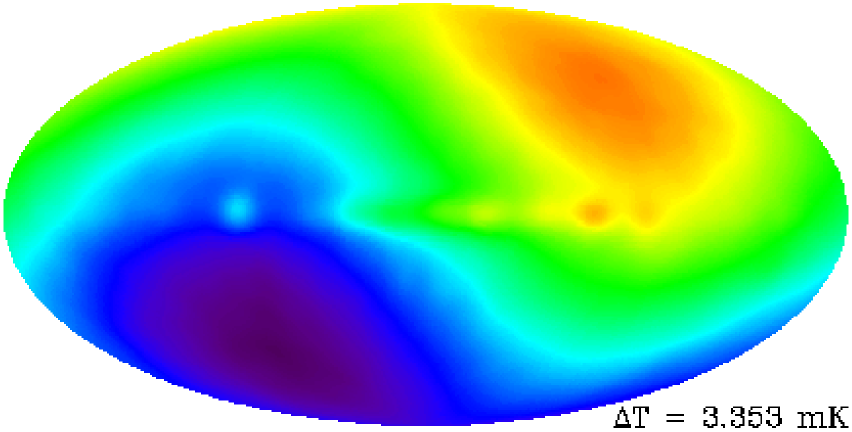

Figure 1.1: CMB dipole anisotropy projected on the full sky in galactic coordinates. [Obtained from COBE Four-Year Sky Map, http://lambda.gsfc.nasa.gov, Bennett et al. (1996)]

amplitude difference varies like a cosine. This dipole effect was first seen by Conklin (1969) and it was quite surprising at that time. One expected the early universe to have been in thermal equilibrium, which would lead to isotropic background radiation. Fortunately there is an explanation of this observed dipole anisotropy that still allows a thermally equalized early universe.

The CMB is observed from our solar system, which can have some relative velocity to the CMB. Such a velocity would lead to a Doppler effect, which would be seen as a dipolar modification on an isotropic background. If we now assume that the CMB dipole is purely due to our kinetic velocity, one can calculate how large this velocity needs to be. Therefore on uses the equation derived by Peebles & Wilkinson (1968):

$$T(\theta) = \frac{T_0}{\gamma(1 - \beta \cos\theta)} \approx T_0(1 + \beta\cos\theta) \ , \tag{1.1}$$

with β and γ being the usual relativistic velocity parameters, θ the angle between the observed direction and our kinetic velocity and T_0 the mean temperature of the CMB. This was done with every new CMB sky map

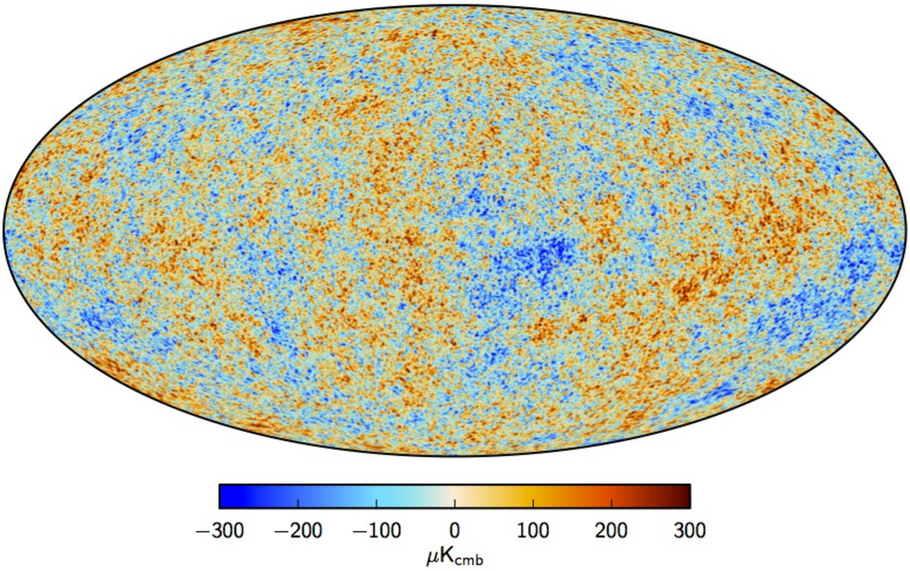

Figure 1.2: CMB as seen by Planck in galactic coordinates with dipole anisotropy and foreground removed. [source: Planck Collaboration et al. (2015a)]

release at an increased precision, most recently by Planck Collaboration et al. (2015b) and the obtained velocity is $v = 370.5 \pm 0.2$ km/s. After this dipole effect is removed from the CMB map, one can observe an higher temperature exactly in the area, which is covered by the Milky Way. This imprint of our own galaxy can also be removed. These two steps were also performed for the most recent observation of the CMB, which is shown in figure 1.2.

Here we can see very small temperature fluctuations, which are of order 10^{-5}. It turns out that this map is of great importance for cosmology, since it can be used to measure many parameters of today's model of the universe. In a recent work of the Planck team (Planck Collaboration et al. 2014a) the temperature power spectrum, up to the 2500th multipole, has been calculated from those anisotropies. To this power spectrum our cosmological model was fitted and, besides others, the Hubble constant H_0, the baron matter density Ω_b, the cold dark matter density Ω_c as well as the curvature parameter Ω_k have been measured. Some other parameters, like the dark energy density Ω_Λ or the age of the universe t_0, can be derived from those parameters.

Of course some of those parameters can also be evaluated by different observations and methods. On the other hand, there is no alternative single observation, which can deduce so many important parameters, with such high precision. Hence, the CMB plays an outstanding role for modern cosmology. But there is one weakness in this line of thought. The CMB dipole is assumed to be caused by our relative velocity and until now we do not have an independent confirmation of this assumption. It is very important to be aware of this, since the velocity measured by the described method is used in a variety of other cosmological investigation.

There is however a way to test this assumption within the CMB itself. The dipole affects the CMB map on a magnitude of order 10^{-3}. So far we only discussed the Doppler-effect on the CMB average temperature, but there are also higher multipoles in the CMB and all those higher multipoles should be affected in the same way, if the dipole is due to the observer's motion. Since those higher multipoles are of order 10^{-5}, it is very challenging to search for a per mille effect on top of those. The first satellite with the ability to perform this search is the Planck satellite and the corresponding collaboration was able to find a dipole effect on higher multipoles, which has a direction in agreement with the CMB dipole and an obtained velocity of 384 km/s ± 78 km/s (stat.) ± 115 km/s (syst.) (Planck Collaboration et al. 2014c). This result is in good agreement with the velocity from the main dipole anisotropy and hence supports the discussed assumption. Unfortunately a final conclusion cannot be made yet, since the error bars of this measurement are too large.

1.2 Large-scale structure

As discussed above, the velocity of our solar system relative to the CMB is inferred from the dipole anisotropy in this background radiation. Removing the dipole contribution in the CMB, results in a very isotropic background, seen by an observer in the so-called CMB rest frame.

The Copernican Principle states that we do not live in a special place in the Universe. If this holds true, not only Earth-based observers, but also other observers throughout the universe should see isotropic background radiation, as long as the peculiar velocity of the observer relative to the CMB is corrected for. When the background radiation is isotropic for every typical observer, then it must be homogeneous throughout the universe (Maartens 2011). Hence, the universe is modelled with an isotropic and homogeneous space-time in cosmology.

It was discovered by Slipher (1917) that the great majority of nearby galaxies is redshifted. Due to the Doppler-effect, these redshifts are interpreted as relative velocities w.r.t. an Earth-based observer, pointing outwards. The velocities increase with distance, described by the famous Hubble law (Hubble 1929):

$$H_0 \; d_l = v \; , \tag{1.2}$$

with H_0 being the Hubble constant today [$H_0 = 67.8 \pm 0.9$ km/s/Mpc, Planck Collaboration et al. (2015c)], d_l the luminosity distance to an object with relative velocity v. This Hubble law is easily obtained, when we assume an expanding Universe and holds for nearby sources ($d_l \ll c/H_0$). Due to this assumption we describe the Universe with a space-time metric that is not constant, but features a time-dependent scale factor $a(t)$. This factor describes the observed stretching, by increasing typical distances (e.g. between different galaxies) with time. Any motion relative to this background space-time, after the cosmic expansion is subtracted, we call peculiar velocity (in practice the peculiar velocity is taken w.r.t. the CMB rest frame).

The observed peculiar velocities of various objects are most likely caused by the gravitational pull of inhomogeneous matter distribution on the scales of galaxy clusters. Such a pull will lead to an acceleration of matter towards areas with increased density. This acceleration $\vec{g}$ was determined in the book of Peebles (1980) to be

$$\vec{g} = Ga \int \mathrm{d}x'^3 \; \rho(\vec{x}') \frac{\vec{x}' - \vec{x}}{|\vec{x}' - \vec{x}|^3} \; , \tag{1.3}$$

where $\rho(\vec{x}')$ is the matter density at the co-moving coordinate $\vec{x}'$, G the gravitational constant and a the scale factor of the Universe today. This equation implies that an object is accelerated towards nearby matter conglomerations.

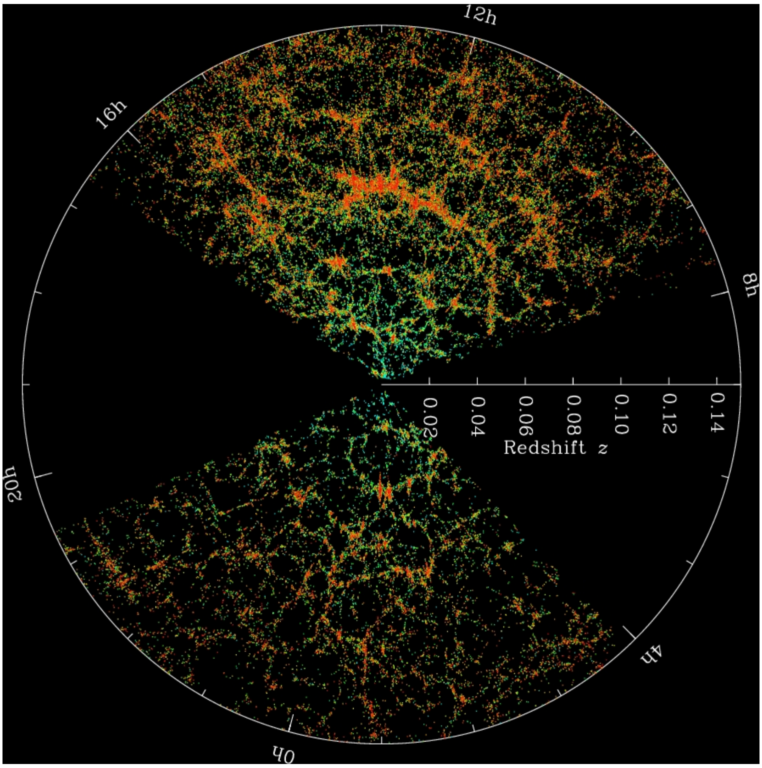

Figure 1.3: Map of the galaxy distribution obtained by the Sloan Digital Sky Survey (SDSS), showing galaxies at different redshift distances, [source: www.sdss.org, March 2015, (Ahn et al. 2014)]

Of course, the Universe is not perfectly homogeneous on all scales. The Earth, the solar system and the Milky Way are examples of inhomogeneous places inside a Universe that can be considered statistically homogeneous on its largest scales (i.e. of orders $z > 0.1$) only. In figure 1.3 we see the distribution of galaxies in a part of the local Universe. Noteworthy are the filaments of clustered galaxies as well as the empty regions in between, which are called voids. The largest mass accumulations are called superclusters, consisting of up to hundred thousand individual (large) galaxies.

It is not obvious, how to define the boundaries of such a cluster. For the local supercluster, which contains the Milky Way, a new method has been applied by Tully et al. (2014). They defined the local supercluster not by regions of connected increased density, since it is hard to define where the boundaries of such a region are, due to the filamentary structure shown in figure 1.3. Instead they studied the peculiar velocities of nearby galaxies listed in the Cosmicflows-2 catalogue (Tully et al. 2013). Regions with infalling galaxies are considered to be gravitational bound and will therefore be defined as a bound large-scale structure. In this way they defined the Laniakea supercluster of galaxies, which contains about 10^{17} solar masses (including the Milky Way and the Virgo cluster) and has a diameter of about 160 Mpc (Tully et al. 2014).

Outside the Lineakea supercluster, further matter accumulations can be found, like the Shapely concentration. This supercluster lies, from our point of view, approximately behind the central region of the Lineakea supercluster. Therefore we expect the gravitational pull of both structures to add up and cause the acceleration of the Local Group (consisting of the Milky Way, the Andromeda Galaxy and nearby dwarf galaxies) towards that direction. The Shapely concentration lies at the galactic coordinates $(l, b) = (305°, 30°)$ (Einasto et al. 1997), which is close to the direction found for the CMB dipole: $(l, b) = (264°, 48°)$ (Planck Collaboration et al. 2015b).

There are three main contributions to the motion which we observe w.r.t. the CMB rest frame. First of all the Earth is moving around the sun with a velocity of approximately 30 km/s. The direction of this velocity varies with the year and is usually removed before data are analysed further (for the CMB it is used to calibrate the observations). It is also an order of magnitude smaller than the two following contributions. The Sun is on an orbit around the centre of the Milky Way with a velocity of about 200 km/s (Sparke & Gallagher 2000), and this centre is also moving with respect to the Local Group. Usually all those effects are combined and the velocity of the Sun relative to the Local Group has been found to be about 306 km/s towards the galactic coordinates $(l, b) = (99° \pm 5°,\ -4° \pm 4°)$[Gibelyou & Huterer (2012) using Maller et al. (2003) and Courteau & van den Bergh (1999)].

Finally, the Local Group has some velocity with respect to the CMB. In order to calculate a value of this velocity, it is necessary to consider the previously mentioned velocities. Doing so leads to a velocity of the Local Group of approximately 622 km/s towards $(l, b) = (272°, 28°)$ [Maller et al. (2003) and Gibelyou & Huterer (2012)]. This direction is even closer to the Shapely concentration than the pure CMB dipole direction. It is interesting to mention that the velocity of the Sun relative to the Local Group is almost opposite to the velocity of the Local Group with respect to the CMB.

1.3 Large bulk flows

Large bulk flows in the universe are measured using the following principle. First the peculiar velocities of a large number ($\mathcal{O}(10^4)$) of nearby galaxies are determined and catalogued. Creating such a catalogue is highly non trivial, since various methods must be used to obtain the peculiar velocities of such a large number of galaxies. Due to the expansion of the universe one cannot just use the redshift of individual galaxies, since this is always a combination of the peculiar velocity and the cosmic redshift. Therefore one also needs to measure the distance to such a galaxy with a redshift-independent method. For example in the Cosmicflows-2 catalogue (Tully et al. 2013) six distinct methods to measure those distances are used. Two examples are the Cepheid period-luminosity relation (Freedman et al. 2001) and the luminosity-linewidth correlation for spirals (Tully & Fisher 1977). Hence, one must be very careful to avoid any bias between the different methods in order to obtain a uniform survey. The distances of some galaxies can be measured with more than one method. This helps to ensure that the results of different methods are in good agreement and in some cases one method can be used to calibrate another.

When distance and redshift of an individual galaxy are known, one can calculate its peculiar velocity. Two modifications for the direct redshift measurement are needed. The first one is due to the peculiar motion of every Earth-based observer relative to the CMB. After removing this effect, one obtains the redshift as seen in the CMB-frame. The second effect comes from the fact that the universe is expanding and thereby red-shifting all photons travelling through space. In order to remove this effect, one needs to assume a specific cosmological model, describing the cosmic expansion. So the two main assumptions used here are: the cosmological model and the peculiar velocity of Earth relative to the CMB.

If the velocity of the solar system relative to the CMB has not exactly the value one obtains via the dipole anisotropy, then this error propagates to the peculiar velocity estimation of the mentioned galaxies. A significant contamination of the bulk flow studies would be the result.

From a peculiar velocity catalogue one can measure, whether the local universe (on scales up to $100h^{-1}$ Mpc) is in some kind of combined motion towards a certain direction or obtain an upper limit on such a movement. Very large bulk flows ($\approx 400 \pm 80$ km/s) have been reported (Watkins et al. 2009) in recent years, which challenges the cosmological model. Another investigation (Watkins & Feldman 2015), using the Cosmicflow-2 catalogue (Tully et al. 2013), resulted in a smaller bulk flow velocity ($\approx 290 \pm 60$ km/s). This second result is not inconsistent with the ΛCDM model, but still rather large (the chance of finding the reported bulk flow is of order 10% according to Watkins & Feldman (2015).

Kalus et al. (2013) measured an anisotropy in the local Hubble rate of $\Delta H/H = 0.026$, by investigating type Ia supernovae. For a length scale of $100h^{-1}$ Mpc, this corresponds to an anisotropy in velocities of about $v_\Delta = 260$ km/s, which is the same order of magnitude as bulk flows that have been reported. Due to rather large statistical and systematically uncertainties, this topic is not resolved yet. In any case it shows that we do not fully understand the motions in our local universe.

Another method to investigate movements through the universe is the kinetic Sunyaev-Zeldovich effect (kSZ). We observe the CMB photons after they travelled through the universe since recombination. On their way they can interact with normal matter. The kSZ describes the interaction between the CMB photons and electrons with high coherent velocities (v_{bulk}) relative to the CMB. This happens with increased likelihood in clusters of galaxies that are moving with some peculiar velocity relative to the CMB. In the end the kSZ leads to a change of temperature in the CMB along the line of sight of such a cluster and thereby one obtains a dipole term $C_{1,\mathrm{kin}}$ in the power spectrum of [Kashlinsky et al. (2008) and Birkinshaw (1999)]

$$C_{1,\mathrm{kin}} = T_{\mathrm{CMB}}^2 \langle\tau\rangle v_{\mathrm{bulk}}^2 / c^2 \ , \tag{1.4}$$

with $\langle\tau\rangle$ being the expected optical depth of the galaxy clusters. Note that this method does not depend on the observer's velocity, but only on the velocities of clusters w.r.t. the CMB.

One can observe the temperature fluctuations in the CMB at the cluster positions and from this obtain the velocity of those clusters relative to the background. If this movement is on length scales of about $100 - 600\ h^{-1}$ Mpc and shows a coherent movement of the observed clusters through the universe, then one calls it a dark flow (similar to the previous bulk flow, but on larger scales). Osborne et al. (2011) studied this effect in the WMAP seven-year data, resulting in an upper limit of 3485 km/s (95% confidence) for the dark flow.

In a more recent work Atrio-Barandela et al. (2014) claim to have found such a dark flow in WMAP nine-year and Planck maps, with an amplitude of 800 ± 200 km/s and aligned with the CMB dipole axis. Such a high value of the dark flow would be in tension with the assumption of a homogeneous universe. The Planck collaboration on the other hand, was not able to find a significant kSZ (Planck Collaboration et al. 2014b) in the same data set. Therefore the issue of a possible dark flow through the universe is also not resolved yet.

To conclude, there are interesting hints towards unknown effects concerning large-scale motions in our universe. If the reported large bulk flows turn out to be valid, the local universe would not be at rest with the CMB. In this case further peculiar velocity measurements of our galaxy with respect to other sources become important. Most radio galaxies are beyond the so-called local universe, but still at much smaller distances than the distance to the last scattering surface (CMB). Hence, they provide an ideal opportunity, to probe the transition between those large bulk flows and a universe at (statistical) rest.

1.4 Dipoles at other wavelengths

The described peculiar velocity of the Earth relative to the CMB rest frame should also affect other extragalactic observations, not only on the microwave background. We need to look for objects, which do not participate in the coherent motion of the Local Group, in order to see the impact of this motion. Also one needs to keep in mind that the dipole effect in the CMB is of order 10^{-3} only. Hence, we expect a similar order of magnitude for the effect in other observations. Therefore it may be hard to see the dipole pattern at all, since the nearby universe is not perfectly homogeneous and other anisotropies can hide the dipole pattern arising from our peculiar velocity.

Some attempts to find the kinetic dipole in other observations can be found in the literature. In this section we will focus on studies in the γ-ray and infrared bands. The kinetic dipole signal in the infrared background has been investigated for example in Fixsen & Kashlinsky (2011). They used the COBE FIRAS (Fixsen et al. 1996) and the DIRBE (Hauser et al. 1998) datasets for their work. Unfortunately both datasets suffer from galactic foreground and dust contamination. Therefore it is not possible yet to determine a kinetic dipole in the infrared background. Future observations will be able to solve this problem. This outcome for the infrared background needs to be distinguished from the infrared point-source studies, discussed in the following passages.

Previous works on infrared point-source catalogues, i.e. by Rowan-Robinson et al. (2000), resulted in a dipole amplitude and direction in good agreement with the CMB expectation. Due to possible bulk flows (see chapter 1.3) and revealed large cosmic structures (see chapter 1.2), those results may be based on observations on too small scales (most sources are at distances of order 100 h^{-1} Mpc). Hence, the following more recent studies, utilizing deeper surveys, are superior in this aspect.

In Gibelyou & Huterer (2012) four different surveys were analysed. Two of those are in the infrared band, namely the 2MASS (Skrutskie et al. 2006) and the 2MRS (Huchra et al. 2012) surveys. Both are point-source surveys, including stars and galaxies from the vicinity of our local group (up to a redshift of about $z = 0.2$). The 2MRS is a subsample of the 2MASS catalogue, also including redshift information of the observed sources. In both cases the main challenge is to separate the contribution of the kinetic dipole from the local structure effects. Since the universe is only on the largest scales isotropic, any local ($z < 1$) observations will also include a dipole contribution from the anisotropic matter distribution. Gibelyou & Huterer (2012) concluded that the measured dipole in both catalogues may be dominated by such a structure term. This issue is still present in their updated work Yoon et al. (2014), using the WISE catalogue (Wright et al. 2010). Since this new survey is significantly deeper, the local structure contribution went down by a factor of about 2.5. Unfortunately the WISE catalogue is still too shallow for probing the kinetic dipole independently.

Another wavelength investigated in Gibelyou & Huterer (2012) is the gamma-ray band. They used the BATSE (Paciesas et al. 1999) catalogue, which is a survey of gamma-ray bursts (GRB). Here the main problem is the limited amount of observed bursts (2702). Hence, the BATSE catalogue does not provide enough data points in order to separate the dipole from shot noise. Future GRB surveys with more sources may allow for a detection of the kinetic dipole within the γ-ray band. The investigation of a radio survey from Gibelyou & Huterer (2012) will be discussed in detail in section 2.

1.5 Origin of cosmic radio signals

This thesis is about the dipole anisotropy in extragalactic radio continuum surveys and therefore we need to discuss what kind of radio signals we can observe from Earth and why it is a sensible idea to use those to find the kinetic dipole signal. The following brief introduction to radio astronomy is based on the books of Burke & Graham-Smith (2010), Sparke & Gallagher (2000) and Jones & Lambourne (2003).

Assume we would be able to look with our eyes at the night sky observing radio frequencies, then we would see a completely different sky compared to the optical one. A typical star is not emitting very much radio signals, so we would see much less of the stars of our own galaxy. The sun is, compared to what we know from optical astronomy, not so bright that it outshines every other star on the sky during the day. Also the Rayleigh scattering (responsible for the blue colour of the daylight sky) is much less effective at the long radio wavelengths, so the radio sky basically stays dark for the whole day.

When looking at the sun with a radio telescope one notices two features that differ essentially from optical observations. The sun seems bigger and does not have an (almost) perfect circular disc. Actually the form of the sun even changes over time, when observed with radio telescopes. This is because in radio wavelengths the corona of the sun is brighter (since it has a higher temperature) than the sun's surface. So we actually see the atmosphere surrounding the sun, in contrast to optical astronomy.

When looking at the radio sky we will see some unusual shapes. It turns out that some galaxies are very strong radio emitters that outshine the stars of our own galaxy by far. Those very bright radio galaxies usually

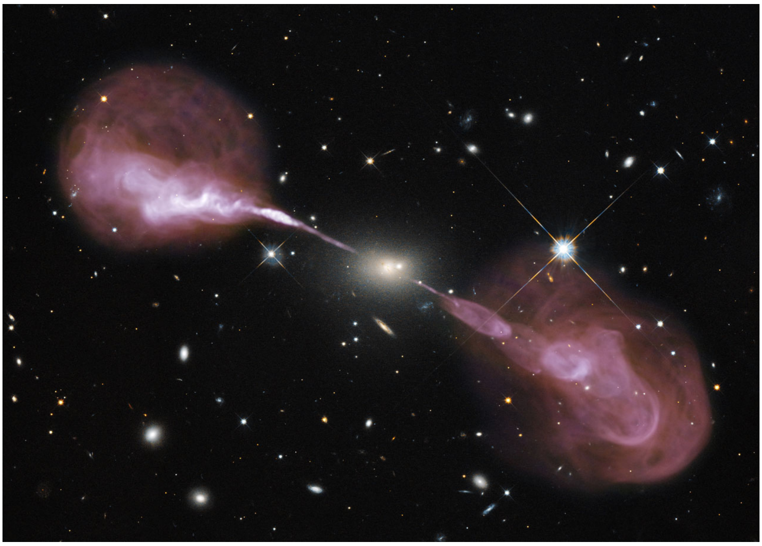

Figure 1.4: Hercules A, combined optical (Hubble Space Telescope) and radio (JVLA) observation. [source: https://public.nrao.edu/gallery/supermassive-blackholes/image?id=857, March 2015]

have one or two lobes and can be found in a variety of shapes. One example can be seen in figure 1.4. When comparing such a radio source with optical images, one finds that the point in the middle (the place where the lobes seem to be emitted) is in the centre of the corresponding galaxy. The lobes are so huge, that they are typically even bigger than the host galaxy, defined by their accumulation of stars.

This first class of radio galaxy is called Active Galactic Nuclei (AGNs). The nucleus is the central engine powering the radio lobes. It can be shown that the AGN produces so much energy that the underlying process cannot be atomic fusion, like it is the case for stars. Hence, it is assumed that the central engine is powered by the gravitational energy of matter falling towards a black hole. In this process the matter falling in heats up and becomes plasma. Now some of the electrons have enough energy to leave the central area while the remaining atomic nuclei keep on falling towards the black hole, since they are more massive.

By some process that is not yet fully understood, the escaping electrons are cumulated into beams. In the outer regions of the host galaxy those electron beams interact with the intergalactic medium. They are captured by magnetic fields and thereby emit radio signals. Those radio signals can then be observed from Earth and the radio galaxies can be classified into two different subgroups. The more common one is called Fanaroff Riley I (FRI) (Fanaroff & Riley 1974) and contains AGN where the main radio emission happens close to the central engine and falls off with increasing distance to the centre. In Fanaroff Riley II (FRII) class galaxies, the outer regions of the lobes emit more radio signals than the central area.

These AGN-powered radio galaxies have two features relevant for this work. They are rather rare and very bright [Cygnus A has an absolute magnitude in radio of $(3.14 \pm 0.78) \times 10^{36}$ W , Braude et al. (1969)] and can therefore be observed from very large distances (compared to optical astronomy). Most know optical galaxies, when observed at radio frequencies, just look like normal galaxies, without any lobes. The radio emission in those galaxies comes from synchrotron radiation, created by highly energetic electrons accelerated in magnetic fields. In contrast to AGNs, the number of those electrons in normal galaxies is relatively small and they are not concentrated in beams, but randomly distributed. Hence, they are not as bright in radio frequencies as the AGN type and can therefore only be observed at smaller distances. On the other hand, most galaxies do not have a powerful central engine and do therefore count as normal radio galaxies.

Among those normal galaxies, there are some with a relatively high number of stars that are very young and still in the process of formation. Active star-forming regions inside a galaxy emit an increased amount of radio and infrared emission. This is due to the fact that a lot of interstellar gas is present in those star-forming regions. The interstellar gas is heated up by the young stars and emits the absorbed energy again at longer wavelength. This is in principle happening in all galaxies, but only in some galaxies those regions are large and active enough to produce a significantly increased radio emission. In order to distinguish them from normal galaxies one talks about starburst galaxies (SBG). They can be observed up to an intermediate range between normal and AGN-type galaxies. Some galaxies are called radio quiet AGN. Those are AGNs, which are less bright than the FRI and FRII galaxies, but do show the same kind of lobe structures.

They are still brighter than normal galaxies, meaning they are only quiet compared to the earlier discovered radio-loud AGNs.

1.6 Radio instruments and surveys

There exist a number of radio telescopes around the world. I will describe in this section those that are relevant for my work, since they produced radio surveys that were used for the dipole analysis or are expected to produce such surveys in the future. All those telescopes are radio interferometers, which means they are consisting of a number of interconnected radio antennas.

Figure 1.5: The Westerbork Synthesis Radio Telescope. [source: http://www.astron.nl/sites/ astron.nl/files/cms/ luchtfoto-WSRT.jpg, April 2015]

The Westerbork Synthesis Radio Telescope (WSRT) can be seen in figure 1.5. One can see the line of radio dishes along the east-west orientation on this photograph. This interferometer consists of 14 radio dishes, each with a diameter of 25 meter. Four of those dishes can be moved on rails and thereby vary the distance between the different telescope parts. The telescope is located in Westerbork (NL) and operated by ASTRON, the Netherlands Institute for Radio Astronomy.

This telescope was used to create the Westerbork Northern Sky Survey [WENSS, Rengelink et al. (1997)], which actually stands for two catalogues at different frequencies (609 MHz and 325 MHz). In both cases the so-called mosaicing technique was used, which means that 80 different fields across the sky were observed and later combined. The larger catalogue includes radio sources with a declination above 30°. The flux of the detected radio sources goes down to 18 mJy and the used frequency for this part of the survey is 325 MHz. The whole catalogue contains about 230,000 sources.

The Very Large Array (VLA) is in many ways similar to the WSRT. It also consists of a number of individual 25-meter radio dishes. All in all there are 27 dishes mounted on rails for this interferometer. They are not all arranged in one line, but form a kind of three-spiked star (see figure 1.6). The VLA is located in a desert in New Mexico, USA. The array can be used in a number of different configurations, depending on how far the individual dishes are moved apart.

Figure 1.6: The Very Large Array in New Mexico. [source: http://images.nrao.edu /Telescopes/VLA/307, April 2015]

The VLA was used to create the NRAO VLA Sky Survey [NVSS, Condon et al. (1998)], which is a catalogue of radio sources with declination values above −40°. This survey was observed at a frequency of 1.4 GHz and contains almost two million sources down to a flux of 2.5 mJy. Unfortunately the survey is not complete down to this limit, which means that not all sources with flux $S > 2.5$ mJy where identified due to various limitations (e.g. noise). It is assumed that this survey is (almost) complete for all sources above 15 mJy (Condon et al. 1998). Due to observational limitations some additional identification problems arise near the galactic plane as well as near very strong radio sources.

More than $200,000$ individual images were taken with the VLA, which were later combined to create the whole NVSS catalogue. For declinations below −10° and above 80° the DnC configuration of the array was used, while between those declinations the array was in the D configuration. This comes from the fact that it is harder to observe radio objects near the horizon of the telescope. In order to compensate this problem to some extent the DnC configuration was used for the most North and South areas

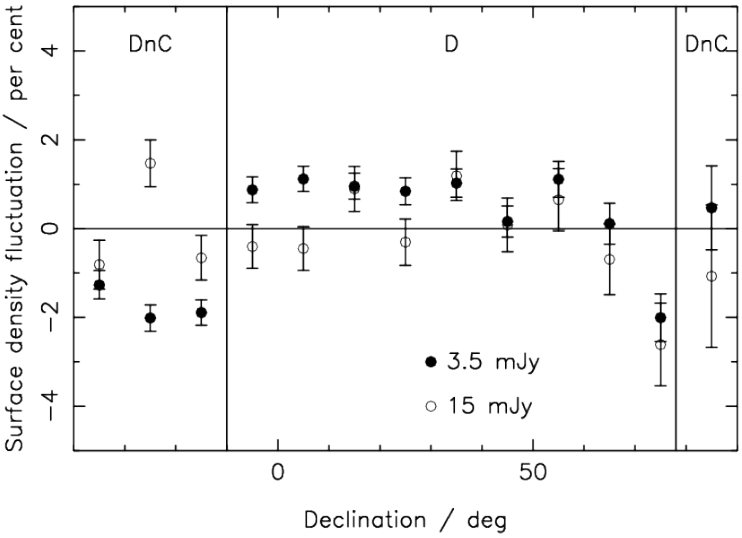

Figure 1.7: Surface density fluctuation versus declination for the NVSS catalogue in both (D & DnC) configurations for the flux limits of $S = 3.5$ mJy & $S = 15$ mJy [source: Blake & Wall (2002)].

of the survey.

For the purpose of this work it is very important to avoid any statistical bias between those two configurations. This issue was addressed by Blake & Wall (2002) and their result is shown in figure 1.7. For a lower flux limit of 3.5 mJy, one can see clearly that the surface density is smaller for the DnC configuration at declinations below $-10°$. Such an anisotropic surface density creates an artificial dipole in the catalogue. When the lower flux limit is raised towards 15mJy this effect is reduced. But one can still see a larger fluctuation at the low declination values. Blake & Wall (2002) concluded that for a dipole analysis one needs to use flux limits above 15 mJy.

Between 2001 and 2012 the electronics of the VLA were upgraded. Among others things the correlator of the telescope was replaced by a state-of-the-art version. With this new hardware the VLA was initially called Expanded VLA (EVLA) until it was renamed in 2012 to become the Karl G. Jansky Very Large Array (JVLA), after the famous radio astronomer. The new JVLA has an increased sensitivity (10 times better than the VLA) and is now able to cover the whole frequency range of 1 GHz to 50 GHz.

The most modern radio telescope in Europe is the LOw Frequency ARray (LOFAR). This interferometer operates at 10 – 80 MHz (Low-Band Antennas, LBA) and 110 – 240 MHz (High-Band Antennas, HBA), which is at the lower end of the atmospheric radio window. Most stations are located in the Netherlands, including the core station near Exloo. At the end of 2014 the sixth German station near Hamburg began its operation. This station belongs to the universities of Hamburg and Bielefeld together and improves the interferometer significantly, by filling a gap in the so-called u-v plane.

Figure 1.8: Operational LOFAR stations in Germany. [source: http://www.mpifr-bonn.mpg.de/lofar, March 2015]

Combined with the international stations in Sweden, Great Britain and France, the LOFAR radio interferometer includes baselines of order 1000 km, resulting in a possible total resolution in the subarcsecond regime (Varenius et al. 2015).

The LOFAR is one of the pathfinder telescopes for the Square Kilometre Array (SKA). This planned array will be constructed in two distinct areas, one in South Africa and one in Australia. The construction is divided into two phases, with the second phase starting after the first one is finished. The Australian part of the telescope is called SKA LOW, since it operates at 50 – 250 MHz. The first phase of this part is named SKA1 LOW and will consist of about 130,000 antennas, spread over an area of 0.4 km^2. Compared to LOFAR, this first phase of SKA LOW will already have an increased resolution by 25% and the sensitivity will be 8 times higher.

In South Africa the first phase is called SKA1 MID, operating between 350 MHz and 14 GHz. It will consist of 200 dishes, each with a diameter of 13.5 m. Compared to the JVLA, SKA1 Mid will have 4 times higher resolution and 5 times the sensitivity. The construction of this impressive instrument is planned to start in 2018. Already the first phase will improve radio observations of the sky by an order of magnitude and hence we can expect new insights in various scientific questions.

1.7 Cosmic radio dipole

This section highlights the most important works concerning the dipole anisotropy in radio surveys in chronological order. The first work in this field was made by Ellis & Baldwin (1984). They calculated the effect, peculiar motion of the Solar System with respect to the rest of the universe has on radio source catalogues. Their main result is that the radio source counts $dN/d\Omega$, for sources with fluxes above a certain limit $S > S_{\text{Limit}}$ at a fixed frequency ν and a peculiar solar velocity v (much smaller than the speed of light c), across the sky will to first order in $\frac{v}{c}$ behave like

$$\frac{dN}{d\Omega}_{\text{obs}} = \left(\frac{dN}{d\Omega}\right)_{\text{rest}} [1 + d\cos(\theta)] \,, \tag{1.5}$$

where d is the amplitude of the kinetic radio dipole and θ is the angle between the line of sight on the sky and the direction of our peculiar motion. The amplitude of this dipole modulation turns out to be

$$d = [2 + x(1 + \alpha)] \left(\frac{v}{c}\right) \,. \tag{1.6}$$

Here x is the power law index of the radio number counts (usually $x \approx 1$ is assumed) and α is the mean spectral index (defined by $S_{\text{source}}(\nu) \propto \nu^{-\alpha}$) of the radio sources (approximately $\alpha \approx 0.75$). A detailed derivation of those equations can be found in section 2.1. In equation (1.6) we can plug in the peculiar velocity derived from the CMB (370.5 km/s) and the mean values mentioned above. From those assumed values for x and α we get an expected radio dipole amplitude of $d = 4.6 \times 10^{-3}$.

Ellis & Baldwin (1984) also made the first attempts to measure this dipole in radio catalogues. The 4C (Pilkington & Scott (1965), about 5000 sources at 178 MHz) catalogue was used, resulting in a dipole amplitude of $(5.6 \pm 3.2) \times 10^{-2}$, which is above the expected value. Because the error bars are so large (due to shot noise), no significant tension with the CMB expectation can be asserted (note that the $d = 0$ case is within their two-sigma boundaries). In order to obtain stricter limits, one needs to use radio catalogues with a significantly higher number of sources. According to their estimation one needs about 2×10^5 sources, in order to constrain the kinetic radio dipole.

In Baleisis et al. (1998) spherical harmonics were used in order to predict and determine the dipole in a combined radio catalogue. The two catalogues used in their work were the Green Bank (Condon et al. 1989) and the Parkes-Mit-NRAO (Condon et al. 1993) catalogues. Combined those two catalogues contain about $40,000$ sources measured at 4.85 GHz. They found that for this survey the main dipole contribution should come from shot noise, due to the limited number of sources. The kinetic dipole would be below the shot noise and the contribution from large-scale structure would be even smaller than this. On the other hand they found, that the detected dipole ($d = 2.5 \times 10^{-2}$) is bigger (about 10%) than the direct combination of those three effects added up. This is surprising, since there is no reason that the shot noise must have an effect in the same direction as the kinetic and large-scale structure dipoles. To some extent, this high dipole amplitude may be explained by the fact that they use the combination of two catalogues instead of one. A small mismatch between the two catalogues will result in a significant dipole contribution.

The first reported detection of the dipole signal in radio surveys was made by Blake & Wall (2002). They used the NVSS catalogue (see section 1.6) in their analysis. In order to determine the dipole, they calculated the spherical harmonic coefficients up to $l = 3$ of the NVSS and fitted a dipole model to the resulting $a_{l,m}$. They masked the sky near (15°) the galactic plane and also removed areas within 30 arcsec of the most bright radio sources [specified by the IRAS PSCz catalogue (Saunders et al. 2000)]. In this way they tried to avoid too much contribution from local structures.

Their results are given in a slightly different notation [their δ corresponds

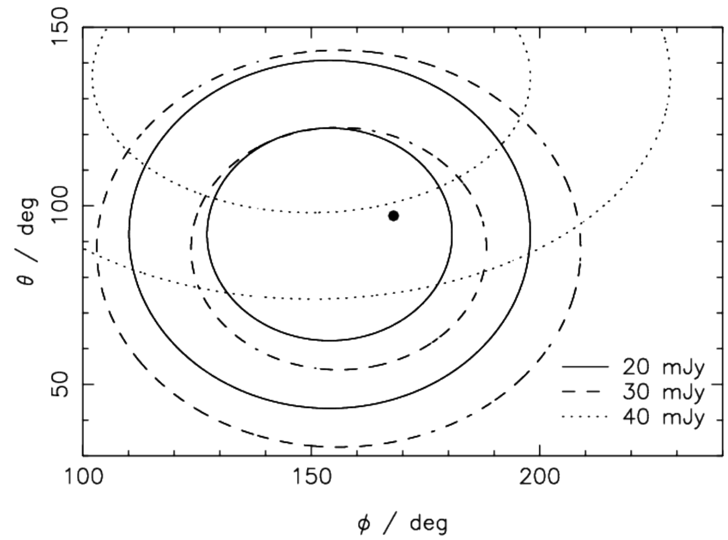

Figure 1.9: Radio dipole 1 and 2σ contours for the direction uncertainties for different lower flux limits. The black dot represents the position of the CMB dipole [source: Blake & Wall (2002)].

to two times our amplitude d in equation 1.6], which is converted here. One result they found is that the dipole in the NVSS depends on the applied lower flux limit. When this limits goes below 20 mJy the direction of the found signal moves towards the South Pole and the overall fit gets worse (meaning a significant increase in χ^2). Most likely this effect has to do with the different telescope configurations used, which resulted in changing sensitivities for different areas on the sky. Hence, at the low flux end of the survey the number of detected sources per area changed (see figure 1.7). The measured dipole directions for higher flux limits can be seen in figure 1.9. From this we can conclude that the direction of the dipole in the NVSS is in agreement with the direction obtained from the CMB within the (quite large) one-sigma contours.

The dipole amplitude estimation of Blake & Wall (2002) is somewhat more surprising. For the best fits they found a dipole of $d = (1.1 \pm 0.3) \times 10^{-2}$ at 25 mJy and $d = (1.1 \pm 0.4) \times 10^{-2}$ at 30 mJy. This is more than twice as big as expected from the CMB but still within the two-sigma environment. It is somewhat surprising that the dipole direction seems to be in much better agreement than the amplitude. This is the first hint towards increased dipole amplitude in radio surveys.

We can estimate the magnitude of such an effect in the following way. First we assume the velocity relative to the CMB is given by (Planck Collaboration et al. 2015b): $\tilde{v}_{\mathrm{cmb}} \approx 370$ km/s. The velocity relative to objects at a redshift of order unity are given by the one-sigma lower boundary of the dipole found in radio surveys [i.e. Blake & Wall (2002)]: $\tilde{v}_{\mathrm{NVSS}} \approx 640$ km/s. The difference between those two velocities could bias the later mentioned measurements by roughly

$$\tilde{v}_{\mathrm{bias}} = \tilde{v}_{\mathrm{NVSS}} - \tilde{v}_{\mathrm{CMB}} \approx 270 \frac{\mathrm{km}}{\mathrm{s}} \ . \tag{1.7}$$

This result is close to the reported bulk flow velocities discussed in 1.3. Hence, one could imagine that the found bulk flows may be a relic of a faulty rest-frame transformation.

The following studies are all based on a linear estimator first proposed by Crawford (2009). With this estimator each radio source is considered as a vector $\vec{r}$ pointing towards the sky at the corresponding position. Those vectors can have unity length $\hat{r}$ or they can be weighted by some factor, for example by their flux S. For a completely isotropic source distribution over the full sky the sum of all position vectors

$$\vec{D} = \sum \vec{r}_i \tag{1.8}$$

vanishes. When the main anisotropy on the sky comes from a dipole, this sum will not vanish, but one obtains a vector pointing towards the direction of the dipole signal. This kind of estimators will be discussed in section 2 in detail.

In Singal (2011) such a linear estimator was used on the NVSS and each source was weighted with the corresponding flux value. So the anisotropy in the radio flux distribution over the sky was analysed. Just like in Blake & Wall (2002), a dipole was found that has about the same direction as the CMB dipole but indicates an increased amplitude. Here the amplitude was even higher than in previous works and showed some significant discrepancy compared to the CMB expectation. Another study of the NVSS catalogue was performed by Gibelyou & Huterer (2012). They used a linear estimator without weights and also tried to correct for masking effects by means of randomly generated data points. This simulated masking dipole is supposed to compensate masking effects. Again a dipole amplitude was found that was significantly above the expectation. In this study, also the direction of the radio dipole was not in agreement with the one from the CMB. Both studies are discussed in detail in section Rubart & Schwarz (2013).

Another linear estimator was used by Kothari et al. (2013). They determined the spherical harmonic coefficients a_{lm} of the NVSS catalogue for $l = 1$. In contrast to Blake & Wall (2002), they did not fit a modelled distribution to the a_{lm}, but used those terms directly to obtain a dipole estimation. Hence, their estimator is also linear. In Kothari et al. (2013), the dipole in number counts as well as in sky brightness [corresponding to the flux-weighted estimator in Singal (2011)] was investigated. For a lower flux limit of $S = 20$ mJy the dipole amplitude of the first one was $d_N = (1.5 \pm 0.2) \times 10^{-2}$ and for the second one they obtained $d_S = (1.7 \pm 0.3) \times 10^{-2}$. The direction of the found dipoles is, like in previous works, in agreement with the CMB dipole.

The dipole estimation using the sky brightness does depend on the assumption that the number count $n(S)$ is a power law for the whole range of used sources and not only for sources close to the lower flux limit. For the observed number counts of the NVSS the power law assumption is a poor approximation and hence Kothari et al. (2013) tried an improved fit. They model the number counts as

$$n(S) \propto x S^{-1-x-\beta \ln S} , \tag{1.9}$$

with x and β being the free fit parameters. With this new fit, one can again determine the corresponding dipole amplitudes and from those calculate the observer's velocity, assuming the dipole is purely kinetic. The corresponding velocities obtained by estimations in sky brightness were reduced by about 10%, while velocities in source counts did not change. With this improved fit both estimators resulted in velocities of about 1300 ± 200 km/s for a flux limit of 20 mJy. In order to compare this with the abovementioned results, we transformed the velocities back into a dipole amplitude of $d_v = (1.6 \pm 0.3) \times 10^{-2}$, using equation 1.6.

In Tiwari & Jain (2015) the NVSS catalogue was utilized for the dipole estimation. In contrast to previous works, this time also cuts in polarization P and in the degree of polarization p were applied. The idea is that the degree of polarization depends on the frequency and hence those additional cuts will increase the dipole signal. The expected amplitude in this case is

$$d_P = [2 + x(1 + \alpha) + x_P(1 + \alpha_P)] \left(\frac{v}{c}\right) , \tag{1.10}$$

where x_P is the number-count slope with respect to the polarization and α_P is defined by an assumed dependence of polarization P on the frequency ν of $P \propto \nu^{-\alpha_P}$. Therefore a direct comparison of the dipole amplitudes is impractical, but the obtained velocities can be compared. Tiwari & Jain (2015) estimated the dipole in (a) source number and (b) polarization. The latter case is similar to the flux-weighted estimators mentioned above, with polarisation P replacing flux S.

In all those cases Tiwari & Jain (2015) found a significantly larger dipole amplitude than expected from the CMB observation. The anisotropy in polarization seems to be even larger than in source counts. For a flux limit of $S = 20$ mJy they found a peculiar velocity of the observer relative to the NVSS sources of 2550 ± 420 km/s. This is roughly two times the obtained value for the source count anisotropy and almost seven times the CMB expectation, but again the direction is in agreement with the CMB dipole. Since the values of x_P and α_P are not measured in this study (but assumed to be the same as for the number counts, i.e. $x_p = x$ & $\alpha_p = \alpha$), the mentioned velocity result should not be taken too serious yet.

From those previous works we can conclude that the radio dipole question is an active topic in radio astronomy. Due to the limited number of sources available in published radio catalogues, a precise measurement of this anisotropy has not yet been performed. Recent studies also suggest an increased dipole amplitude in radio surveys. In case those results turn out to be robust, interesting new effects could be discovered and examined. Connections to different related astrophysical questions, like for example the bulk flows, could arise. In any case a detailed investigation seems appropriate.

Chapter 2

The linear Radio Dipole

The trick is the idealizations.
— Richard Feynman

2.1 Publication A&A 555, A117 (2013)

The following publication was written by the first author and edited by the second. It contains a detailed analysis of various linear estimators. First the theoretical derivation of the kinetic dipole is presented, with an emphasis on the effect of the slope of corresponding number counts. For different surveys this slope is determined in order to make precise predictions of the expected dipole amplitude.

Previous results concerning the cosmic radio dipole are discussed and compared, including the differences in the estimators. A theoretical background for the expected shot noise contribution is developed and the results are tested and confirmed by simulations. Thereby a biasing factor in amplitude estimation due to shot noise contribution is revealed.

For the case of surveys with half-sky coverage, a two-dimensional linear estimator is presented and its properties (in comparison to the three-dimensional one) are investigated. This version of the linear estimator will become relevant in the light of upcoming radio telescopes.

In this publication the two radio catalogues, NVSS and WENSS, are analysed and the radio dipoles are estimated. The significance of the found amplitude excess is studied and compared with simulations. In this way the authors were able to show that, in spite of the shot noise bias, the resulting amplitudes are still significantly above the expected values.

A&A 555, A117 (2013)
DOI: 10.1051/0004-6361/201321215
© ESO 2013

Astronomy & Astrophysics

Cosmic radio dipole from NVSS and WENSS

M. Rubart and D. J. Schwarz

Fakultät für Physik, Universität Bielefeld, Postfach 100131, 33501 Bielefeld, Germany
e-mail: `[matthiasr;dschwarz]@physik.uni-bielefeld.de`

Received 1 February 2013 / Accepted 30 May 2013

ABSTRACT

We use linear estimators to determine the magnitude and direction of the cosmic radio dipole from the NRAO VLA Sky Survey (NVSS) and the Westerbork Northern Sky Survey (WENSS). We show that special attention has to be given to the issues of bias due to shot noise, incomplete sky coverage and masking of the Milky Way. We compare several different estimators and show that conflicting claims in the literature can be attributed to the use of different estimators. We find that the NVSS and WENSS estimates of the cosmic radio dipole are consistent with each other and with the direction of the cosmic microwave background (CMB) dipole. We find from the NVSS a dipole amplitude of $(1.8 \pm 0.6) \times 10^{-2}$ in direction $(\mathrm{RA}, \mathrm{dec}) = (154° \pm 19°, -2° \pm 19°)$. This amplitude exceeds the one expected from the CMB by a factor of about 4 and is inconsistent with the assumption of a pure kinetic origin of the radio dipole at 99.6% CL.

Key words. radio continuum: galaxies – large-scale structure of Universe

1. Introduction

The assumed isotropy and homogeneity of the Universe at large scales is fundamental to modern cosmology. The isotropy is best seen in the cosmic microwave background (CMB) radiation and holds at the per cent level. The most prominent anisotropy of the CMB temperature is a dipole signal of $\Delta T/T \approx 10^{-3}$. It is commonly assumed that this dipole is largely caused by the motion of the Solar system through the Universe (Stewart & Sciama 1967). This interpretation seems to be fully consistent with the concordance model of cosmology.

However, the observation of the microwave sky is not enough to tell the difference between a motion induced CMB dipole and dipole contributions form other physical phenomena, i.e.

$$\boldsymbol{d}_{\mathrm{cmb}} = \boldsymbol{d}_{\mathrm{motion}} + \boldsymbol{d}_{\mathrm{primordial}} + \boldsymbol{d}_{\mathrm{ISW}} + \boldsymbol{d}_{\mathrm{foregrounds}} + \boldsymbol{d}_{\mathrm{noise}}. \tag{1}$$

In our notation a dipole vector $\boldsymbol{d}$ modulates the isotropic sky by a factor $(1 + \boldsymbol{d} \cdot \hat{\boldsymbol{r}})$, with $\hat{\boldsymbol{r}}$ denoting the position on the sky.

Usually it is assumed that the primordial and the integrated Sachs-Wolfe (ISW) contribution to the CMB dipole are negligibly small and that foregrounds (the Milky Way) are under control. Within the concordance model we expect a primordial contribution of $d_{\mathrm{primordial}} \approx 2 \times 10^{-5}$. The ISW contribution could be as large as 10^{-4} from the gravitational potentials induced by local 100 Mpc sized structures, without being in conflict with the concordance model (Rakic et al. 2006; Francis & Peacock 2010). The noise term can be ignored due to excellent statistics of full sky observations. Thus the measured $\boldsymbol{d}_{\mathrm{cmb}}$ is directly used to infer the velocity of the Solar system w.r.t. the CMB to be $v = 369 \pm 0.9$ km s^{-1} (Hinshaw et al. 2009). It is used in many cosmological studies done in the CMB rest frame, e.g. supernova Hubble diagrams or measurements of large scale bulk flows.

The effects of motion are not limited to the CMB, but should actually be detectable at any frequency. In order to test the hypothesis $\boldsymbol{d}_{\mathrm{cmb}} = \boldsymbol{d}_{\mathrm{motion}}$, it would be very interesting to measure the dipole of another cosmic probe, such as that obtained by radio point source catalogues. In this case one expects to find

$$\boldsymbol{d}_{\mathrm{radio}} = \boldsymbol{d}_{\mathrm{motion}} + \boldsymbol{d}_{\mathrm{structure}} + \boldsymbol{d}_{\mathrm{foregrounds}} + \boldsymbol{d}_{\mathrm{noise}}. \tag{2}$$

Besides the signal from our proper motion, we expect a signal from structure in the Universe and we expect a random dipole from Poisson noise. The dipole from structure is expected to dominate any catalogue limited to redshift $z \ll 1$. Thus we are interested in surveys with a mean redshift of order unity and a large enough sky coverage to be sensitive to the dipole. This makes radio catalogues the preferred probe to look at. Within the concordance model, the dipole signal induced by the large scale structure is then a subdominant contribution, as it is for the CMB. If we had a large enough catalogue, we could compare $\boldsymbol{d}_{\mathrm{radio}}$ to $\boldsymbol{d}_{\mathrm{cmb}}$. Any statistically significant deviation would be exciting, while finding a match would put the concordance model on firmer grounds.

A first attempt to measure the radio dipole was performed by Baleisis et al. (1998) using a combination of the Green Bank 1987 and the Parkes-MIT-NRAO catalogues. Blake & Wall (2002), Singal (2011) and Gibelyou & Huterer (2012) attempted to determine the dipole vector in the NRAO VLA Sky Survey (NVSS), with different conclusions. Blake & Wall (2002) found a result that is in agreement with a purely kinetic origin of the cosmic radio dipole, but this was challenged by Singal (2011), who finds a dipole amplitude four times larger than expected, but strangely enough pointing in a direction consistent with the CMB dipole. The analysis of Gibelyou & Huterer (2012) finds both a different direction and an amplitude six times as large as the expected one. While Blake & Wall (2002) used a quadratic estimator, Singal (2011) and Gibelyou & Huterer (2012) used different linear estimators to find the dipole direction.

The purpose of this work is to discuss the use of linear estimators of the cosmic radio dipole and apply several versions of them on the NVSS (Condon et al. 2002) and the Westerbork

Northern Sky Survey (WENSS; Rengelink et al. 1997). We resolve the conflicts in the literature and extend the analysis to other linear estimators.

The NVSS survey covers about 10.3 sr of the sky and contains about 2×10^5 sources per steradian. For this survey the Very Large Array (VLA) in New Mexico (USA) has been used measuring at a frequency of 1.4 GHz. The survey includes over 80 per cent of the sky, missing only areas with declination $\delta < -40°$. The lower flux limit lies at 2.5 mJy for the 5σ detection of point sources. The NVSS was conducted by means of two different configurations of the VLA above and below $\delta = -10°$.

The Westerbork Synthesis Radio Telescope in the Netherlands was operated at a frequency of 325 MHz to record the WENSS survey covering about 2.9 sr of the nothern sky and containing about 2.3×10^5 sources in total. This survey is made up of a main catalogue for $\delta \in (28°, 76°)$ and a polar catalogue for $\delta > 72°$. The 5σ detection limit for this survey is 18 mJy.

To analyse these surveys, we focus on linear estimators in this work. We do so for two reasons. Firstly, recent controversial results used linear estimators for the dipole direction (Singal 2011; Gibelyou & Huterer 2012) and in one work also for the dipole amplitudes (Singal 2011). Secondly, linear estimators are conceptually simpler. However, it is not expected that they are optimal (unbiased and minimal variance). The linear estimators used in our analysis are asymptotically unbiased and their variance can be easily understood by analytic calculations and by Monte Carlo simulations.

The paper is organized as follows: first we discuss the expected kinetic radio dipole. In Sect. 3 we outline previous estimates of the radio dipole. Linear estimators for full sky surveys are investigated in Sect. 4, followed by a detailed analysis of the effects of incomplete sky coverage and masking in the next section. In Sect. 6 we discuss the expected dipole amplitude from a flux based estimator. Our estimate of the radio dipole can be found in Sect. 7 and is followed by a comparison with previous results. We conclude in Sect. 9.

2. Kinetic radio dipole

2.1. Doppler shift and aberration

Ellis & Baldwin (1984) predicted the kinetic contribution to the cosmic radio dipole for an isotropic and homogeneous cosmology. At redshift of order unity and beyond, we expect this kinetic contribution to be the dominant one.

The spectrum of a radio source is assumed to be described by a power law,

$$S(f) \propto f^{-\alpha}, \tag{3}$$

where S denotes the flux and f the frequency. Each radio source can be described by an individual spectral index α. For simplicity we assumed a mean value of α for all radio sources in the catalogue.

The number of observed radio sources per steradian depends on the lower flux limit and can be approximated by a power law

$$\frac{\mathrm{d}N}{\mathrm{d}\Omega}(>S) \propto S^{-x}. \tag{4}$$

The value of x can be different for each survey. Typically x is assumed to be about one.

Two effects have to be taken into account. The emitted radio frequency f_{rest} is observed at the Doppler shifted frequency f_{obs}. The magnitude of this change depends on the angle θ between the direction to the source and the direction of our motion, with velocity v. Observed and rest frame frequencies are related by

$$f_{\mathrm{obs}} = f_{\mathrm{rest}}\delta(v, \theta), \tag{5}$$

where δ is given by

$$\delta(v, \theta) = \frac{1 + \frac{v}{c}\cos(\theta)}{\sqrt{1 - (\frac{v}{c})^2}}\cdot \tag{6}$$

Thus the observed flux changes due to our motion, since it depends on the frequency

$$S_{\mathrm{obs}}(f_{\mathrm{obs}}) \propto \delta f_{\mathrm{rest}}^{-\alpha} \propto \delta^{1+\alpha} f_{\mathrm{obs}}^{-\alpha} \propto S_{\mathrm{rest}}(f_{\mathrm{obs}})\delta^{1+\alpha}. \tag{7}$$

The first factor of δ is due to the fact that the energy of an observed photon is enhanced due to the Doppler effect.

Thus, the Doppler effect will change the number of observed sources above a given flux limit like

$$\left(\frac{\mathrm{d}N}{\mathrm{d}\Omega}\right)_{\mathrm{obs}} = \left(\frac{\mathrm{d}N}{\mathrm{d}\Omega}\right)_{\mathrm{rest}} \delta^{x(1+\alpha)}. \tag{8}$$

Since the velocity of light is finite, aberration will also modify the number counts. The position of each source is changed towards the direction of motion. The new angle θ' (observed from Earth) between the position of the source and the direction of motion is given by

$$\tan\theta' = \frac{\sin\theta\sqrt{1 - \frac{v^2}{c^2}}}{\frac{v}{c} + \cos\theta}\cdot \tag{9}$$

Therefore, at first order in v/c, $d\Omega$ transforms like

$$\mathrm{d}\Omega' = \mathrm{d}\Omega\left(1 - 2\frac{v}{c}\cos\theta\right) + O\left(\left(\frac{v}{c}\right)^2\right)\cdot \tag{10}$$

This can be combined with the Doppler effect to give the observed number density. After approximating $\delta(v, \theta)$ to first order in $\frac{v}{c}$, the result becomes

$$\frac{\mathrm{d}N}{\mathrm{d}\Omega}_{\mathrm{obs}} = \left(\frac{\mathrm{d}N}{\mathrm{d}\Omega}\right)_{\mathrm{rest}} \left[1 + [2 + x(1+\alpha)]\left(\frac{v}{c}\right)\cos(\theta)\right]. \tag{11}$$

The amplitude of the kinetic radio dipole is then given by

$$d = [2 + x(1+\alpha)]\left(\frac{v}{c}\right)\cdot \tag{12}$$

The kinetic radio dipole points towards the direction of our peculiar motion, which in an isotropic and homogeneous Universe must also agree with the direction defined by the CMB dipole.

2.2. Expected kinetic radio dipole

The measured CMB dipole is $\Delta T = 3.355 \pm 0.008$ mK in the direction $(l, b) = (263.99° \pm 0.14°, 48.26° \pm 0.03°)$ (Hinshaw et al. 2009). In equatorial coordinates (epoch J2000) its direction reads (RA, Dec) = $(168°, -7°)$. Compared to the CMB temperature of $T_0 = 2.725 \pm 0.001$ K (Fixsen & Mather 2002). this corresponds to a relative fluctuation of $\Delta T/T = (1.231 \pm 0.003) \times 10^{-3}$ and thus the velocity of the Solar system has been inferred from the CMB dipole to be $v = 369.0 \pm 0.9$ km s^{-1} (Hinshaw et al. 2009).

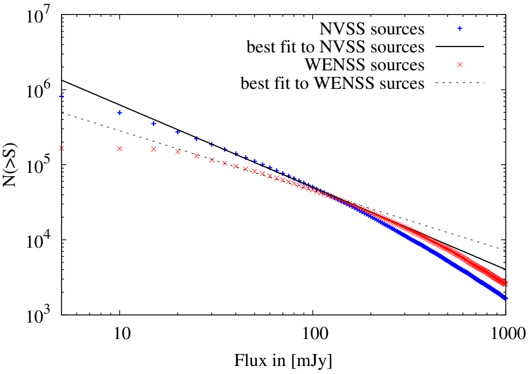

Fig. 1. Number counts of the NVSS and WENSS surveys. A function $f(S) \propto S^{-x}$ is fitted to both data sets in the range of 25 mJy $< S <$ 200 mJy. Resulting values of x are 1.10 ± 0.02 for the NVSS survey and 0.80 ± 0.02 for the WENSS survey.

Table 1. Best-fit dipole parameters from Blake & Wall (2002).

Flux (mJy)	N	RA (°)	Dec (°)	d (10^{-2})	$\chi^2_{\rm red}$
>40	125 603	149 ± 49	–45 ± 38	0.7 ± 0.5	1.02
>35	143 524	161 ± 44	–27 ± 39	0.9 ± 0.4	0.74
>30	166 694	156 ± 32	2 ± 33	1.1 ± 0.4	1.01
>25	197 998	158 ± 30	–4 ± 34	1.1 ± 0.3	1.01
>20	242 710	153 ± 27	–3 ± 29	1.1 ± 0.3	1.32
>15	311 037	148 ± 29	31 ± 31	0.8 ± 0.3	1.81
>10	431 990	132 ± 29	65 ± 19	0.5 ± 0.2	4.96

Notes. Coordinate system and amplitude definition are adjusted for comparison with Singal's results (see Tables 2 and 3). N denotes the number of point sources with flux above the indicated limit.

Table 2. Dipole direction and amplitude from the number count estimator (15) from Singal (2011).

Flux (mJy)	N	RA (°)	Dec (°)	d (10^{-2})
≥50	91 597	171 ± 14	−18 ± 14	2.1 ± 0.5
≥40	115 837	158 ± 12	−19 ± 12	1.8 ± 0.4
≥35	132 930	157 ± 11	−12 ± 11	1.9 ± 0.4
≥30	154 996	156 ± 11	−02 ± 10	2.0 ± 0.4
≥25	185 474	158 ± 10	−02 ± 10	1.8 ± 0.4
≥20	229 365	153 ± 10	+02 ± 10	1.8 ± 0.3
≥15	298 048	149 ± 09	+15 ± 09	1.6 ± 0.3

To find the expected amplitude of the kinetic radio dipole, we also need estimates for x and α. The typically assumed values are $x = 1$ and $\alpha = 0.75$, which gives together with $v = 370$ km s^{-1} a radio dipole amplitude of $d = 0.46 \times 10^{-2}$. However, we can improve on that as x can be measured with help of the radio survey. Therefore we need to plot $N(>S)$ against S like in Fig. 1.

For the purpose of this work we find $x_{\rm NVSS} = 1.10 \pm 0.02$ and $x_{\rm WENSS} = 0.80 \pm 0.02$. The mean spectral index cannot be inferred from the catalogues, as they provide data at a single frequency band only. We thus stick to $\alpha = 0.75$, but include in the dipole error an uncertainty of $\Delta\alpha = 0.25$ (Garn et al. 2008). This results in the expectations:

$$d^{\rm exp}_{\rm NVSS} = (0.48 \pm 0.04) \times 10^{-2}, \tag{13}$$

$$d^{\rm exp}_{\rm WENSS} = (0.42 \pm 0.03) \times 10^{-2}. \tag{14}$$

The error is dominated by the uncertainty in the spectral index.

3. Previous results

The first measurement of the radio dipole using the NVSS catalogue was performed by Blake & Wall (2002). In order to remove corruption by local structure, all sources within 15° vicinity of the Galactic disk have been removed. Additionally the clustering dipole contribution was reduced by ignoring sources within 30″ of nearby known galaxies. The spherical harmonic coefficients $a^{\rm obs}_{lm}$ from the remaining NVSS catalogue have been determined up to $l = 3$. A model for a dipole distribution with an isotropic background has been constructed (a_{00} and a_{10}). Due to masking, this dipole distribution also influences higher multipoles. After applying the same mask as for the NVSS catalogue, one finds $a^{\rm model}_{lm}$ up to $l = 3$. A quadratic estimator (chi square) was used to compare the model with the observed coefficients.

The resulting best-fit dipoles can be seen in Table 1. The results of Blake & Wall (2002) indicate a higher radio dipole than expected, however without statistical significance.

Singal (2011) used a linear estimator, originally proposed by Crawford (2009),

$$\boldsymbol{R}_{\rm 3D} = \sum \hat{\boldsymbol{r}}_i, \tag{15}$$

and a variation of it, which we discuss below. For a large number of sources the isotropic background will clear away. The remaining vector $\boldsymbol{R}_{\rm 3D}$ will point towards the main anisotropy in the distribution of number density over the sky. To get the correct dipole amplitude d one has to normalize this estimator depending on the number of sources. In Singal's analysis sources within 10° of the Galactic plane have been removed. In order to avoid directional bias (see the more detailed discussion below), he reestablished a north-south symmetry of the NVSS by cutting all sources with dec > 40°. The results of Singal (2011) are shown in Table 2. The errors of the directional measurements are quite small here. This is an effect of an unexpectedly large amplitude, which simplifies the measurement. While the direction agrees with the one found by Blake & Wall (2002), the dipole amplitude seems to be a factor of about four higher than expected from the CMB dipole and twice as big as found by Blake & Wall (2002).

Masking the supergalactic plane in order to reduce the contribution of local structure did not resolve the discrepancy. Since unknown clustering further away from the super Galactic plane could also have contributed to the measurement, a second test was performed. A clustering contribution to the dipole would not give a signal proportional to $\cos\theta$. On the other hand, the difference in number counts of areas that are opposite to each other should decrease with $\cos\theta$ (where θ is the angle between an area and the measured dipole direction), if the measured dipole is due to our velocity. Singal was able to fit such a behaviour to the data. Therefore he concludes that the radio dipole amplitude is not due to local clustering.

Singal (2011) also used a linear estimator for the distribution of flux over the sky. This estimator is similar to the number density estimator (15), but weights each radio source by its flux S_i,

$$\boldsymbol{R}_{\rm flux} = \sum S_i \hat{\boldsymbol{r}}_i. \tag{16}$$

Table 3. Dipole direction and amplitude from the flux weighted number count estimator (16) from Singal (2011).

Flux (mJy)	N	RA (°)	Dec (°)	d (10^{-2})
$1000 > S \geq 50$	90 360	163 ± 12	-11 ± 11	2.3 ± 0.7
$1000 > S \geq 40$	114 600	159 ± 12	-11 ± 11	2.2 ± 0.6
$1000 > S \geq 35$	131 691	159 ± 11	-10 ± 10	2.2 ± 0.6
$1000 > S \geq 30$	153 759	159 ± 11	-07 ± 10	2.2 ± 0.6
$1000 > S \geq 25$	184 237	159 ± 10	-07 ± 09	2.2 ± 0.6
$1000 > S \geq 20$	228 128	158 ± 10	-06 ± 09	2.1 ± 0.5
$1000 > S \geq 15$	296 811	157 ± 09	-03 ± 08	2.0 ± 0.5

Like $\boldsymbol{R}_{3\mathrm{D}}$, this estimator finds the main anisotropy and the amplitude needs to be normalized. The brightest sources ($S > 1000$ mJy) are removed, because they would dominate $\boldsymbol{R}_{\mathrm{flux}}$ otherwise. Results of this estimator are shown in Table 3. The estimated directions are in agreement with the results of Blake & Wall (2002) and the number count estimator results of Singal (2011). However, the normalized dipole amplitudes d are even higher than those of the number count estimator $\boldsymbol{R}_{3\mathrm{D}}$. In Sect. 6 we resolve this conflict.

Most recently, Gibelyou & Huterer (2012) measured a dipole amplitude ($d = 2.7 \pm 0.5) \times 10^{-2}$ towards (RA, Dec) = ($117 \pm 20°, 6 \pm 14°$) from the NVSS. This direction is inconsistent with the studies mentioned above and the dipole amplitude is a factor of five larger than expected. The authors used separate estimators for the direction and the amplitude. Their direction estimate is based on a linear estimator, originally proposed by Hirata (2009),

$$\boldsymbol{R}_{3\mathrm{DM}} = \sum_{i}^{N_{\mathrm{D}}} \hat{r}_i - \frac{N_{\mathrm{D}}}{N_{\mathrm{R}}} \sum_{j}^{N_{\mathrm{R}}} \hat{r}_j. \tag{17}$$

This three-dimensional estimator (3DM) is intended to be unbiased for arbitrary survey geometries and arbitrary masking. The idea is to achieve that with help of the second sum, which goes over N_{R} randomly distributed points, subject to the same masking. Therefore, the authors include all sources of the NVSS survey, except for those within 10° of the Galactic plane. Below we show that this estimator has a direction bias, which depends on the real dipole anisotropy.

We summarize, there is no agreement on the amplitude and direction of the cosmic radio dipole so far.

4. Linear estimators for a full sky

Let us first show that the estimator (15) provides an unbiased estimate of the dipole direction.

Starting from the distribution of the number of radio sources per solid angle (11), as seen by a moving observer in an otherwise isotropic Universe, the probability to find a given radio source within a solid angle dΩ of position $\hat{\boldsymbol{r}}$ is given by

$$p(\hat{\boldsymbol{r}})\mathrm{d}\Omega = \frac{1}{4\pi}(1 + \hat{\boldsymbol{r}} \cdot \boldsymbol{d})\mathrm{d}\Omega, \tag{18}$$

where $\boldsymbol{d}$ denotes the dipole vector.

To study the bias of an estimator, we calculate its expectation value with respect to an ensemble average. We do so below by means of Monte Carlo studies. For analytic considerations, for large N we replace the ensemble average by a spatial average, i.e.

$$\langle 1 \rangle = \int \prod_{i=1}^{N} \mathrm{d}\Omega_i p(\hat{\boldsymbol{r}}_i) 1 = 1, \tag{19}$$

thus we assume ergodicity. Note that the average is a linear operator.

Now the expectation value of Crawford's estimator can be evaluated for large N,

$$\langle \boldsymbol{R}_{3\mathrm{D}} \rangle = \langle \sum_{i=1}^{N} \hat{r}_i \rangle = \sum_{i=1}^{N} \langle \hat{r}_i \rangle = \frac{N}{4\pi} \int \mathrm{d}\Omega \,(1 + \hat{r} \cdot \boldsymbol{d})\, \hat{r}. \tag{20}$$

This calculation holds for independent, identically distributed positions $\hat{r}_i$, thus without clustering effects. Only the second term survives the integration and thus the expected dipole estimator is

$$\langle \boldsymbol{R}_{3\mathrm{D}} \rangle = \frac{1}{3} N \boldsymbol{d}. \tag{21}$$

Naively, one could now estimate the dipole signal by $\boldsymbol{d}_{3\mathrm{D}} \equiv \frac{3}{N} \boldsymbol{R}_{3\mathrm{D}}$.

We conclude that $\boldsymbol{d}_{3\mathrm{D}}$ provides us with an unbiased estimate of the dipole direction $\hat{\boldsymbol{d}}$ for a full sky sample. However the estimated dipole amplitude $|\boldsymbol{d}_{3\mathrm{D}}|$ is biased.

To understand the origin of this bias let us first consider

$$\langle \boldsymbol{d}_{3\mathrm{D}}^2 \rangle = \left(1 - \frac{1}{N}\right) d^2 + \frac{9}{N} > d^2. \tag{22}$$

The inequality holds for large N and $d < 3$ (in case of large dipole amplitudes [$d = O(1)$] our ansatz (19) should also take many-point correlations into account). Thus $\boldsymbol{d}_{3\mathrm{D}}^2$ is definitely biased towards higher amplitudes. However, to prove that $|\boldsymbol{d}_{3\mathrm{D}}|$ is biased, we would need to calculate $\langle |\boldsymbol{d}_{3\mathrm{D}}| \rangle$. We do this by means of the random walk/flight method.

4.1. Random flight

Adding up vectors for each point of a survey corresponds to a random walk with unit step size. To be more precise this is a random flight, since the problem is three dimensional. Even for a vanishing dipole, such a random flight is unlikely to return to the origin after N steps. This describes the noise of any realisation of an isotropic distribution of N sources.

Following Crawford (2009), we determine the distance r from the origin after N steps from the probability density of a random flight process

$$\check{P}_N(r)\mathrm{d}r = \left[\frac{54}{\pi N^3}\right]^{1/2} r^2 \exp\left(-\frac{3r^2}{2N}\right)\mathrm{d}r. \tag{23}$$

The probability of measuring a dipole signal of an amplitude bigger than R in a random flight is

$$P_N(R > R_{pCL}) = \int_{R_{pCL}}^{\infty} \mathrm{d}r \check{P}_N(r) = 1 - pCL. \tag{24}$$

A confidence level pCL can be choosen, leading to errorbars for a measured dipole vector $R_{3\mathrm{D}} \pm R_{pCL}$. To estimate the directional uncertainties of this method, Crawford (2009) made the following argument: at a given confidence level the random flight corresponds to a step of length up to R_{pCL}. Adding R_{pCL}

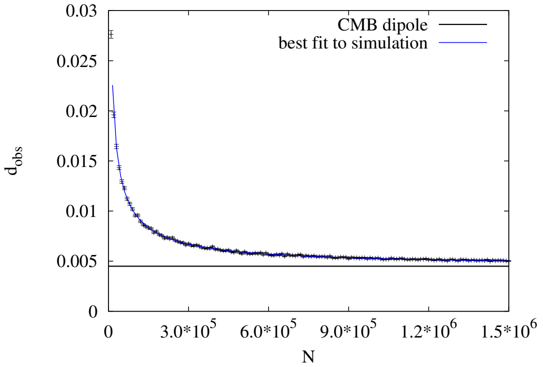

Fig. 2. Ampliude bias of the full sky estimator d_{3D}. Data represent mean and empirical variance of 1000 simulations for each N. A function $d_{obs}(N) = \sqrt{D^2 + 9A^2/N}$ is fitted to the simulated data, with best-fit values $A = 0.908 \pm 0.002, D = (0.451 \pm 0.001) \times 10^{-2}$. The expected dipole amplitude ($d = 0.0046$) is indicated by the horizontal line.

perpendicular to the measured dipole $\boldsymbol{R}_{3D}$ allows us to estimate the maximal offset in direction. Using trigonometry, one can relate R_{pCL} to the directional uncertainties expressed as the angle

$$\delta\theta_{pCL} = \arcsin\frac{R_{pCL}}{R_{3D}}. \tag{25}$$

The expected magnitude of the random dipole contribution is estimated from (23) as

$$\langle R^{\text{random}}_{3D}\rangle = \int_0^\infty r\left[\frac{54}{\pi N^3}\right]^{1/2} r^2 \exp\left(-\frac{3r^2}{2N}\right)\mathrm{d}r \approx 0.92\sqrt{N}. \tag{26}$$

Since the random dipole has no distinguished direction, there is no direction bias of the linear estimator for a full sky map.

Even for vanishing d, this gives rise to a non-vanishing estimate of the dipole amplitude $d^{\text{random}}_{3D} = 2.8N^{-1/2}$ and is thus the origin of the amplitude bias.

Motivated by (22) we make the following ansatz for the dipole amplitude and its bias:

$$\langle d_{3D}\rangle = \sqrt{d^2 + \frac{9}{N^2}\langle R^{\text{random}}_{3D}\rangle^2}. \tag{27}$$

To verify this analytic estimate of the biased amplitude, we simulated full sky maps including a velocity dipole (with $v = 370$ km s^{-1}). From these simulated catalogues we extracted the observed amplitude d_{obs}. Figure 2 shows the simulated data, the true value of the dipole amplitude and a fit of the form $f(N) = \sqrt{D^2 + 9A^2/N}$.

The best-fit values are $A = 0.908 \pm 0.002$ and $D = (0.451 \pm 0.001) \times 10^{-2}$ (statistical errors only). These numbers should be compared to the factor 0.92 from (26) and the simulation input of $d = 0.46 \times 10^{-2}$. The reduced chi- square of the fit is 7×10^{-5}. Thus the Monte Carlo simulations agree with the theoretically motivated ansatz (27) for the expected dipole amplitude of the estimator $\boldsymbol{d}_{3D}$.

We conclude that even for a perfect full sky catalogue (no masking, complete in flux, perfect flux and position measurements), the amplitude of the linear estimator is biased towards higher values. Increasing the number of radio sources will reduce the bias. The estimator d_{3D} is asymptotically unbiased, but this is of limited practical use for the analysis of NVSS and WENSS data. A similar bias of the dipole amplitude is also found for the other linear estimators introduced above. This finding is in agreement with Gibelyou & Huterer (2012), who use a linear estimator to find the direction of the dipole.

5. Linear estimators for an incomplete sky

So far we assumed full coverage of the radio sky. More realistic catalogues cover just a fraction of the sky, as all earth based telescopes are limited to observe at certain declination ranges. Additionally, the Milky Way is masking parts of the sky. Here we discuss some of the effects caused by incomplete sky coverage.

The upcoming Low Frequency Array (LOFAR) Tier-1 survey will cover about half of the sky (2π), thus we first focus on this situation. As a second step we generalize this to an arbitrary axisymmetric survey geometry and include the effects of masking.

5.1. Random walk

Let us assume a survey geometry that covers all of the Northern hemisphere and ask how the estimator of the radio dipole (15) has to be modified. For the first two Cartesian components of $\boldsymbol{R}_{3D}$ there should be no systematic problem, but the third component will definitely be biased. It is necessary to remove the effect of the incomplete sky from this z component. Consider the expectation value of $\boldsymbol{R}_{3D}$ for the Northern hemisphere

$$\langle\boldsymbol{R}_{3D}\rangle_{\text{hemisphere}} = \langle\sum_{i=1}^{N}\hat{r}_i\rangle = \frac{Np_d}{2\pi}\int_{\delta>0}\mathrm{d}\Omega(1+\hat{r}\cdot\boldsymbol{d})\hat{r}, \tag{28}$$

where $p_d \equiv 1/[1 + (d/2)\cos\vartheta_d)]$ accounts for the proper normalisation of the probability distribution on the hemisphere in presence of a dipole. 4π in (18) becomes 2π for obvious reasons. The integral can be evaluated by hand. One finds

$$\langle\boldsymbol{R}_{3D}\rangle_{\text{hemisphere}} = Np_d\begin{pmatrix}\frac{1}{3}d\cos\varphi_d\sin\vartheta_d\\ \frac{1}{3}d\sin\varphi_d\sin\vartheta_d\\ \frac{1}{2}+\frac{1}{3}d\cos\vartheta_d\end{pmatrix}, \tag{29}$$

where ϑ_d and φ_d denote the dipole position in spherical coordinates. The z direction is strongly influenced by the incomplete sky coverage. The total number of observed sources is not independent from the amplitude and orientation of the dipole itself.

Nevertheless there is no problem in the evaluation of φ_d because one can calculate

$$\varphi_d = \arctan\frac{R_y}{R_x}. \tag{30}$$

Here N as well as $\sin\vartheta_d$ cancel out. So the 2D estimator is unbiased with respect to φ_d. Therefore we propose a pure two dimensional estimator:

$$\boldsymbol{R}_{2D} = \sum_i^N\begin{pmatrix}\cos\varphi_i\sin\vartheta_i\\ \sin\varphi_i\sin\vartheta_i\\ 0\end{pmatrix}. \tag{31}$$

From this one can still use $(R_x^2 + R_y^2)^{-1/2}$ for evaluating $d\sin\vartheta_d Np_d/3$ and φ_d. Let us take a look at the factor $\sin\vartheta_d$. Sources near the pole will make a smaller contribution than those further away. If a source near the pole is shifted by a small distance, the value φ_i of this source could change dramatically.

So the weighting terms compensate for this artificially big errors, which are just a relic of the coordinate system.

Let us now estimate the uncertainties of the estimator $\boldsymbol{R}_{2\mathrm{D}}$. The problem corresponds to an isotropic random walk process with variable step size. The probability density for a displacement of r for such a random walk is

$$\check{P}_N(r)_{2\mathrm{D}}\mathrm{d}r = \frac{3}{N} r \exp\left(-\frac{3r^2}{2N}\right)\mathrm{d}r. \quad (32)$$

Similar to the random flight we determine R_{pCL} defined by

$$P_N(R_{2\mathrm{D}} > R_{pCL}) = \int_{R_{pCL}}^{\infty} \mathrm{d}r \check{P}_N(r)_{2\mathrm{D}} = 1 - pCL. \quad (33)$$

Here again pCL is the confidence level. It is possible to solve the above integral analytically

$$\int_{R_{pCL}}^{\infty} \mathrm{d}r \frac{3}{N} r \exp\left(-\frac{3r^2}{2N}\right) = \exp\left(-\frac{3R_{pCL}^2}{2N}\right). \quad (34)$$

So R_{pCL} is given by

$$R_{pCL} = \sqrt{\frac{2N}{3}\ln\left(\frac{1}{1-pCL}\right)}. \quad (35)$$

Now one can use the same argument as for the random flight to evaluate the uncertainty of the φ_d estimation

$$\delta\varphi_{pCL} = \arcsin\frac{R_{pCL}}{R_{2\mathrm{D}}}. \quad (36)$$

In this way one can directly determine error bars for measured results of φ_d calculated via (30). Using this two dimensional estimator one cannot measure the dipole amplitude d itself but only the combination $d\sin\vartheta_\mathrm{d} N p_\mathrm{d}/3$. Therefore it can only give an lower limit for d.

Like in the case of the full three dimensional estimator, this version is also biased in the measurement of the amplitude. The expectation of the random contribution can be calculated via

$$\langle R_{2\mathrm{D}}^{\mathrm{random}}\rangle = \int_0^{\infty} r\frac{3}{N} r \exp\left(-\frac{3r^2}{2N}\right)\mathrm{d}r \approx 0.72\sqrt{N}. \quad (37)$$

So we expect our estimator to measure a combination of this random contribution and the true velocity dipole and make the ansatz

$$\langle d_{2\mathrm{D}}\rangle = \sqrt{d^2\sin^2\vartheta_\mathrm{d} + \frac{9}{N^2}\langle R_{2\mathrm{D}}^{\mathrm{random}}\rangle^2}, \quad (38)$$

where we used $p_\mathrm{d} \approx 1$. Like above, we verify this via Monte Carlo simulations, shown in Fig. 3.

5.2. Direction bias

For any masked or incomplete map of the sky, we cannot measure the mean source density $\bar{N}/(4\pi)$, i.e. the monopole. Therefore we always have to keep in mind that the observed mean density is just an approximation. Gibelyou & Huterer (2012) have used an estimator proposed by Hirata (2009), which implicitly assumes, that the monopole is known. Based on the knowledge of the monopole, this estimator would compensate for masking effects and incomplete sky coverage by substracting a pure random isotropic map from the observed dipole term via (17). However, we cannot know $\bar{N}$.

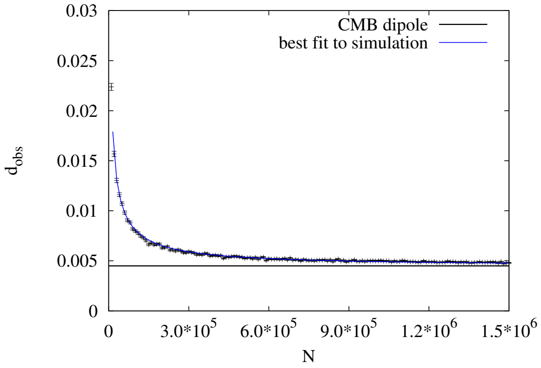

Fig. 3. Ampliude bias for the estimator $d_{2\mathrm{D}}$ on a hemisphere. Data represent mean and empirical variance of 1000 simulations for each N. A function $d_{\mathrm{obs}}(N) = \sqrt{D^2 + 9A^2/N}$ is fitted to the simulated data, with best fit values $A = 0.712 \pm 0.003$ and $D = (0.444 \pm 0.002) \times 10^{-2}$. The dipole amplitude (0.0046) is indicated by the horizontal line, the dipole vector is assumed to lie in the equatorial plane ($\sin\vartheta_\mathrm{d} = 1$).

For the previous example of a hemisphere, the monopole density is $\bar{N}/(4\pi) = Np_\mathrm{d}/(2\pi)$, where $N = N_\mathrm{D}$ in (17). The random map can be made up of an arbitrary number of sources N_R, but is reweighted by the observed number of sources $N_\mathrm{D}/N_\mathrm{R}$, instead of $\bar{N}/N_\mathrm{R}$. This introduces a directional bias, in addition to the previously discussed biased amplitude. One can see this explicitly by applying (17) on our model of a dipole modified isotropic hemisphere. We find

$$\langle\boldsymbol{R}_{3\mathrm{DM}}\rangle_{\mathrm{hemisphere}} = \frac{Np_\mathrm{d}}{3}d\begin{pmatrix}\cos\varphi_\mathrm{d}\sin\vartheta_\mathrm{d}\\ \sin\varphi_\mathrm{d}\sin\vartheta_\mathrm{d}\\ \cos\vartheta_\mathrm{d}\end{pmatrix} + \frac{1}{2}N\begin{pmatrix}0\\ 0\\ p_\mathrm{d}-1\end{pmatrix}, \quad (39)$$

which clearly is not parallel to $\boldsymbol{d}$. For small values of d we can expand p_d and obtain

$$\langle\boldsymbol{R}_{3\mathrm{DM}}\rangle_{\mathrm{hemisphere}} = \frac{N}{3}d\begin{pmatrix}\cos\varphi_\mathrm{d}\sin\vartheta_\mathrm{d}\\ \sin\varphi_\mathrm{d}\sin\vartheta_\mathrm{d}\\ \frac{1}{4}\cos\vartheta_\mathrm{d}\end{pmatrix} + O\left(d^2\right). \quad (40)$$

The z component of the dipole is underestimated by a factor of 4 for the geometry of a hemisphere. Despite cancelation of the leading term of the bias of the z direction, the dipole direction remains biased. Less symmetric survey geometries lead to a bias of all dipole components for this estimator.

The best strategy to avoid any directional bias for a linear estimator is to make the survey geometry point symmetric around the observer for three dimensional estimators like $\boldsymbol{R}_{3\mathrm{D}}$ or point symmetric around the zenith in case of two dimensional estimators $\boldsymbol{R}_{2\mathrm{D}}$. This implies for the NVSS that one has to cut symmetric in declination, such that both polar caps are missing, a strategy that was used by Singal (2011).

5.3. Masking

The use of a masked sky additionally affects the dipole measurement. In general, the estimated dipole direction and amplitude depend on the position of the true dipole relative to the mask. Cutting areas with large dipole contribution will reduce the amplitude and vice versa.

In the following we consider masks that are point symmetric with respect to the observer for all considered 3-dimensional estimators, respectively point symmetric with respect to the zenith for the 2-dimensional estimators. Constructed in such a way, masking does not introduce any directional bias. Nevertheless, we have to consider the effects of masking on the estimated dipole amplitude.

A simple method to correct for this effect was put forward by Singal (2011), who introduced a masking factor k,

$$\boldsymbol{R}_{3\mathrm{D}}^{\mathrm{mask}} = \frac{1}{k_{3\mathrm{D}}} \sum \boldsymbol{r}_i. \tag{41}$$

Such a factor is expected to be a function of shape and position of the mask as well as the dipole position. In most cases an analytic calculation of this factor is impossible. For simple mask geometries some analytic results can be found in Rubart (2012). An alternative approach is to simulate the effects by means of Monte Carlos and to compare simulations with and without masking. The ratio of both results after a large number of simulations provides the masking factor $k_{3\mathrm{D}}$.

Doing so, we found some interesting effects. The masking factors depend on the number of objects in the simulated maps as well as on the true dipole amplitude. This can be explained as follows. The masking will mainly affect the kinetic dipole contribution, while the random dipole will increase due to the decrease of the number of objects in the masked catalogue. Therefore we expect the amplitude to be

$$\langle d_{3\mathrm{D}} \rangle_{\mathrm{mask}} = \sqrt{k_{3\mathrm{D}}^2 d^2 + \frac{9}{N^2} \langle R_{3\mathrm{D}}^{\mathrm{random}} \rangle^2}. \tag{42}$$

$k_{3\mathrm{D}}$ should only depend on the properties of the mask and not on the amplitude of the dipole. To test this, we created simulated maps for two different dipole amplitudes, with values motivated by the CMB measurement $d_{\mathrm{CMB}} = 0.46 \times 10^{-2}$ and by the measurement of Blake & Wall (2002) at 25 mJy $d_{\mathrm{BW}} = 1.1 \times 10^{-2}$. We used the direction RA $= 158°$, Dec $= -4°$ in both cases. The mask agrees with the one used by Singal (2011), i.e. we removed all sources with $|\delta| > 40°$ and $|b| < 10°$. Resulting amplitudes for different numbers of sources are shown in Fig. 4.

First of all we can conclude that (42) is a good fit for the behaviour of the simulated maps in both cases. The measured amplitudes are larger than those estimated from full sky maps. We can now calculate $k_{3\mathrm{D}}$. In both cases it turns out to be 1.4, which could be used to correct the amplitude estimate.

A similar argument holds for the two dimensional estimator. Here we expect a behaviour of the form:

$$\langle d_{2\mathrm{D}} \rangle_{\mathrm{mask}} = \sqrt{k_{2\mathrm{D}}^2 d^2 \sin^2 \vartheta_{\mathrm{d}} + \frac{9}{N^2} \langle R_{2\mathrm{D}}^{\mathrm{random}} \rangle^2}. \tag{43}$$

Using the same assumptions about the dipole term and the same mask as before, we obtain Fig. 5.

This time, we find $k_{2\mathrm{D}} = 1.3$ for both assumed velocities. The simulations support our assumption that the masking factor does not depend on the dipole magnitude d.

5.3.1. Masking correction

Although the masking factor k does not depend on the amplitude d, it may depend on the dipole direction $\hat{\boldsymbol{d}}$. Therefore it would be necessary to repeat the analysis of the previous section for each dipole direction found. To reduce the simulation effort, we rely on the following method instead.

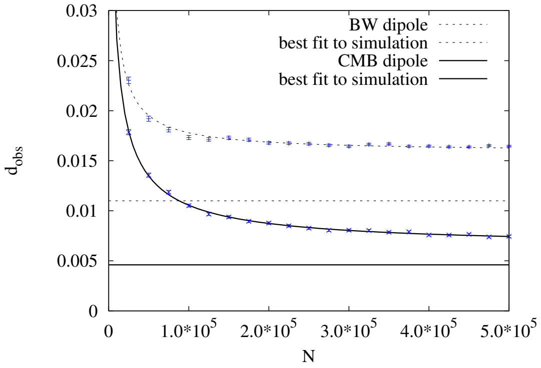

Fig. 4. Amplitude bias of the 3-dimensional estimator for the masked NVSS geometry of Singal (2011). Data represent mean and empirical variance of 1000 simulations for each N. A function $d_{\mathrm{obs}}(N) = \sqrt{(KD)^2 + 9A^2/N}$ is fitted to the simulated data, with best-fit values $A = 0.883 \pm 0.006$, $KD = (0.642 \pm 0.005) \times 10^{-2}$ and $A = 0.847 \pm 0.016$, $KD = (1.59 \pm 0.008) \times 10^{-2}$ for the expected kinetic radio dipole and the radio dipole measured by Blake & Wall (2002), respectively. The simulated dipole amplitudes, without masking, are indicated by the horizontal lines.

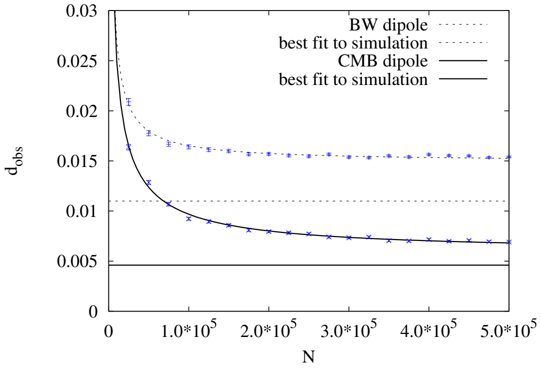

Fig. 5. Amplitude bias of the 2-dimensional estimator for the masked NVSS geometry of Singal (2011). Data represent mean and empirical variance of 1000 simulations for each N. A function $d_{\mathrm{obs}}(N) = \sqrt{(KD)^2 + 9A^2/N}$ is fitted to the simulated data, with best-fit values $A = 0.810 \pm 0.009$, $KD = (0.589 \pm 0.008) \times 10^{-2}$ and $A = 0.745 \pm 0.014$, $KD = (1.493 \pm 0.006) \times 10^{-2}$, for the expected kinetic radio dipole and the dipole measured by Blake & Wall (2002), respectively. The simulated dipole amplitudes, without masking, are indicated by the horizontal lines.

For the full, as well as for the masked sky, surveys with 10^6 sources were simulated. This choice guarantees that we investigate masking effects and not effects due to shot noise. The mean dipole amplitudes are determined for 10^3 simulated full and masked sky surveys, respectively. The ratio of the masked sky mean amplitude to the full sky mean amplitude is denoted $\tilde{k}$. This ratio provides a first approximation to the masking factor.

$$\tilde{k} \equiv \frac{\sqrt{k^2 d^2 + \frac{9}{N^2} \langle R^{\mathrm{random}} \rangle^2}}{\sqrt{d^2 + \frac{9}{N^2} \langle R^{\mathrm{random}} \rangle^2}}. \tag{44}$$

The influence of the random dipole tends to bias $\tilde{k}$ towards 1 (as can be easily seen in the limit of a small number of sources).

This bias can be compensated by rewriting the above formula into

$$k = \sqrt{\tilde{k}^2 + \frac{9\langle R^{\rm random}\rangle^2}{d^2N^2}\left(\tilde{k}^2 - 1\right)}. \tag{45}$$

The values of N and d are input parameters of the simulation. From the last section we know the values of $\langle R^{\rm random}\rangle$ for the three- as well as for the two-dimensional case. Therefore we can transform the approximated masking factor $\tilde{k}$ into the unbiased masking factor k.

6. Dipole from a flux weighted estimator

Let us now turn to a discussion of the flux weighted estimator (16), which was used by Singal (2011).

We first take a closer look at the theoretically expected value of the flux dipole $\boldsymbol{d}_{\rm flux}$. For simplicity we assume full sky coverage. For a large number of sources,

$$\hat{\boldsymbol{d}} \cdot \sum_{i=1}^{N} S_i \boldsymbol{r}_i \approx \int_{4\pi} {\rm d}\Omega \int_{S_{\rm min}}^{S_{\rm max}} {\rm d}S \, \frac{{\rm d}^2N}{{\rm d}\Omega {\rm d}S} S \cos\theta, \tag{46}$$

where θ is the angle between a source and the dipole direction $\hat{\boldsymbol{d}}$.

We now determine the number of sources per flux and solid angle as a function of the observer velocity. At zeroth order in velocity, this density $n(S)$ is isotropic. As for the number counts, stellar aberration and the Doppler effect have to be taken into account. Stellar aberration gives rise to

$$\frac{{\rm d}^2N}{{\rm d}\Omega {\rm d}S} \approx n(S)\left(1 + 2\frac{v}{c}\cos\theta\right). \tag{47}$$

The relativistic Doppler effect alters the observed fluxes. When we observe a source in the direction of motion, we measure a higher flux than if we were at rest with respect to the isotropic and homogeneous Universe. We relate the observed flux S_0 to the flux that is measured by an observer with vanishing peculiar motion,

$$S_{\rm rest} \approx S_0 - S_0(1+\alpha)\frac{v}{c}\cos\theta. \tag{48}$$

We assume the power law $n(S) = aS^{-\tilde{x}}$ to hold for observers at rest and Taylor expand around the observed flux

$$n(S_{\rm rest}) \approx n(S_0)\left[1 + \tilde{x}(1+\alpha)\frac{v}{c}\cos\theta\right]. \tag{49}$$

If the assumed power law holds for all sources of a survey, then $\tilde{x} = 1 + x$, with x as defined above in (4). Combining the Doppler effect and the stellar aberration leads to

$$\frac{{\rm d}^2N}{{\rm d}\Omega {\rm d}S} = n_0(S_0)\left[1 + (2 + \tilde{x}(1+\alpha))\frac{v}{c}\cos\theta\right] + O\left(\left(\frac{v}{c}\right)^2\right). \tag{50}$$

This result only holds under the assumption of a power law behaviour of the number counts. It is crucial to keep this in mind.

6.1. NVSS

Let us now see, if we are allowed to make this assumption for the analysis of NVSS data. The plot in Fig. 6 demonstrates that the power law is not valid for the flux range used in the analysis of Singal (2011), i.e. fluxes up to 1 Jy. Actually the slope steepens for the larger fluxes considered. The best fit power-law gives a reduced chi-squared value of $\chi^2 = 122$. That means that the observed data cannot be fitted by a power law.

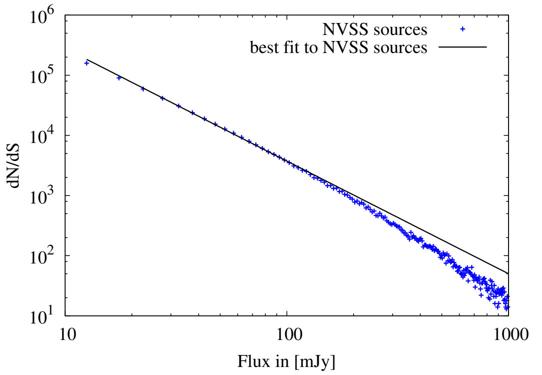

Fig. 6. Differential number counts of the NVSS catalogue, $S_{\rm min}$ = 10 mJy, best fit values for $f(s) = a \cdot s^{-\tilde{x}}$ with 25 mJy $< S <$ 1000 mJy are $a = 2.1 \times 10^7$ and $\tilde{x} = 1.9$.

Thus Singal's assumption $\tilde{x} \approx 1$ does not hold for two reasons. Firstly, for a pure power law we would expect $\tilde{x} = 1 + x \approx 2$, which is close to what we find: $\tilde{x} \approx 1.9$. Secondly, the power-law assumption only applies to about one half of the data.

In conclusion, the result of unexpectedly large amplitudes in Singal (2011) could partly be explained by this two effects. With power law behaviour one should use $\tilde{x} = 1.9$ or larger to also account for the steepening of the spectral index at high fluxes, which increases the expectation value by

$$\frac{\langle \boldsymbol{d}_{\rm obs}\rangle|_{\tilde{x}=1.9}}{\langle \boldsymbol{d}_{\rm obs}\rangle|_{x=1}} > 1.4. \tag{51}$$

The results of the flux weighted estimator from Singal (2011) should be reduced by at least a factor of 1.4.

Compared to the estimator of Crawford, the estimator (16) stresses sources with high flux. To avoid the domination of a small number of sources, sources with $S > 1000$ mJy are not taken into account. Nevertheless, this estimator is stressing bright sources. These sources are, on average, nearer than the rest. Hence (16) might be dominated by nearby sources and by atypically bright ones. This seems to be yet another weakness of this estimator, since the local universe is anisotropic.

7. Dipole estimates from NVSS and WENSS

7.1. 3D linear estimates

We are now in a position to check the three dimensional estimations of the radio dipole in the NVSS catalogue. As we have shown above, the estimator used by Gibelyou & Huterer (2012) (17) gives rise to a biased dipole direction and thus is not further considered in this work. The flux weighted estimator (16) is also of limited use, as the NVSS data cannot be described by a power-law over all fluxes of interest. We thus focus here on the simplest linear estimator (15).

In order to obtain an unbiased direction estimate, the cut sky geometry of Singal (2011) is adopted. The masking factor k is determined for every measured dipole anisotropy direction, as described in 5.3.1. The pure estimator results $d_{\rm 3D}$ are then corrected for the masking bias and we obtain $d_{\rm 3D}^{\rm cor}$.

All results for right ascension agree within their error bars. The same holds true for the dipole amplitudes. This

Table 4. Dipole direction and amplitude from NVSS.

Flux (mJy)	N	RA (°)	Dec (°)	d_{3D} (10^{-2})	k	d^{cor}_{3D} (10^{-2})
50	91 662	170 ± 23	−17 ± 23	2.78	1.38	2.0 ± 0.8
40	115 917	156 ± 26	−18 ± 26	2.23	1.29	1.7 ± 0.8
35	133 022	156 ± 22	−11 ± 22	2.46	1.32	1.9 ± 0.7
30	155 120	156 ± 19	−2 ± 19	2.63	1.35	1.9 ± 0.7
25	185 649	158 ± 19	−2 ± 19	2.38	1.34	1.8 ± 0.6
20	229 557	153 ± 18	2 ± 18	2.31	1.30	1.8 ± 0.6
15	298 289	149 ± 18	17 ± 18	2.02	1.28	1.6 ± 0.5

Notes. The estimator (15) was used. Excluded are sources with $|\delta| > 40^\circ$ and $|b| < 10^\circ$ (J2000).

self-consistency indicates the absence of significant systematic errors. Unfortunately, we can not state the same for the declination results. One observes an significant increase in declination with respect to deceasing flux limits. This effect is very likely due to a relic of the NVSS survey procedure. Sources below $\delta = -10^\circ$ were measured by means of a different alignment of the Very Large Array. The source density is therefore smaller in this area. Therefore it is expected that the dipole measurement will show increasing values of declination at the fainter flux limits. This makes it hard to trust the declination results below a flux limit of 25 mJy (note that there is no significant difference between 20 mJy and 30 mJy).

The results of Table 4 can be compared to those in Table 2. Number of sources and direction results are almost the same. Deviations could be explained by minor differences in the precise form of the mask. We used a different method for estimating uncertainties in the direction and amplitude measurement, than those used by Singal (2011). Since our method (described above) is more conservative, we obtain larger errorbars. All dipole amplitudes in this table are slightly below those from Table 2. In Singal (2011) a different method was used to obtain the dipole amplitude from the estimator (15), which can explain this discrepancy. In principle we can recover the results of Singal (2011) and confirm an unexpectedly high dipole amplitude.

7.2. 2D linear estimates

A disadvantage of the NVSS catalogue is that the sampling depth changes at $\delta = -10^\circ$ (less sensitivity at lower declinations). This could lead to a directional bias of the NVSS data analysis and thus it is interesting to also use the two dimensional estimator presented in this work, as this effect cannot lead to a bias in this case. For the WENSS analysis, a three dimensional linear estimator cannot avoid directional bias.

7.2.1. NVSS

A major advantage of the estimator $\boldsymbol{R}_{2D}$ is that it does not require a north-south symmetry of the catalogue. Therefore, the declination limit of the NVSS catalogue is no problem.

As the estimator $\boldsymbol{R}_{2D}$ requires a point symmetry around the north pole, we cannot remove the Galactic plane only. For each removed point we also need to subtract the point which is 180° away. When we do so, a second plane occurs, which we call the counter Galactic plane (CG). A HEALPix[1] map of the remaining NVSS sources can be seen in Fig. 7. The colour of the pixels encodes the number of sources per pixel.

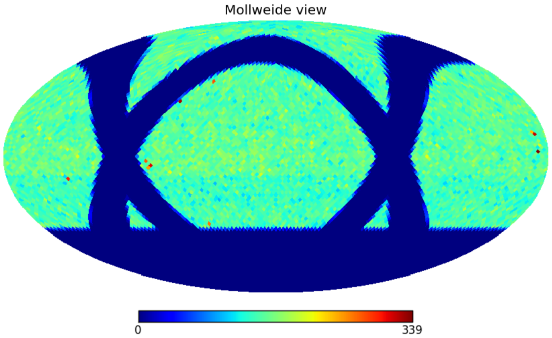

Fig. 7. Map of the number counts in HEALPix pixels from NVSS. The pixel size corresponds to $N_{side} = 32$. Shown are equatorial coordinates at epoch J2000. The NVSS contains data at $\delta > -40^\circ$ and the Galactic plane and a "counter galaxy" are masked (CG mask) in order to avoid Galactic contamination and to restore point symmetry with respect to the zenith.

Table 5. Dipole right ascension and amplitude $d \sin\theta_d$ from NVSS.

Flux (mJy)	N	RA (°)	d_{2D} (10^{-2})	k	d^{cor}_{2D} (10^{-2})
50	96 337	171 ± 19	2.63	1.42	1.9 ± 0.7
40	121 831	146 ± 20	2.28	1.29	1.8 ± 0.7
35	139 851	152 ± 17	2.49	1.28	1.9 ± 0.6
30	163 208	153 ± 15	2.55	1.28	2.0 ± 0.6
25	195 245	155 ± 14	2.45	1.29	1.9 ± 0.5
20	241 399	150 ± 14	2.25	1.26	1.8 ± 0.5
15	313 724	148 ± 15	1.86	1.21	1.5 ± 0.4
10	447 459	133 ± 14	1.67	1.10	1.5 ± 0.4

Notes. The 2D estimator (31) is used and all sources with $\delta > -40^\circ$, except the Galactic and counter Galactic planes (CG mask), are included.

An alternative would be the mask used by Singal (2011). That mask is a combination of two great cycles and would therefore also work for $\boldsymbol{R}_{2D}$. However, it turns out that the mask with the CG removes fewer sources. Thus we decided to use the CG mask.

The next step is to evaluate the masking correction k of the CG mask. As this factor depends on the right ascension and on the declination of the dipole anisotropy, we need some additional information. From $\boldsymbol{R}_{2D}$ we estimate the right ascension. As the declination cannot be evaluated with $\boldsymbol{R}_{2D}$, we use the declination as provided by the three dimensional estimator in order to determine k. These values are certainly not exact, since a different mask is used now. The influence of a small change in dipole declination on the evaluated factor k is discussed in Sect. 7.2.2.

We reduce the dipole amplitude of the 2D estimator by the masking factor k and obtain the masking corrected amplitude d^{cor}_{2D}. The results of this procedure for the NVSS catalogue and different flux limits can be found in Table 5.

Obtained right ascensions and amplitudes are stable with respect to different flux limits. For all flux limits ≥15 mJy, the estimated right ascension of the radio dipole is in agreement with the CMB prediction of RA = 168°. Only when we include sources as faint as 10 mJy, we find a 3σ deviation. However, we know that the catalogue is incomplete at its faint end.

The masking corrected dipole amplitudes d^{cor}_{2D} are significantly above the CMB prediction. To some extent this is

---

[1] http://healpix.jpl.nasa.gov

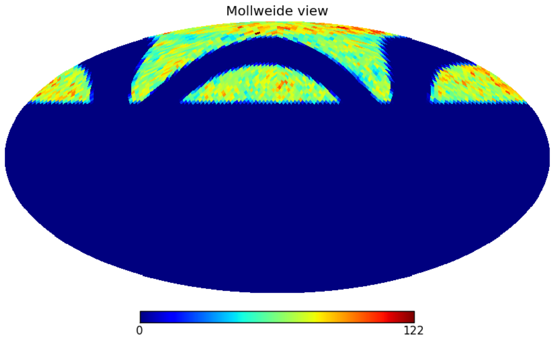

Fig. 8. Map of the number counts in HEALPix pixels from WENSS. The pixel size corresponds to $N_{\rm side} = 32$. Shown are equatorial coordinates at epoch B1950. The WENSS contains data at $\delta > 30°$ and the Galactic plane and a "counter galaxy" are masked (CG mask) in order to avoid Galactic contamination and to restore point symmetry with respect to the zenith.

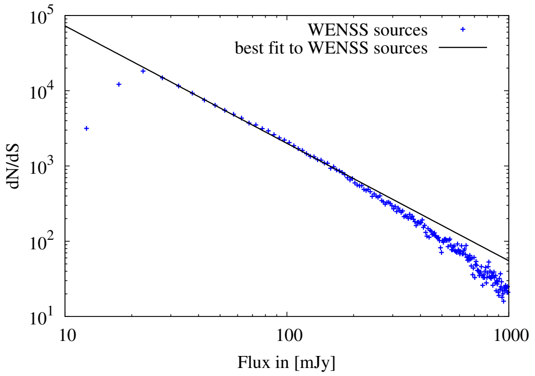

Fig. 9. Differential number counts of the WENSS catalogue, $S_{\rm min} = 5$ mJy, best fit values for $f(s) = a \cdot s^{-\tilde{x}}$ with 25 mJy $< S <$ 1000 mJy are $a = 2.6 \times 10^6$ and $\tilde{x} = 1.6$.

expected due to the discussed amplitude bias. A detailed discussion is presented in the next section.

7.2.2. WENSS

We finally present the first estimation of the radio dipole from the WENSS catalogue. We cannot use the three dimensional linear estimators on this catalogue, since it only contains sources with Dec > 28°. The two dimensional estimator on the other hand can be used here. Again, we need to remove the Galactic plane and the counter Galactic plane to reestablish a symmetry around the north pole. The remaining WENSS catalogue is shown in Fig. 8.

To choose the best flux limit, we analyse the differential number counts between 10 mJy and 1000 mJy. Figure 9 shows that the WENSS catalogue seems to be incomplete below 25 mJy. In Rengelink et al. (1997) the completeness of the WENSS catalogue is claimed to hold only above a limit of 30 mJy. From Fig. 9 we infer that a simple power law also applies to the source counts between 25 and 30 mJy and thus we include sources down to a flux limit of 25 mJy in our analysis.

Table 6. Masking correction k for WENSS with CG mask and a dipole with RA = 120°.

Dec	45°	30°	5°	0°	−5°	−30°	−45°
k	0.50	0.48	0.45	0.44	0.44	0.47	0.51

Table 7. Dipole estimate from WENSS based on 2D estimator using peak flux values for all sources with $\delta > 30°$, except those in the Galactic and counter Galactic planes (CG mask).

Flux (mJy)	N	RA (°)	$d_{\rm 2D}$ (10^{-2})	k	$d_{\rm 2D}^{\rm cor}$ (10^{-2})
40	67 052	124 ± 51	1.31	0.45	2.9 ± 2.3
35	73 653	123 ± 46	1.36	0.47	2.9 ± 2.1
30	81 863	122 ± 48	1.24	0.45	2.8 ± 2.1
25	92 600	117 ± 40	1.36	0.47	2.9 ± 1.9

Notes. Our WENSS analysis uses positions at epoch B1950.

We cannot obtain information on the declination of the dipole from the WENSS catalogue by means of the two dimensional estimator applied in this work. This could in principle be a problem for the determination of the masking factor k. Therefore, we further investigated the effect of different dipole declinations. Assuming the WENSS symmetry and a right ascension of 120° (close to the results given in Table 7), we calculated k for 7 different values of declination, see Table 6. For this mask, the dependence of k on the right ascension of the dipole is relatively small, compared to shot noise uncertainties. We assume dec = 0° for the determination of k, based on the expectation from the CMB dipole and the NVSS radio dipole estimates.

The results of the WENSS analysis are presented in Table 7. Although the WENSS catalogue covers only one fourth of the sky, we find that it can be used for the estimation of the radio dipole. A problem is the limited number of sources that are left after masking the galaxy and restoring the required symmetry of the catalogue. This leads to larger error bars, compared with the NVSS estimates. We can conclude that the observed dipole anisotropy in the WENSS catalogue is in agreement with the measurements from NVSS, which is a nontrivial statement, as we are probing radio sources at different frequencies (325 MHz vs. 1.4 GHz).

8. Comparison of results

We summarize the various results from the literature and this work in Table 8. The results of this work are highlighted with bold faced letters. For comparison we focus on the flux limits of 25 mJy and 15 mJy.

All estimated dipole directions, both from the NVSS and from WENSS are in good agreement with each other and with the direction from the CMB dipole, with the exception of the result from Gibelyou & Huterer (2012). As explained in Sect. 5.2, their estimator shows a directional bias. We did not investigate any further, whether this bias invalidates their findings at a rather low flux limit. Our analysis based on the three dimensional estimator applied to NVSS and using the mask defined by Singal (2011) gives (RA, Dec) = (158° ± 19°, −2° ± 19°).

For the amplitude of the radio dipole, the situation is more contrived. Here we focussed on the study of linear estimators and showed that all linear estimators under investigation returned a biased estimate of the amplitude. The amplitude estimators of Blake & Wall (2002) and Gibelyou & Huterer (2012) are unbiased, but the latter one uses a biased direction estimate as an

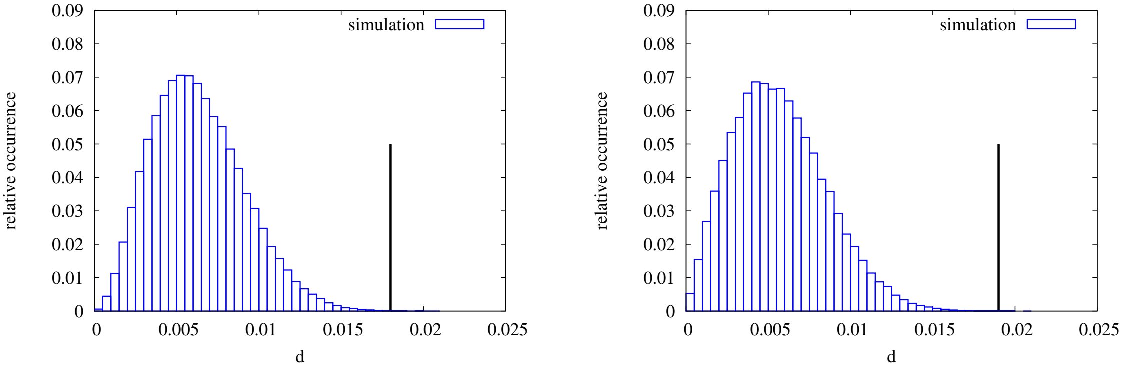

Fig. 10. Histogram of dipole amplitudes for 100,000 simulations of the three dimensional (*left*) and two dimensional (*right*) estimator, assuming the CMB expectation and a slope of $x = 1.1$, with 185 649 (*left*) and 195 245 (*right*) sources per simulation and appropriate masks. The black vertical lines are the NVSS results of this work.

Table 8. Comparison of results.

Source	Flux > (mJy)	N	RA (°)	Dec (°)	d (10^{-2})
NVSS					
BW	25	197 998	158 ± 30	−4 ± 34	1.1 ± 0.3
SIN	25	185 474	158 ± 10	−2 ± 10	1.8 ± 0.4
SIF	25	184 237	159 ± 10	−7 ± 9	2.2 ± 0.6
SIF*	**25**	**184 237**	**159 ± 10**	**−7 ± 9**	**1.6 ± 0.5**
3DS	**25**	**185 649**	**158 ± 19**	**−2 ± 19**	**1.8 ± 0.6**
2DCG	**25**	**195 245**	**155 ± 14**	…	**1.9 ± 0.5**
GH	15	211 487	117 ± 20	6 ± 14	2.7 ± 0.5
3DS	**15**	**298 289**	**149 ± 18**	**17 ± 18**	**1.6 ± 0.5**
2DCG	**15**	**313 724**	**148 ± 15**	…	**1.5 ± 0.5**
WENSS					
2DCG	**25**	**92 600**	**117 ± 40**	…	**2.9 ± 1.9**
expected					
NVSS	…	…	168	−7	0.48 ± 0.04
WENSS	…	…	168	−7	0.42 ± 0.03

Notes. Radio dipole from NVSS: BW (Blake & Wall 2002), SIN (Singal 2011) number counts, SIF (Singal 2011) flux weighted number counts, SIF* corrects SIF for slope (this work), 3DS three-dimensional estimator, mask adopted from Singal (2011) (this work), 2DCG two-dimensional estimator, CG mask (this work), GH (Gibelyou & Huterer 2012); Radio dipole from WENSS: 2DCG two-dimensional estimator, CG mask (this work). The expectations for a purely kinetic radio dipole are given at the bottom of the table.

input and is thus of limited interest. Besides bias, we identified another effect that reduces the dipole amplitude found by the flux estimator used in Singal (2011). We reduced the result of this estimator by a factor of 1.4, due to the fact that the appropriate exponent of the differential number count is given by $\tilde{x} = x + 1$ (see Sect. 6). With this correction, the result of the flux weighted estimator (denoted by SIF* in Table 8) is now in agreement with the result of Blake & Wall (2002).

Our three dimensional estimate with the masking of Singal (2011) gives rise to $d = (1.8 \pm 0.6) \times 10^{-2}$. One should keep in mind that this is a biased result, thus one cannot naively compare it to the expected amplitude. To figure out if our result is consistent with the null hypothesis that the radio sky is statistically isotropic, modified by the kinetic effects of our proper motion (measured via the CMB dipole), we performed 100 000 Monte Carlo simulations. The corresponding histogram is shown in Fig. 10. We find that only 21 of those realizations contain a dipole higher than the measured one and thus we can exclude that the estimated radio dipole is just due to our proper motion and amplitude bias at 99.6% CL. This is actually very puzzling, as the direction of the radio dipole agrees with the direction of the CMB dipole within the measurement error.

We can redo this analysis with the null hypothesis that the radio dipole was accurately measured by Blake & Wall (2002). This time we find that 3402 out of 100 000 realisations are higher than our measured dipole. If we increase the implemented velocity towards the upper one sigma bound of the dipole amplitude from Blake & Wall (2002), we observe every sixth simulation to be above our own measurement (16%). Therefore our result is in agreement with Blake & Wall (2002).

Before we turn to the discussion of potential explanations, let us inspect the dipole amplitudes from the two dimensional estimator. The dipole amplitudes estimated with the two dimensional estimator are also in agreement with the results of Singal (2011) and Blake & Wall (2002). We find $d \sin\vartheta_{\rm d} = (1.9 \pm 0.5) \times 10^{-2}$ for the NVSS analysis and $d \sin\vartheta_{\rm d} = (2.9 \pm 1.9) \times 10^{-2}$ for WENSS, which translate into lower limits on d. Thus, the results from the WENSS catalogue are in agreement with the radio dipole found in the NVSS catalogue. This is encouraging as they are prepared at different instruments and probe different frequencies.

In Figs. 10 and 11 we present the corresponding results from 100 000 Monte Carlo simulations for the geometries of the NVSS and WENSS two dimensional estimators. In both cases we find that the amplitude bias is not enough to explain the difference between the observed and the expected amplitude. In the case of NVSS the null hypothesis (isotropic sky plus proper motion dipole) is ruled out at 99.6% CL, while for the WENSS analysis it is inconsistent at 98.1% CL.

The two dimensional estimation (2DCG), using the NVSS catalogue, is also compared to simulations, assuming the results from Blake & Wall (2002). We observe 1141 and 7024 out of 100 000 simulations to give a dipole above our measurement for the assumptions of $d_{\rm true} = 1.1 \times 10^{-2}$ and $d_{\rm true} = 1.4 \times 10^{-2}$, respectively. Therefore, the result of our two dimensional estimator is not in contradiction to Blake & Wall (2002).

9. Conclusion

We conclude that the task to measure the cosmic radio dipole remains relevant and we expect that interesting information on

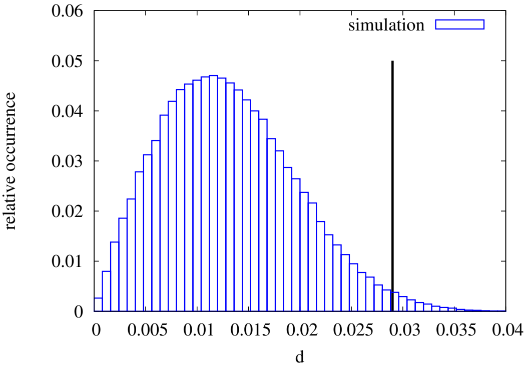

Fig. 11. Histogram of dipole amplitudes from 100 000 simulations for the dimensional estimator, assuming the CMB expectation, a slope of $x = 0.8$, 92,482 sources per simulation and the CG masking form for the WENSS catalogue. The black vertical line is the WENSS result of this work.

cosmology can be extracted from this measurement. All measurements so far point towards a higher radio dipole amplitude than expected, when we assume that the cosmic radio dipole is just due to our peculiar motion with respect to the rest frame defined by the CMB. This is quite puzzling, as the orientation of the radio dipole agrees with the orientation of the CMB dipole within measurement errors. This is the case for the NVSS and the WENSS analysis, two radio point source catalogues that cover ~3π and ~π of the sky, respectively. They contain information at different frequencies (1.4 GHz and 325 MHz) and have been put together by different instruments and thus provide a strong constraint on systematic issues.

Our detailed analysis of various linear dipole estimators (Crawford 2009; Singal 2011; Gibelyou & Huterer 2012) for three dimensional estimates $(\alpha_{\rm d}, \delta_{\rm d}, d)$ and a new linear estimator for a two dimensional estimate $(\alpha_{\rm d}, d \cos \delta_{\rm d})$ had to tackle several non-trivial issues. We investigated issues of directional bias, amplitude bias and masking. There is still room to optimize the masking of the galaxy. We did not look into quadratic estimators, as used by Blake & Wall (2002). Our studies did not incorporate the uncertainties in point source positions, as we expect that they are subdominant (their magnitude is well below the effect of aberration, see e.g. Rengelink et al. 1997). The measurement error of the flux is also expected to be subdominant as we included sources with flux above 15 mJy only. In the case of NVSS these are a factor 6 above the 5σ point source detection limit, in case of WENSS it is a factor of 1.4. The number of point sources considered in our analysis is about 190 000 for NVSS and 92 000 for WENSS. Putting all those facts together, we consider the NVSS analysis to be more reliable. Nevertheless, the results of the WENSS analysis are fully consistent with our results from NVSS.

Our result (3DS) for the NVSS catalogue is $(\mathrm{RA}, \mathrm{Dec}, d) = (154° \pm 19°, -2° \pm 19°, (1.8 \pm 0.6) \times 10^{-2})$. Thus we conclude that the observed amplitude of the radio dipole exceeds the expected amplitude by about a factor of four. We could imagine that this might be due to the structure that causes our proper motion, which in a simple model of our Hubble patch would certainly be aligned with the direction of proper motion. However, all attempts to identify a "great attractor" by means of other observations (optical, infra-red, X-ray) have failed so far. Of all those probes, the radio surveys are definitely the deepest probe of the Universe, as the mean redshift of NVSS sources is estimated to be 1.2 by de Zotti et al. (2010) and 1.5 by Ho et al. (2008). To explain the observed excess radio dipole by contributions from local structure, we would need a density contrast of order 0.05 at scales extending to about $z \approx 0.3$, which does not seem plausible. Without a detailed study of the redshift distribution of the radio sources it is impossible to judge whether this finding is actually in agreement with the current standard model of cosmology.

An example of such a scenario is provided by Wiltshire et al. (2012). They claim that the spherically averaged Hubble law on $<100/h$ Mpc scales is significantly closer to uniform in the Local Group frame as compared to the CMB frame and on this basis have suggested a non-kinematic contribution to the CMB dipole. In this case the CMB dipole could differ from the cosmic radio dipole.

Another reason for the large amplitude of the radio dipole could be that the linear estimators considered in this work do not assume the deviation from isotropy to be a pure dipole. Thus higher multipole moments also contribute to the measured amplitude.

It has been found from the analysis of the CMB that quadrupole, octopole and a few more low ℓ-multipoles seem not to be orientated randomly on the sky, but show some unexpected alignments (Schwarz et al. 2004; Bennett et al. 2011; Copi et al. 2010) among themselves and with the CMB dipole direction. Thus it might not be surprising that also the dominant anisotropy direction of the radio sky lines up.

It is evident that it would be crucial to repeat this investigation with new and even deeper radio catalogues, which provide more sources. In the near future there will be three large sky surveys available (Raccanelli et al. 2012). A multi-wavelength study will be possible based on the Multifrequency Snapshot Sky Survery (MSSS) of the International LOFAR Telescope and with the LOFAR Tier-1 survey. The Australian Square Kilometre Array (SKA) Pathfinder (ASKAP) will produce the Evolutionary Map of the Universe (EMU) and the Westerbrok Synthesis Radio Telescope (WSRT) equipped with the Apertif system will compile the Westerbrok Observations of the Deep Apertif Northern sky survey (WODAN) catalogue.

The multi-wavelength surveys will also allow us to directly measure the spectral index α, which has to be known to connect the measured amplitude to the kinetic dipole. A steepening of the spectral index for the lowest flux sources would increase the expected kinetic amplitude. HI surveys will have the advantage that they will also provide redshift information on top of positions and fluxes and we will be able to study the evolution of the radio dipole as a function of redshift out to redshifts of a few. Beyond that SKA will increase the number of sources in such a survey by orders of magnitude. All these surveys will reduce the random dipole contribution, improve on systematics, and allow us to settle the question: Is the radio dipole in agreement with the CMB dipole?

Acknowledgements. We thank David J. Bacon, Dragan Huterer, Matt J. Jarvis, Seshadri Nadathur, Huub Röttgering and Ashok K. Singal for fruitful comments and discussions and Anne-Sophie Balleier for help with Healpy and the generation of maps of the NVSS and WENSS number counts. The CAMB code, and the Healpy and HEALPix (Górski et al. 2005) packages have been used to estimate the concordance value of the CMB primordial dipole and to produce the NVSS and WENSS maps of the sky. We acknowledge financial support from Deutsche Forschungsgemeinschaft (DFG) under grants IRTG 881 'Quantum Fields and Strongly Interacting Matter' and RTG 1620 'Models of Gravity', as well as from the Friedrich Ebert Stiftung.

Appendix A: Monte Carlo simulations

We used the pseudorandom number generator Mersenne Twister for all Monte Carlo simulations. One simulated source consists of two position coordinates and one flux value. The coordinates will be drawn from an uniform distribution, leading to an isotropic sky for a catalogue with many sources. To obtain a desired number count power law like (4) with a certain slope x, we calculate the flux S using a random number A (choosen between 0 and 1) by

$$S_{\mathrm{rest}} = S_{\mathrm{L}}(1 - A)^{-x}, \tag{A.1}$$

where S_{L} is a flux value 20% below the simulated flux limit. The simulation also creates sources, which only due to Doppler shifting are counted in the final catalogue, because this value of S_{L} lies below the simulated flux limit. Lowering S_{L} further increases computational time and is not necessary, as long as the simulated velocity v is below $0.1c$.

The two physical effects (Doppler shift and spherical aberration) will be implemented separately. In cooperating the Doppler effect is straightforward, since it only affects the flux values of each source depending on the angle θ between the source and the velocity direction, i.e.

$$S_{\mathrm{obs}}(\nu_{\mathrm{obs}}) = S_{\mathrm{rest}} \left(\frac{1 + \frac{v}{c}\cos(\theta)}{\sqrt{1 - (\frac{v}{c})^2}} \right)^{1+\alpha}. \tag{A.2}$$

In the simulation α is fixed to 0.75 for all sources. The velocity direction and amplitude can by chosen be the user.

To model the relativistic effect of stellar aberration one has to change the position of each radio source. The aberration formula is

$$\tan(\theta') = \frac{\sin(\theta)\sqrt{1 - (\frac{v}{c})^2}}{\frac{v}{c} + \cos(\theta)}, \tag{A.3}$$

where θ' is the new angle between the velocity direction and the radio source. Forth, the position of a radio source is translated into Cartesian coordinates by assuming that it lies on a unit sphere. Then a straight line from this point ($\boldsymbol{P}$) to the velocity direction on the sphere ($\boldsymbol{V}$) is constructed depending on a parameter t

$$\boldsymbol{r}(t) = \boldsymbol{P}(1 - t) + \boldsymbol{V}t. \tag{A.4}$$

On this line we choose a t' in such a way that $\boldsymbol{r}(t')$ points towards the new position. The value of t' can be determined by

$$\boldsymbol{r}(t') \cdot \boldsymbol{V} = r'(t')\cos(\theta') \tag{A.5}$$

$$\rightarrow t' = \frac{r'(t')\cos(\theta') - \cos(\theta)}{1 - \cos(\theta)} \tag{A.6}$$

with $r'(t') = \sqrt{\boldsymbol{r}'^2(t')}$. This equation is solved by

$$t'_1 = \frac{\sin(\theta - \theta')}{\sin(\theta - \theta') + \sin(\theta')} \vee t'_2 = \frac{\sin(\theta + \theta')}{\sin(\theta + \theta') - \sin(\theta')}. \tag{A.7}$$

We know that for $\theta = \theta'$ the result of t' must always be 0. Therefore the correct solution is $t' = t'_1$. Now one has to transform $\boldsymbol{r}(t')$ back into spherical coordinates in order to find the new position of the radio source. The new declination ϑ' is then (the index v stands for the velocity direction):

$$\vartheta' = \arccos\left(\frac{1}{r'}[(1 - t')\cos(\vartheta) + t'\cos(\vartheta_{\mathrm{v}})] \right) \tag{A.8}$$

and the new right ascension φ':

$$\varphi' = \arcsin\left(\frac{(1 - t')\sin(\vartheta)\sin(\varphi) + t'\sin(\vartheta_{\mathrm{v}})\sin(\alpha_{\mathrm{v}})}{r'\sin(\vartheta')} \right). \tag{A.9}$$

This way one obtains a simulated sky, including the effect of the observers movement. Now one can feed the different estimators with those sky simulations and obtain the resulting dipole vectors.

References

Baleisis, A., Lahav, O., Loan, A. J., & Wall, J. V. 1998, MNRAS, 297, 545
Bennett, C. L., Hill, R. S., Hinshaw, G., et al. 2011, ApJS, 192, 17
Blake, C., & Wall, J. 2002, Nature, 416, 150
Condon, J. J., Cotton, W. D., Greisen, E. W., et al. 2002, VizieR Online Data Catalog, VIII/065
Copi, C. J., Huterer, D., Schwarz, D. J., & Starkman, G. D. 2010, Adv. Astron., 2010, id. 847541
Crawford, F. 2009, ApJ, 692, 887
de Zotti, G., Massardi, M., Negrello, M., & Wall, J. 2010, A&A Rev., 18, 1
Ellis, G. F. R., & Baldwin, J. E. 1984, MNRAS, 206, 377
Fixsen, D., & Mather, J. 2002, ApJ, 581, 817
Francis, C., & Peacock, J. 2010, MNRAS, 406, 14
Garn, T., Green, D. A., Riley, J. M., & Alexander, P. 2008, MNRAS, 383, 75
Gibelyou, C., & Huterer, D. 2012, MNRAS, 427, 1994
Górski, K. M., Hivon, E., Banday, A. J., et al. 2005, ApJ, 622, 759
Hinshaw, G., Weiland, J. L., Hill, R. S., et al. 2009, ApJS, 180, 225
Hirata, C. M. 2009, , J. Cosmol. Astropart. Phys., 9, 11
Ho, S., Hirata, C., Padmanabhan, N., Seljak, U., & Bahcall, N. 2008, Phys. Rev. D, 78, 043519
Raccanelli, A., Zhao, G.-B., Bacon, D. J., et al. 2012, MNRAS, 424, 801
Rakic, A., Rasanen, S., & Schwarz, D. J. 2006, MNRAS, 369, L27
Rengelink, R. B., Tang, Y., de Bruyn, A. G., et al. 1997, A&AS, 124, 259
Rubart, M. 2012, Master Thesis, Universität Bielefeld
Schwarz, D. J., Starkman, G. D., Huterer, D., & Copi, C. J. 2004, Phys. Rev. Lett., 93, 221301
Singal, A. K. 2011, ApJ, 742, L23
Stewart, J. M., & Sciama, D. W. 1967, Nature, 216, 748
Wiltshire, D. L., Smale, P. R., Mattsson, T., & Watkins, R. 2012 [arXiv:1201.5371]

2.2 Flux-weighted estimator correction

There was a critical response (Singal 2014) in the literature concerning section 6 of Rubart & Schwarz (2013). In that part of our work we investigated the flux-weighted linear estimators, which are similar to the linear number-count estimators, but weight each source with the measured flux value,

$$\vec{R}_{\text{flux}} = \sum S_i \vec{\hat{r}}_i. \tag{2.1}$$

We claimed that the expectation value for the amplitude of this estimator is by a factor of about 1.4 above the corresponding expectation for a pure number count estimator. It turned out that this factor is not correct. In Rubart & Schwarz (2013) we Taylor expanded the number density of the observed sources for the changed flux values. Since the flux estimator in question also has an upper flux limit, this method is not valid in this case. Assuming the number density for the observed survey does obey a power law for the whole range of used fluxes, the kinematic dipole does not change the observed flux values in any direction. The estimator always considers sources between an upper and a lower flux limit and those sources do behave like $n(>S) \propto S^{-x}$ in any case. The only effects playing a role are (a) the aberration leading to a change in position of radio sources and (b) the Doppler-effect leading to an increased observed number of sources in a certain direction. Those effects are the same for the number count estimator and therefore both methods should give the same expectation value.

In order to clarify this debate, we also investigated the expectation of the flux estimator with simulated radio maps in comparison to a pure number-count estimator. The simulated full-sky maps had 10^6 sources each and a simulated peculiar observer velocity of $v = 1200$ km/s. Those high values were chosen in order to keep the shot noise contribution small. In the simulated maps the power law $n(>S) \propto S^{-x}$ (with $x = 1$) was used for drawing all flux values and thereby the simulation fulfilled the assumptions mentioned above. The theoretical dipole amplitude in table 2.1 was computed using equation (1.6) and corresponds to the case, without any correction factor applied and without a shot-noise bias.

First of all we clearly see in table 2.1 that the simulations do not support any need for a correction factor between those two estimators. The

	number count estimator	flux estimator	theoretical value
d (10^{-2})	1.515 ± 0.006	1.542 ± 0.010	1.5

Table 2.1: Mean dipole amplitudes from 1000 simulations with statistical variance, the number count of the simulated sources behaved like $n(> S) \propto S^{-x}$ with $x = 1$ and the spectral index of the sources was $\alpha = 0.75$. Each simulation was full sky with 10^6 sources, the implemented observer velocity was $v = 1200\ \frac{\mathrm{km}}{\mathrm{s}}$ towards RA $= 180°$ and dec $= 0°$.

resulting amplitudes differ only very little and agree within their two-sigma boundaries with each other. One sees a little bit higher error for the flux estimator, which can be explained in the following way: Due to the fact that the sources are weighted with their flux values, some become more important in the estimation than others. This increases the shot noise of the estimator, since the number of higher weighted sources is comparably small. Hence, the shot noise amplitude bias will be a little bit increased and can explain the small difference in amplitude for both estimators.

This supports our initial statement that the flux estimator is less stable and therefore one should prefer to use a pure number count estimator. Another point is, that the flux estimator depends crucially on the power law behaviour of the number counts along the whole used flux spectrum, while the linear number estimator only assumes such a power law near the lower flux limit. Nevertheless, we acknowledge that both estimators result in the same amplitude expectation for the given assumptions and the proposed correction factor of 1.4 was an error.

Chapter 3

Masking and Calibration effects

> *Insufficient facts always invite danger.*
> — Mr. Spock, Star Trek: Space Seed

3.1 Masking

In section 2.1 the dipole amplitude measured by linear estimators was discussed in great detail. We found a bias, due to shot noise, as well as one due to masking. The second one was corrected for by simulated maps. The resulting amplitudes were compared to simulations, which assumed the CMB dipole as basis for the observer's velocity. In this way a discrepancy between the radio maps and the expected kinetic contribution was found.

The dipole direction on the other hand was assumed to be unbiased, as long as the masked map was point symmetric w.r.t. the observer. This assumption was first made in the work of Ellis & Baldwin (1984) and explicitly used in later studies, e.g. by Singal (2011). The basic principle is that the monopole will not appear in the linear estimation, as long as the mask is symmetric, since the monopole contribution due to masking will cancel then. Implicitly the same assumption is used, when masked areas are filled with isotropically distributed simulated sources, for correcting the monopole bias for incomplete skies [i.e. Crawford (2009) and Gibelyou & Huterer (2012)]. In fact this assumption is over-simplifying the problem, since the radio sky does also have a dipole modulation, which can interact with the mask. In this section we study, whether the dipole direction measured by linear estimators with a symmetric mask is unbiased or not.

One expects the biggest possible bias to emerge, when the mask is not symmetric with respect to the dipole modulation. We created simulated radio maps and used the linear estimator to measure the dipole direction. In this way we can compare, whether the measured direction is in agreement with the true simulated distribution. In order to reduce shot noise contamination, a rather high peculiar velocity ($v = 1200\frac{\mathrm{km}}{\mathrm{s}}$) was assumed and we simulated the sky with one million sources. We masked areas in two different ways. The first type of mask is called "caps", because the areas at the polar caps were masked and only sources between the declination values of 40° and $-40°$ were included in the measurement. Exactly inverted is the mask type "ring", where only sources outside those declinations will be taken into account.

mask type	$\mathrm{dec}_d^{\mathrm{sim}}$	measured $d \times 10^2$	measured dec_d
caps	$-40°$	1.565 ± 0.017	$-14.95° \pm 0.44°$
ring	$-40°$	2.016 ± 0.026	$-74.60° \pm 0.38°$
caps	$-10°$	1.917 ± 0.024	$-3.21° \pm 0.38°$
ring	$-10°$	0.915 ± 0.018	$-35.84° \pm 1.30°$

Table 3.1: Linear estimator measurements for 100 simulated maps containing 10^6 sources (for the full sky) and implemented observer velocity of $v = 1200\frac{\mathrm{km}}{\mathrm{s}}$ towards RA = 180° and $\mathrm{dec}_d^{\mathrm{sim}}$ (see table). Masking sources within $-40° < \mathrm{dec} < +40°$ for the ring type mask and with either $\mathrm{dec} > 40°$ or $\mathrm{dec} < -40°$ for the caps type mask.

In table 3.1 the results of our simulations can be seen. The changing dipole amplitude values were expected and for observations using radio surveys these amplitudes are therefore modified by a masking factor [see e.g. Rubart & Schwarz (2013)]. In all simulated cases we see a directional bias significantly above the estimated variances of the simulations. For the caps mask, the bias goes towards the celestial equator and for the ring mask type towards the celestial poles (in this case, the celestial South Pole). Due to symmetry considerations the caps mask in general will have an effect pointing towards the equator and the ring mask away from the equator, independent of the sign of the declination values.

For the simulated cases above we can calculate the direction bias analytically. Therefore we assume w.l.o.g. N sources on the whole sky and a dipole with right ascension of $RA = 0°$. The dipole amplitude d and the dipole declination dec_d will not be fixed. For convenience we will switch the coordinate system into spherical coordinates, meaning we change all declination angles into $\vartheta = 90° - \mathrm{dec}$ and just rename the right ascension $\mathrm{RA} = \varphi$ (i.e. $\vartheta_d = 90° - \mathrm{dec}_d$ and $\varphi_d = 0°$). We calculate the expectation value of the linear estimator with a mask that removes sources within the polar caps (up to an angular distance to the poles of α),

$$\langle \vec{R}_{\mathrm{3D}} \rangle = \frac{N}{4\pi} \int_{|\cos\vartheta| < |\cos\alpha|} \mathrm{d}\Omega \, (1 + \hat{r} \cdot \vec{d}) \, \hat{r}. \tag{3.1}$$

We define $\beta = \cos\alpha$ and the integral becomes:

$$\frac{N}{4\pi} \int_0^{2\pi} \mathrm{d}\varphi \int_{-\beta}^{\beta} \mathrm{d}\cos\vartheta \, \left[1 + \begin{pmatrix} \cos\varphi \sin\vartheta \\ \sin\varphi \sin\vartheta \\ \cos\vartheta \end{pmatrix} \cdot d \begin{pmatrix} \sin\vartheta_d \\ 0 \\ \cos\vartheta_d \end{pmatrix} \right] \hat{r}.$$

Executing the scalar product, the integrand gives

$$\curvearrowright [1 + d\cos\varphi \sin\vartheta \sin\vartheta_d + d\cos\vartheta \cos\vartheta_d] \begin{pmatrix} \cos\varphi \sin\vartheta \\ \sin\varphi \sin\vartheta \\ \cos\vartheta \end{pmatrix} .$$

The y component of $\langle \vec{R}_{\mathrm{3D}} \rangle$ vanishes, since the corresponding terms in the integrand are proportional to $\sin\varphi$ or $\sin\varphi\cos\varphi$ and will therefore result in 0 after the integration over $\mathrm{d}\varphi$. Now we evaluate the z component. Here the terms $\cos\vartheta + d\cos\vartheta\cos\varphi\sin\vartheta\sin\vartheta_d$ vanish after $\cos\vartheta$ and φ integration respectively. Hence, we are left with

$$\langle \vec{R}_{\mathrm{3D}} \rangle_z = \frac{N}{4\pi} \int_0^{2\pi} \mathrm{d}\varphi \int_{-\beta}^{\beta} \mathrm{d}\cos\vartheta (d\cos^2\vartheta \cos\vartheta_d) \ .$$

After resubstituting β, this integral provides the expectation value

$$\langle \vec{R}_{\mathrm{3D}} \rangle_z = \frac{N}{3} d \cos\vartheta_d \cos^3\alpha \ . \tag{3.2}$$

Here we see that the masking limit $\cos\alpha$ does have an effect on the z component of the estimator. In order to understand, whether the effect propagates to the direction estimation, we also have to evaluate the x component of the integral. Here the only nonvanishing term in the integrand leads to

$$\langle\vec{R}_{3\mathrm{D}}\rangle_x = \frac{N}{4\pi}\int_0^{2\pi}\mathrm{d}\varphi\int_{-\beta}^{\beta}\mathrm{d}\cos\vartheta(d\cos^2\varphi\sin^2\vartheta\sin\vartheta_d)\ ,$$

which can be solved, utilizing the relation $\sin^2\vartheta = 1-\cos^2\vartheta$ and again changing β back to $\cos\alpha$, leading to:

$$\langle\vec{R}_{3\mathrm{D}}\rangle_x = \frac{N}{2}d\sin\vartheta_d\left[\cos\alpha - \frac{1}{3}\cos^3\alpha\right]\ . \tag{3.3}$$

The direction estimation ϑ_e can be obtained by $\tan\vartheta_e = \frac{\langle\vec{R}_{3\mathrm{D}}\rangle_x}{\langle\vec{R}_{3\mathrm{D}}\rangle_z}$, which leads to

$$\tan\vartheta_e = \frac{\langle\vec{R}_{3\mathrm{D}}\rangle_x}{\langle\vec{R}_{3\mathrm{D}}\rangle_z} = \frac{N/2\ d\sin\vartheta_d\left[\cos\alpha-\frac{1}{3}\cos^3\alpha\right]}{N/3\ d\cos\vartheta_d\cos^3\alpha}\ ,$$

and this simplifies into

$$\tan\vartheta_e = \tan\vartheta_d\frac{\left[\frac{3}{2}-\frac{1}{2}\cos^2\alpha\right]}{\cos^2\alpha}\ . \tag{3.4}$$

When applying no mask, meaning $\alpha = 0 \rightarrow \cos\alpha = 1$, the direction estimation becomes unbiased, since the last factor in equation (3.4) will be unity. Before this result is compared to the simulation, we also consider the case of a mask excluding sources within a ring of $|\cos\vartheta| < |\cos\alpha|$. For this we can utilize the previous calculation, since we are considering the exactly inverted case. Hence, the expectation of each component will be the value for the whole sky, with the values derived above subtracted, for sources within the ring, so

$$\langle\vec{R}_{3\mathrm{D}}\rangle_z = \frac{N}{3}d\ \cos\vartheta_d\left[1-\cos^3\alpha\right]$$

and

$$\langle\vec{R}_{3\mathrm{D}}\rangle_x = \frac{N}{3}d\ \sin\vartheta_d\left[1-\frac{3}{2}\left(\cos\alpha-\frac{1}{3}\cos^3\alpha\right)\right]\ .$$

From this we obtain

$$\tan\vartheta_e = \frac{\langle\vec{R}_{3\mathrm{D}}\rangle_x}{\langle\vec{R}_{3\mathrm{D}}\rangle_z} = \tan\vartheta_d\frac{1-\frac{3}{2}\cos\alpha+\frac{1}{2}\cos^3\alpha}{1-\cos^3\alpha}\ . \tag{3.5}$$

This time the case of no applied mask corresponds to $\alpha = 90° \rightarrow \cos\alpha = 0$ and the estimator becomes unbiased again. For both cases we obtain a different bias, but the behaviour is the same in principle. The tangent of the declination will be multiplied by a factor. For the case of a caps type mask, the behaviour will be described by the factor $B_c = \left[\frac{3}{2} - \frac{1}{2}\cos^2\alpha\right] / \cos^2\alpha$. When we mask sources inside a ring, the bias factor becomes $B_r = \left[1 - \frac{3}{2}\cos\alpha + \frac{1}{2}\cos^3\alpha\right] / \left[1 - \cos^3\alpha\right]$.

mask type	$\lvert\tan\vartheta_d{}^{\text{sim}}\rvert$	$\lvert\tan\vartheta_d{}^{\text{est}}\rvert$	$\frac{\lvert\tan\vartheta_d{}^{\text{est}}\rvert}{\lvert\tan\vartheta_d{}^{\text{sim}}\rvert}$	$B_{c/r}$
caps	1.19	3.75 ± 0.12	3.14 ± 0.11	3.13
ring	1.19	0.28 ± 0.01	0.23 ± 0.01	0.23
caps	5.67	17.84 ± 2.12	3.15 ± 0.38	3.13
ring	5.67	1.38 ± 0.07	0.24 ± 0.01	0.23

Table 3.2: Comparison of theoretical $\frac{\lvert\tan\vartheta_d{}^{\text{esti}}\rvert}{\lvert\tan\vartheta_d{}^{\text{sim}}\rvert}$ with simulated results from linear estimator measurements for 100 simulated maps with 10^6 sources (for the full sky) and implemented observer velocity of $v = 1200\frac{\text{km}}{\text{s}}$ towards RA = 180° and $\tan_d^{\text{sim}}$ (see table). Masking sources within $-40° < \text{dec} < +40°$ for the ring type mask and with either $\text{dec} > 40°$ or $\text{dec} < -40°$ for the caps type mask.

In order to verify this derivation, we compared the calculated bias factors with the results from the simulations, shown in table 3.1. Therefore we needed to convert the declination values into spherical coordinates and apply a tangent function on those. Then we form the ratio of the simulated dipole and the measured one and compare this with the theoretical bias factor. The results can be seen in table 3.2. One can directly see that the bias factors from the simulations fit very well to the calculated ones within the estimated uncertainties. Hence, we understood this effect for both discussed cases and can conclude that masking a ring or masking areas outside a ring does have a significant effect on the dipole direction estimation in general.

The estimated dipole direction will be effectively pushed away from the masked areas. In both discussed cases the expectation value of the direction ϑ_e will be

$$\vartheta_e = \arctan\left(B\tan\vartheta_d\right) \ , \tag{3.6}$$

with B standing for the bias factor B_c or B_r, depending on the mask type. The total change in angle is small, when the distance between the masked areas and the dipole is big (meaning close to 90°), since arctan becomes very flat for those angles. So a dipole direction, which is far away from the masked region is not biased as much and would therefore be comparably stable.

The estimated dipole declination in section 2.1 is $\mathrm{dec} = -2°$. This is far away from the largest masking areas at $|\mathrm{dec}| > 40°$, which is just what we expect from the discussed bias effect. Note that in table 3.1 we see that a dipole at $\mathrm{dec} = -10°$ can be shifted towards $\mathrm{dec} = -3°$ due to the masking effect. Hence, we can estimate that our result may include a directional bias of similar magnitude.

For the case of a mask consisting of one ring, (excluding or including sources within) the bias can be corrected for, since it is now fully understood. Unfortunately the mask, used in real dipole estimation, is more complicated. Each mask consists of at least two masking rings (with different orientations), which in general even overlap. Those cases cannot be handled as trivially by deriving a general bias factor. Even writing down the corresponding integrals is not simple and we cannot make any simplifying assumptions about the dipole position anymore.

It is also not possible to simulate the bias in a straightforward way, since we cannot know the real dipole position. In order to perform a search for the real dipole position, given a certain mask and an estimated dipole position, we would need to simulate every possible dipole direction. Then we must evaluate, which one of those (or possibly even more than one) will result in a biased direction close to the measured one. Such a simulation would eliminate the biggest advantage of the simple linear estimator, namely that it is fast in terms of computational time.

In chapter 2.1 we discussed the masking bias in amplitude. We used simulated data in order to correct the final dipole estimation for this effect. With the results from above, we are able to give theoretical values for the bias coming from the masks, in the above described simple cases. The expectation of the linear estimator without any bias is $Nd/3$ and so we define the amplitude bias factor for the caps/ring mask by

$$B^a_{c/r} = \frac{\sqrt{< R_x >^2 + < R_y >^2 + < R_z >^2}}{Nd/3} \; . \tag{3.7}$$

Since the dipole is assumed to be at $RA = 0°$ here, the $< R_y >$ term vanishes and the x and z contributions can be taken from the above calculations. For the caps mask we obtain:

$$B_c^a = \sqrt{\frac{9}{4}\sin^2\vartheta_d\left[\cos\alpha - \frac{1}{3}\cos^3\alpha\right]^2 + \cos^2\vartheta_d\cos^6\alpha}\ , \tag{3.8}$$

and for the ring mask:

$$B_r^a = \sqrt{\sin^2\vartheta_d\left[1 - \frac{3}{2}\cos\alpha - \frac{1}{3}\cos^3\alpha\right]^2 + \cos^2\vartheta_d\left[1 - \cos^3\alpha\right]^2}\ . \tag{3.9}$$

Both factors will vanish for the case of no mask. This derivation is an analytic confirmation of the amplitude bias observed with linear estimators [e.g. Rubart & Schwarz (2013), Singal (2011)].

It is very interesting to notice, that the bias factor does not depend on the dipole amplitude or the number of sources used in the estimations. Therefore this effect will be present in all future estimation, no matter how many sources the catalogue will include.

Summarized, we found that the dipole direction estimated from a very simple linear estimator is of limited use, since it has a directional bias, which cannot easily be corrected for in the general case. The results of this chapter do not apply for more complicated linear estimators, like the ones utilizing spherical harmonics [e.g. Kothari et al. (2013)].

3.2 Calibration

Every measurement contains a measurement uncertainty. There is no real instrument to determine a physical value perfectly. Hence, every position and flux value given in a radio source catalogue (i.e. the NVSS) contains an uncertainty. In this section we want to investigate, what effect measurement errors will have on the dipole estimation. It is quite clear that an error in the direction of an individual source does not have a direct impact on the dipole. Directional errors must be correlated in order to affect our estimation. It is reasonable to assume that such an error would be on much smaller scales than the 180° we are investigating. Assume all positions are systematically biased by one degree. Then the resulting dipole estimation would also be biased by one degree. The current dipole position uncertainty due to shot noise is an order of magnitude higher. Hence, the effect of position measurement errors on the dipole estimation is small and we will focus on errors in flux, during this work. A total measurement offset for all sources (i.e. $S + 5\mathrm{mJy}$) will not have any effect on the dipole search, since the applied estimator is searching for a relative increase in source counts in a given radio survey.

The sensitivity of a radio telescope does depend on the declination of the observed source. This is due to the fact that it is harder to observe sources near the horizon of the telescope's field of view than around the zenith. Due to the Earth's rotation a large part of the sky will be visible high above the horizon at some point during the day. For areas near the celestial poles this is not the case, as long as the telescope is not close to the North or South Pole. Depending on where on the spherical earth a telescope is located some areas of the sky will never be visible and some will only be visible relatively near to the horizon. Hence, a radio telescope will not have a uniform sensitivity across the whole sky.

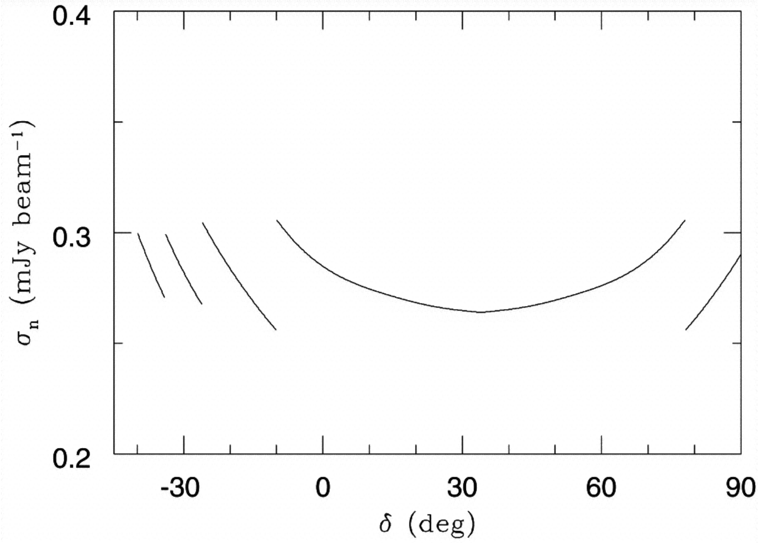

Figure 3.1: Expected rms noise level for the NVSS on snapshot image centres [source: Condon et al. (1998)].

In figure 3.1 we see the estimated noise level of the VLA for the observations of the NVSS survey. The curve is not continuous since the VLA did not observe with the same configuration and integration time for all declinations. Sources with declination far away from dec = 30° were observed for longer times in order to keep the noise at a near to constant level for the whole survey. The interesting question for this work is, whether such a noise distribution has any impact on the dipole estimation. For investigating this question we used computer simulated radio maps, which included measurement uncertainties in flux.

We focus on Gaussian random errors in the flux measurement of individual sources with variance σS_t, where S_t denotes the true (simulated) flux of a source. The measured flux will then be

$$S_m = S_t + \sigma S_t r \ , \tag{3.10}$$

where r is a random variable drawn from a standard normal distribution. We will consider two distinct cases for the variance. In the first one we consider a constant variance over the whole sky i.e. $\sigma = \sigma_0$. In the second case we try to mimic the general noise behaviour shown in figure (3.1), by letting the variance depend on the declination. The lowest variance is found at declination δ_* and from there on continuously increases in both directions symmetrically. We found that the form of the variance of the NVSS noise is quite well described by $\sigma = \sigma_0 / \cos(\delta - \delta_*)$. We restrict our simulation to declinations fulfilling $|\delta - \delta_*| < 70°$, in order to keep the maximal variance below three times the minimal variance.

We expect the influence of such calibration errors to depend on the number count form, which is approximated by $N(>S) \propto S^{-x}$ for surveys like the NVSS near its lower flux values. We tested different values of the slope x in order to see how the number counts may influence the measurement error in these cases. In the end we may find a bias in the dipole amplitude and/or direction estimations and therefore we studied both. We did this for a constant as well as for declination-dependent σ. In the first case we did not see any dependence on x and therefore we will only show the result of $x = 1$ for the isotropic case.

In figure 3.2 we see the dependence of the dipole amplitude estimation on the calibration error. Shown in this graph is the relative error of the estimated dipole amplitude in percent. For comparison, we also plotted

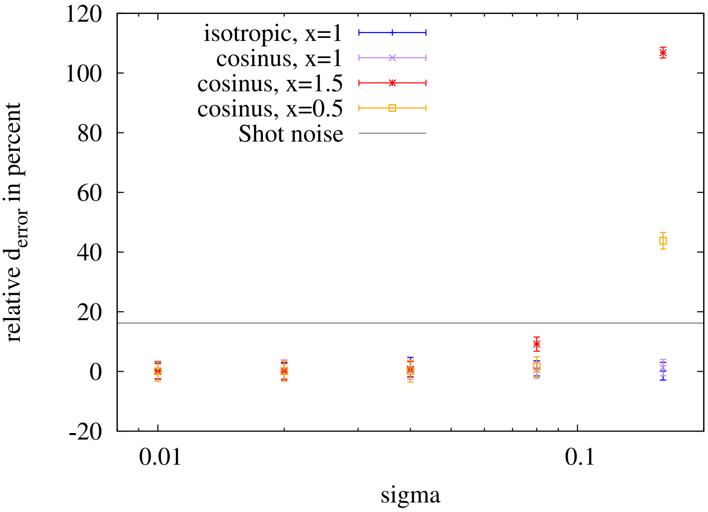

Figure 3.2: Relative dipole amplitude error versus σ_0 for different values of x and for the case of constant and declination-dependent measurement error (with $\delta_* = 30°$). Each point represents the mean after 100 simulations and the error bars show the statistical variance of those. The horizontal line denotes the error due to shot noise for a dipole estimate based on 10^7 sources [source: Schwarz et al. (2015)].

the expected shot noise contribution for the case of 10^7 sources. When the calibration error is below $\sigma_0 = 0.1$ we obtain an amplitude uncertainty, which is dominated by shot noise. We can conclude that such a small calibration effect will not have a significant impact on the dipole estimation. Larger calibration effects on the other hand could spoil the dipole estimation dramatically.

For higher values of σ_0 the error rises in two of the four shown cases. A constant value of σ (isotropic case) seems to have no biasing effect at all. This result we actually expected and it holds for all tests we performed, as long as the calibration effect was isotropic for the whole sky. The declination dependent cases start to show a trend towards increased dipole amplitude estimations for higher values of σ_0. This effect is strongest for

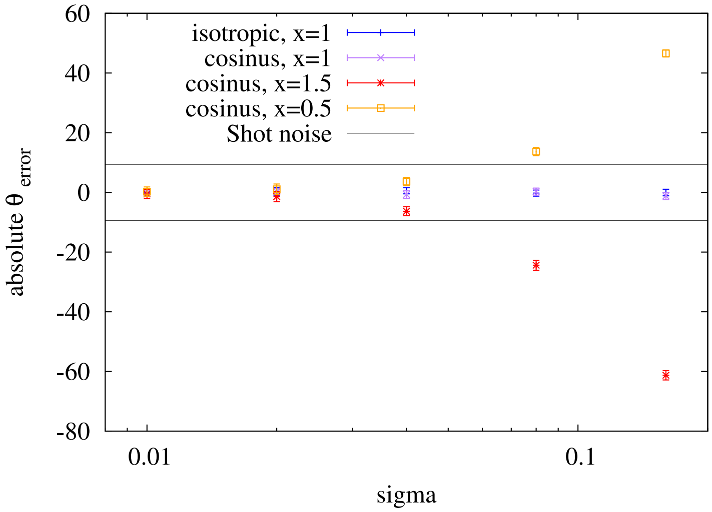

Figure 3.3: Absolute dipole direction error versus σ_0 for different values of x and for the case of constant and declination-dependent measurement error (with $\delta_* = 30°$). Each point represents the mean after 100 simulations and the shown error bars come from statistical variance of those. The horizontal lines denote the error due to shot noise for a dipole estimate based on 10^7 sources [source: Schwarz et al. (2015)].

$x > 1$, so for a steeper number count. It is very interesting that in the case of $x = 1$ the amplitude does not increase, even if the calibration does depend on the declination. This finding will be discussed later in more detail.

In figure 3.3 the absolute offset angle after 100 simulations including different calibration uncertainties to the case without any calibration error is shown. The expected shot noise uncertainty for a survey with 10^7 sources can be seen as horizontal lines. For all cases with $\sigma_0 \leq 0.04$ we see that the change in dipole direction due to calibration problems is below the shot noise uncertainty. For $x = 1.5$ and $x = 0.5$ in the declination-dependent cases we see a bias in the direction estimation. This bias is becoming dominant with respect to the shot noise, when σ_0 is increased further.

The direction of this bias is opposite for the two discussed cases. We will give a qualitative reason for this after we discussed the $x = 1$ case.

Just like for the amplitude before we see here that the cases with $x = 1$ do not show any dependence on σ_0. For the isotropic calibration uncertainty this is not surprising, but it is remarkable that also for strongly declination-dependent measurement errors, the dipole estimation seems not to be influenced. We actually found that $x = 1$ is a kind of 'sweet spot', in which the dipole effect is independent of the flux measurement accuracy. In the following part of this section we will prove this statement analytically.

The linear estimators used in this study utilize the flux of a source from a survey in only one way. If the measured flux is above the applied flux limit S of an estimator, the corresponding source is taken into account. So an inaccurate flux measurement can only have two effects: (a) a source is taken into account although its true flux would have been too low or (b) a source is ignored, even so its true flux would have been high enough. So some sources drop out from the estimation and others are added. Hence, there is a new lowest flux limit called S_-, with the condition $S_- + 2\sigma S_- = S \Leftrightarrow S_- = \frac{S}{1+2\sigma}$. Actually there is no fixed limit anymore, but all sources below this S_- will to 95% certainty not be taken into account. The amount of potential 'extra' sources can be evaluated by the integral

$$\alpha \int_{\frac{S}{1+2\sigma}}^{S} \mathrm{d}S \; S^{-x-1} \; , \tag{3.11}$$

where the number of sources per flux is $\frac{\mathrm{d}N}{\mathrm{d}S} = \alpha S^{-x-1}$ with some constant α, so that $N(> S) \propto S^{-x}$. Of course not all of these sources will be used in the dipole estimation, but for the sake of determining the sweet spot at $x = 1$ it is sufficient to look at the amount of potentially extra sources. The result of (3.11) is

$$\frac{\alpha}{x} \left(S^{-x} - \left(\frac{S}{1+2\sigma} \right)^{-x} \right) \; . \tag{3.12}$$

In the same way we can calculate the number of potential sources that were ignored in the dipole estimation, although the real flux value was high enough. Those will be between S and $S_+ - 2\sigma S_+ = S \Leftrightarrow S_+ = \frac{S}{1-2\sigma}$

and hence we need to integrate:

$$\alpha \int_{S}^{\frac{S}{1-2\sigma}} \mathrm{d}S\ S^{-x-1} = \frac{\alpha}{x}\left(\left(\frac{S}{1-2\sigma}\right)^{-x} - S^{-x}\right) . \tag{3.13}$$

Both effects work in opposite directions, one adding and one subtracting sources. Hence, they can cancel each other, when the magnitudes are the same. Due to the simulation we strongly suspect that this happens for $x = 1$ and so we test this hypothesis now:

$$\begin{aligned} \frac{\alpha}{x}\left(\left(\frac{S}{1-2\sigma}\right)^{-x} - S^{-x}\right) &= \frac{\alpha}{x}\left(S^{-x} - \left(\frac{S}{1+2\sigma}\right)^{-x}\right) \\ &\Leftrightarrow\ 2 - (1+2\sigma)^{x} - (1-2\sigma)^{x} = 0, \end{aligned} \tag{3.14}$$

which is true for $x = 1$. So we can conclude that for $x = 1$ a Gaussian measurement error for the flux values does not influence the dipole estimation at all. This actually also holds true for e.g. higher multipole moments or two-point correlations, not only for the dipole estimation. For the NVSS survey, $x = 1.10 \pm 0.02$ for flux values of 25 mJy to 200 mJy (Rubart & Schwarz 2013) and therefore we are close to the discussed 'sweet spot' and expect no dominant calibration effect.

Now we can also understand that the absolute direction offset for $x = 1.5$ and $x = 0.5$ in figure (3.3) goes into opposite directions. For $x = 1.5$ there are more sources coming additionally into the estimation in areas with high σ and so we get a dipole towards regions with higher uncertainties. In the case of $x = 0.5$ we will lose more sources in areas with high σ and so the resulting dipole error points away from the areas with higher variance. Hence, both cases must show a different directional error and the case of $x = 1$ lies in the middle, with no biasing effect at all.

3.3 Publication arXiv:1501.03820

In 2014 a conference in Giardini Naxos, Italy, was held with the aim to produce an updated version of the SKA science book, named Advancing Astrophysics with the Square Kilometre Array. This book will be published online by Proceedings of Science in 2015. The following publication is part of this updated description of possible scientific projects, utilizing SKA.

Using large area ($\approx 3\pi$) radio sky surveys produced by SKA will enable a number of important cosmological tests. The cosmic radio dipole can be measured with such surveys at a high precision and it will be possible to notice any directional variation w.r.t. the CMB dipole on a degree scale.

With the angular two-point correlation function it will be possible to test the power spectrum at low multipoles and thereby probe the large scale structure of the universe. It will be interesting to see, whether the power spectrum of number counts with such surveys is scale invariant at superhorizon scales, as expected by the current cosmological model. Finally, also the Copernican Principle will be tested with such surveys, combined with SNIa distance measurements.

The main contribution of Matthias Rubart to this publication was explained in detail in the previous sections. His work is the basis for the second section (i.e. cosmic radio dipole) of the following publication.

This contribution has been reviewed and accepted for publication. The science case layed out in this work became a Tier.1 science goal of SKA (Braun et al. 2014).

PROCEEDINGS OF SCIENCE

Testing foundations of modern cosmology with SKA all-sky surveys

---

Dominik J. Schwarz*,[1] **David Bacon,**[2] **Song Chen,**[1] **Chris Clarkson,**[3] **Dragan Huterer,**[4] **Martin Kunz,**[5,6] **Roy Maartens,**[7,2] **Alvise Raccanelli,**[8,9] **Matthias Rubart,**[1] **Jean-Luc Starck**[10]

[1] *Fakultät für Physik, Universität Bielefeld, 33501 Bielefeld, Germany;* [2] *Institute of Cosmology & Gravitation, University of Portsmouth, Portsmouth PO1 3FX, United Kingdom;* [3] *Centre for Astrophysics, Cosmology & Gravitation and Department of Mathematics & Applied Mathematics, University of Cape Town, Cape Town 7701, South Africa;* [4] *Department of Physics, University of Michigan, Ann Arbor, MI 48109-1040, USA;* [5] *Université de Genève, Département de Physique Théorique and CAP, CH-1211 Genève 4, Switzerland;* [6] *African Institute for Mathematical Sciences, Cape Town 7945, South Africa;* [7] *Physics Department, University of the Western Cape, Cape Town 7535, South Africa;* [8] *Jet Propulsion Laboratory, California Institute of Technology, Pasadena CA 91109, USA;* [9] *California Institute of Technology, Pasadena CA 91125, USA;* [10] *Laboratoire AIM, UMR CEA-CNRS-Paris, Irfu, SAp, CEA Saclay, F-91191 Gif-sur-Yvette CEDEX, France*

E-mail: `dschwarz@physik.uni-bielefeld.de`

Continuum and HI surveys with the Square Kilometre Array (SKA) will allow us to probe some of the most fundamental assumptions of modern cosmology, including the Cosmological Principle. SKA all-sky surveys will map an enormous slice of space-time and reveal cosmology at super-horizon scales and redshifts of order unity. We illustrate the potential of these surveys and discuss the prospects to measure the cosmic radio dipole at high fidelity. We outline several potentially transformational tests of cosmology to be carried out by means of SKA all-sky surveys.

Advancing Astrophysics with the Square Kilometre Array
June 8-13, 2014
Giardini Naxos, Italy

---

*Speaker.

1. Introduction

The Square Kilometre Array (SKA) will allow us to test fundamental assumptions of modern cosmology at redshifts of order unity and at an accuracy level matching and complementing the high fidelity observations of the cosmic microwave background (CMB).

The Cosmological Principle states that the Universe is spatially isotropic and homogeneous. Strictly, this holds on sufficiently large scales and needs to be interpreted in a statistical sense. Historically, it provided a very powerful motivation to single out the Friedmann-Lemaître models despite a lack of knowledge regarding the initial conditions of the Universe. Cosmological inflation, proposed in the 1980s, allowed the universe to start from a reasonably small patch of almost homogeneous and isotropic space. According to the idea of cosmological inflation, suddenly at least one small patch is inflated to contain today's observable Universe. In the course of inflation, any previously existing anisotropy or inhomogeneity is exponentially diluted. However, unavoidable quantum fluctuations are squeezed by the rapid expansion during inflation and become the seeds for large scale structure formation in the more recent history of the Universe. This results in a statistically isotropic and homogeneous Universe (at least locally).

The observed high degree of isotropy of CMB radiation enables us to define a CMB frame by measuring the CMB temperature monopole, $T_0 = 2.2755 \pm 0.0006\,\mathrm{K}$ and dipole, $T_1 = 3.355 \pm 0.008\,\mathrm{mK}$ towards $(l,b) = (263.99^\circ \pm 0.14^\circ, 48.26^\circ \pm 0.03^\circ)$ [1]. The concept of a spatially homogeneous Universe allows us to speak about a cosmic time or an age of the Universe. By measuring the CMB temperature T_0 and the present expansion rate of the Universe H_0 we can anchor the thermal history of the Universe to its expansion history. Testing the assumption of isotropy is much simpler than testing homogeneity [2, 3].

Radio surveys played an important role to establish that the Universe extends to redshifts beyond unity and that it is almost isotropic (see e.g. [4]). Today, observations of the CMB confirm the predictions of cosmological inflation impressively [5, 6], especially by means of the CMB angular temperature and polarization power spectra. However, it is unknown for how long (or how many e-foldings) inflation took place. In order to explain the observed spatial flatness of the Universe, about 50 to 60 e-foldings could be enough, but in many models it took much longer, i.e. the domain in which the statistical cosmological principle applies is expected to be much larger than the observable Universe. The quest to determine the duration of inflation, as well as the related question of the topology of the Universe, can only be answered by observing the biggest scales.

Interestingly enough, the CMB exhibits unexpected features at the largest angular scales, among them a lack of angular correlation, alignments between the dipole, quadrupole and octupole, hemispherical asymmetry, a dipolar power modulation, and parity asymmetries [7, 8, 9]. Understanding the statistical significance of these anomalies is a hot topic [10, 11, 12] since lack of statistical isotropy or Gaussianity could rule out the standard cosmological model. As the precision of these CMB measurements is limited by our understanding of the foregrounds and observational uncertainties are already much smaller than the cosmic variance at those scales, it is very hard to identify the cause of these anomalies without an independent probe at the same scales.

SKA will probe an enormous number of independent modes when studying the large-scale structure of the Universe and will measure superhorizon sized modes at redshifts of order unity (better than any existing or planned infrared, optical, or X-ray campaign). This will enable us to probe scales that have not been in causal contact since the first horizon crossing during inflation and that contain information that was frozen in during cosmological inflation. In contrast to the CMB, the radio sky provides a probe of those largest scales at a redshift of order unity (2D for continuum surveys and 3D for HI surveys).

SKA would enable several tests of the fundamental cosmological principles. For example, the rest frames of the CMB and large scale structure (LSS) may not coincide due to novel superhorizon physics — for example, presence of isocurvature modes [13]. SKA's width and depth will enable a measurement the kinematic dipole with respect to the LSS reference frame via the relativistic aberration and Doppler shift ("bunching up" of SKA sources in the direction of the dipole). This, when combined with the CMB's own measurement of the kinematic dipole would, for the first time, enable the test of whether the two reference frames — that of the CMB and the LSS — are one and the same, as demanded by the Cosmological Principle.

Here we describe how to use all-sky (3π) SKA continuum surveys to test statistical isotropy and to measure the cosmic dipole and other low-ℓ multipole moments. These issues are tightly connected to tests of non-Gaussianity and the topology of the Universe, the former aspect is described in [14]. All-sky SKA HI threshold surveys will additionally allow us to test the homogeneity of the Universe at superhorizon scales – a test that has never before been performed. Statistical homogeneity and isotropy are assumed to hold true in other cosmology-related contributions to this book [15, 16]. Tests of statistical isotropy and homogeneity will also allow (and force) us to dig deep into the systematics of the SKA surveys and thus help to put all cosmological and non-cosmological results of SKA surveys on firmer grounds.

The conceptually simplest probe of cosmology is differential number counts [17]. If no redshift information is available, one can count the number of (extragalactic) radio sources per solid angle and flux density. Besides flux calibration issues, the cosmological information contained in differential number counts is limited by the diversity of radio sources and their luminosity and density evolution. Radio sources fall into two principal classes, active galactic nuclei (AGN) and star forming galaxies (SFG). The exquisite angular resolution of SKA surveys will allow us to resolve most of the AGNs and thus to obtain an extra handle based on morphology. Another simple possibility to overcome the restrictions from evolution is to study the directional fluctuations of differential number counts [18], as we do not expect that the properties of radio sources would single out preferred directions in the Universe. Fluctuations can be studied in harmonic or in real space, utilizing complementary analysis techniques (note that harmonic space and real space analysis are equivalent for full-sky data, but not for masked sky surveys).

2. Cosmic radio dipole (Early Science, SKA1, Full SKA)

The CMB dipole is generally assumed to be due to our peculiar motion and thus defines a cosmic reference frame. However, the observation of the dipole in the microwave sky is not enough to tell the difference between a motion-induced CMB dipole and dipole contributions from other physical phenomena (e.g. the model in [13]).

Due to the effects of aberration and Doppler shift, the kinetic dipole must also be present in radio observations [19]. Besides the kinetic dipole, we also expect contributions from the large-scale structure and from Poisson noise. Such a radio dipole has been looked for in radio source

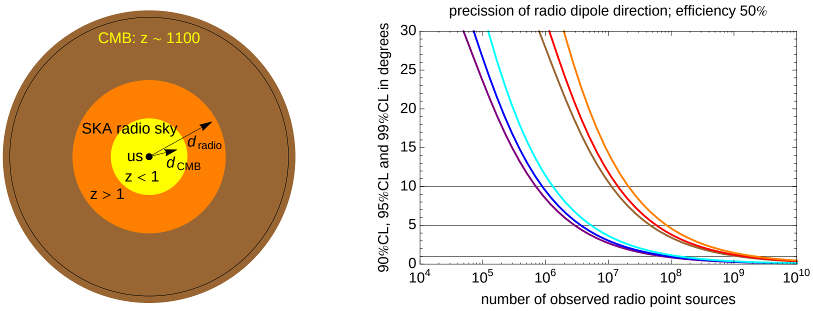

Figure 1: *Left:* All-sky (3π) SKA surveys (yellow and orange) will measure the cosmic radio dipole of differential source counts. Selecting AGNs will result in a sample with median redshift $z > 1$ (orange) and thus allow us to measure the peculiar velocity of the solar system with respect to the large scale structure on superhorizon scales. These measurements will be compared to the CMB dipole and thus test for the existence of a bulk flow of our Hubble volume compared to the CMB rest frame. *Right:* Angular accuracy at 90, 95 and 99 % C.L. of the measurement of the cosmic radio dipole as a function of observed point sources. The blue set of curves assumes $d_{\text{radio}} = 4d_{\text{cmb}}$, the red set assumes $d_{\text{radio}} = d_{\text{cmb}}$. It is assumed that only 50% of all detected radio sources survive all quality cuts (e.g. masking fields that contain very bright sources). Combined with Table 1 we find that SKA Early Science allows detection of a possible deviation from the CMB expectation at high significance. SKA1 will constrain the cosmic radio dipole direction with an accuracy better than 5 degrees, the full SKA within a degree (at 99% C.L.).

catalogues, such as NVSS [20, 21, 22] and WENSS [22] and was found within large error bars. While the direction of the observed radio dipole is consistent with the CMB dipole direction, its amplitude exceeds the theoretical expectations by a factor of a few. SKA will enable us to measure the radio dipole with high accuracy and to extract other low-ℓ multipole moments. Recently, the Planck mission reported a first detection of the effects of aberration and Doppler shift at high multipole moments [23]. However, this observation is less precise than the reported measurements of the radio dipole and allows for a primordial contribution to the CMB dipole of comparable size.

The SKA will allow us to compare $\vec{d}_{\text{radio}}$ to $\vec{d}_{\text{cmb}}$, since SKA will test a super-horizon sized volume. Any statistically significant deviation will be exciting, while finding a match would put the concordance model on firmer grounds.

SKA continuum surveys at low frequencies ($< 1\,\text{GHz}$) should be ideal to probe the cosmic radio dipole already in the Early Science phase for two reasons. First, it is not necessary to cover the full area of the 3π surveys, since a sparse sampling spread out over all of the accessible sky should be sufficient for a first estimate. And second, a focus on low frequencies and bright sources will pick primarily AGNs which have a much higher mean redshift than the SFG.

Figure 1 illustrates the accuracy that we can hope to achieve for a measurement of the radio dipole based on a linear estimator [24, 22]. Our estimates are based on differential number counts from surveys in small and deep fields and simulations [25]. Our expectations for all-sky continuum surveys are summarized in Table 1. We find that the cosmic radio dipole can be measured at high statistical significance, even taking realistic data cuts into account (e.g. masking the galaxy and very bright extragalactic sources, or morphology, spectral index or flux cuts).

A major concern might be the effect of flux calibration errors on the dipole estimation. This has

SKA 3π surveys (centr. frequency, ang. res.)	Early Science	SKA1	Full SKA
LOW (151 MHz, 10”)	1.0×10^8 (20 μJy)	2.4×10^8 (10 μJy)	2.2×10^9 (1 μJy)
MID/SUR B1 (610 MHz, 1”)	7.8×10^7 (10 μJy)	1.9×10^8 (5 μJy)	1.8×10^9 (0.5 μJy)
MID/SUR B2 (1.4 GHz, 0.5”)	3.8×10^7 (10 μJy)	9.7×10^7 (5 μJy)	1.2×10^9 (0.5 μJy)

Table 1: Expected total number of radio sources (10 σ) in various frequency bands and survey instruments, assuming the SKA baseline design and the cosmology and differential number counts as simulated in [25]. In order to match observations at 1.4 GHz, the number of SFG has been multiplied by a factor of 2.5 compared to the simulations for all frequency bands. The numbers in brackets denote the assumed rms noise levels.

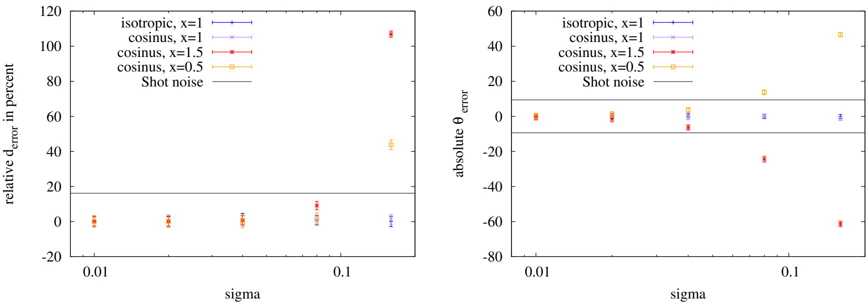

Figure 2: *Left:* Accuracy (in per cent) of the measurement of the dipole amplitude as function of fractional error on flux density calibration on individual point sources. All points are based on 100 simulations. *Right:* Accuracy (in degrees) of the measurement of the dipole direction. The horizontal lines denote the error due to shot noise for a dipole estimate based on 10^7 sources (SKA Early Science).

been studied by means of simulations. The results of this study are shown in figure 2. We assume Gaussian flux density errors with variance $\sigma(\delta)S$, where S denotes the expected flux density of a particular source. We consider the isotropic case in which $\sigma(\delta) = \sigma$ is isotropic and a declination dependent situation with $\sigma(\delta) = \sigma/\cos(\delta - \delta_*)$, δ_* being fixed by the latitude of the SKA site and $|\delta - \delta_*| < 70$ deg. For two cases we find negligible influence of callibration errors: If the flux calibration error is completely isotropic or if the slope x of the number counts $[N(> S) \propto S^{-x}]$ is equal to one. It turns out that $x = 1$ is a special value, where calibration errors at the lower flux density limit have no influence on the dipole estimator. We conclude that direction dependent calibration effects must not exceed certain limits as shown figure 2.

Another significant contaminant of the kinetic radio dipole is the local structure dipole. We can turn a disadvantage of continuum surveys, namely that we observe several source populations, into an advantage as follows: The lower mean redshift of SFGs compared to AGNs allows us to change the mean depth of the survey by scanning different fluxes density limits and frequencies. This in fact allows for a tomographic survey of the radio dipole. For the example of a huge ($\sim$ 100 Mpc) local void this was studied recently [26]. Figure 3 illustrates this effect.

3. Large angular scales (SKA1 and full SKA)

It is not obvious that the isotropic distribution of light implies also the isotropy of space-

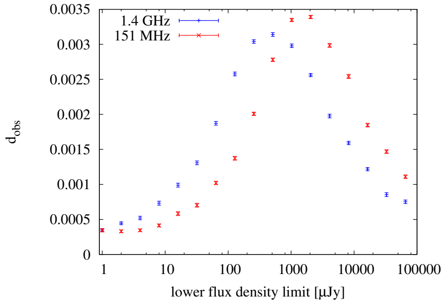

Figure 3: Amplitude of structure dipole due to a local void, affecting the measurements of the cosmic radio dipole as a function of lower flux density limit and for two wavebands centered on 151 MHz and 1.4 GHz (from [26]).

time itself. The vanishing of the quadrupole and octopole moments of the CMB would imply the isotropy of space-time along the world line of the observer [2]. While those low-ℓ multipoles are small compared to the monopole and dipole, they do not vanish exactly. We thus we can at best speak about an almost isotropic Universe. The radio sky offers another independent probe at $z > 1$ and at the largest angular scales.

Recent work has revealed the existence of CMB “anomalies" (for a review, see [27]). In brief, the angular correlation function in the WMAP and Planck temperature maps vanishes on scales larger than 60 degrees, contrary to theoretical expectation; moreover, the CMB quadrupole and octopole anisotropy patterns are aligned both mutually and with respect to the Solar System geometry. These anomalies have been widely studied and discussed, but their origin remains unexplained.

SKA will provide a deep and wide large-scale structure dataset that will enable separating the effects of the early and late universe on the observed CMB anisotropy. For example, the SKA data could be used to reconstruct the late-time contribution to the CMB anisotropy via the integrated Sachs-Wolfe effect, and thus provide information about the temporal evolution of the CMB anomalies.

3.1 Low-ℓ multipole moments

The analysis of low-ℓ multipoles from SKA continuum surveys can benefit from the methods developed for the study of the CMB. Missing sky area is always a problem for low-ℓ mode measurements. For CMB studies, many methods were proposed to deal with a mask of missing data for both power spectrum estimation and phase recovery. For the power spectrum, one the most used methods is MASTER [28]. It consists in first building a matrix which captures the coupling between the modes induced by the mask, and then inverting this matrix. In Figure 4 we plot the angular power spectrum of SKA galaxies for low-ℓ mulitpoles with error bars corresponding to a SKA1 continuum survey.

For phase recovery, or more generally for large scale map reconstruction, many methods have been proposed based on Wiener filtering, l_2 or l_1 norm regularization, constraint realizations or diffusion (see [11] and references therein). Based on these new methodological idea, Planck data were analyzed with a mask removing 27% of the sky [7, 12]. For a given observed sky area, the

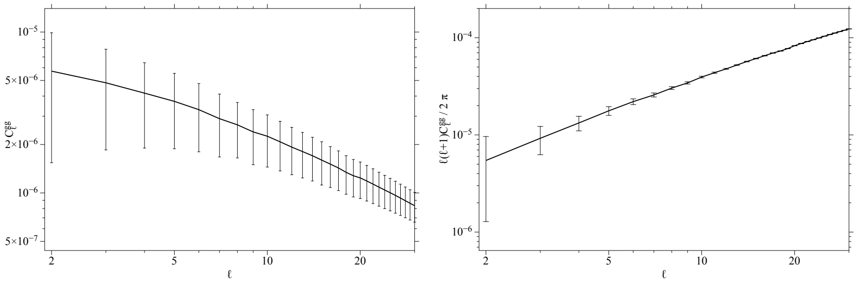

Figure 4: *Left:* Low-ℓ multipoles of the angular power spectrum as expected for a SKA1 continuum survey. *Right:* The corresponding band power. The errors contain shot noise and cosmic variance. The figures illustrate that statistically significant measurements of multipole moments can be expected.

shape of the mask will also be important. The importance of random sampling is also described in [29], and many small missing parts, randomly distributed, will always be much better for large scale studies than a compact big missing part.

As for the dipole, SKA will tremendously improve the precision and quality of low-ℓ multipole moments and thus allow us to probe statistical isotropy, scale invariance and gaussianity.

3.2 Angular 2-point correlation function

The angular two point correlation is a powerful tool to measure the projected large-scale structure distribution of the Universe. It allows us to probe certain fundamental assumptions like scale-invariance of the primordial perturbations, Gaussianity and the isotropy of the Universe (by comparing two-point correlations on sub-samples of the observed sky).

The two-point correlation at large angular scales contains many interesting aspects: Firstly, the matter fluctuations at large scales are in the linear regime. Secondly, general relativistic effects and cosmological evolution prefer large scales. AGNs are very good candidates to probe this, since they are isotropically distributed on the sky and most of them have a significant ($z > 1$) cosmological distance. In order to accurately investigate ultra-large scale correlations, the theoretical frame work of differential number counts based on general relativity will be needed [30, 31, 32, 33].

In contrast to galaxy redshift surveys within the local Universe ($z \ll 1$), all linear order relativistic corrections, which include the Doppler effect, lensing, and generalized Sachs-Wolfe contributions, are of relevance. The spread of luminosities of radio sources in continuum surveys washes out much of the clustering signal, and the general relativistic corrections are also suppressed. However, SKA HI surveys in which the source redshifts will be known will resolve these effects.

With the assistance of Lyman alpha data, one can model the luminosity function and evolution. With the SKA morphology data we expect to be able to identify different type of sources. This will allow us to study cross correlations between star forming galaxies and AGNs. We could also cross correlate with the CMB and different types of radio sources, which have different redshift distributions.

These aspects are treated in more detail in other contributions to this volume [14, 15, 16]. Let us just stress here the importance of re-establishing the almost scale-invariant power spectrum at superhorizon scales at $z \sim 1$, which will be possible by means of SKA all-sky surveys.

4. Copernican Principle and homogeneity (SKA1 & Full SKA)

The Copernican Principle is the assumption that we are not distinguished observers in the Universe. If we observe an isotropic cosmos, then distant observers should also see a similarly isotropic cosmos. This implies that the Universe satisfies the Cosmological Principle and is homogeneous on large scales. A violation of homogeneity in principle offers an alternative explanation to the acceleration of the Universe [34], but simple inhomogeneous models without dark energy are incompatible with current data [35]. However, radial homogeneity is only weakly constrained in ΛCDM [36]. Any deviations would imply a radical change to the standard model and scale-invariant initial conditions, making it a vital constraint on the standard model.

SKA HI intensity mapping on super-Hubble scales offers powerful new ways to test homogeneity. By comparing the radial and transverse scale of baryon acoustic oscillations we can test isotropy of the expansion rate around distant observers [2, 40, 3]. This places direct constraints on radial inhomogeneity about us, when redshift-space distortions, lensing and other large-scale GR effects are accounted for. Anisotropic expansion rates act on the sound horizon at decoupling so that by redshift z it has evolved into an ellipsoid with semi-axes

$$L_\parallel(z) = \frac{\delta z(z)}{(1+z)H_\parallel(z)}, \quad L_\perp(z) = d_A(z)\delta\theta(z), \tag{4.1}$$

given the observed radial and angular scales $\delta z(z), \delta\theta(z)$. $L_\parallel(z) = L_\perp(z)$ in a homogeneous universe. In an inhomogeneous universe $d_A(z)$ depends on the transverse Hubble rate along the line of sight, which will be different from the radial Hubble rate $H_\parallel(z)$, providing a test of homogeneity.

When combined with accurate distance data from SNIa, consistency relations can be used to check deviations from homogeneity in a completely model independent way [41]. In a homogeneous universe, irrespective of dark energy or theory of gravity, the Hubble rate $h(z) = H(z)/H_0$ and dimensionless comoving distance $D(z) = (1+z)H_0 d_A(z)$ satisfy ($' = d/dz$)

$$\mathscr{C}(z) = 1 + h^2\left(DD'' - D'^2\right) + hh'DD' = 0\ , \tag{4.2}$$

so that $\mathscr{C}(z) \neq 0$ implies violation of the Copernican Principle. We expect that SKA1 will be able to constrain $\mathscr{C}(z)$ to 0 ± 0.05 for $z < 1.5$, based on a naive error propagation from [39]. A more careful forecast has yet to be done. Direct constraints on radial inhomogeneity can be given combining with all available data sets which will significantly improve current constraints which are much weaker than those for isotropy [36].

Finally, the Copernican Principle allows for the possibility of a fractal universe, but this is not predicted by the concordance model – which predicts a fractal dimension of 3 on large scales – any deviations would imply new physics. It is therefore important to measure the fractal dimension of the distribution of radio sources at superhorizon scales. Such a test has been performed using the SDSS and the WiggleZ surveys, finding an approach to a three-dimensional distribution at $\sim 100\,$Mpc scales [37, 38]. A dramatic improvement will be possible based on SKA HI threshold surveys.

5. Summary

The Cosmological Principle provides the foundation for modern cosmology, and our understanding of the evolution of the Universe as well as all parameter constraints from the CMB, supernovae or large scale structure rely on this assumption. Testing the Cosmological Principle is thus of fundamental importance for cosmology generally as well as for the cosmological interpretation of the SKA data itself. As this chapter shows, SKA will be able to greatly increase our confidence that our cosmological framework makes sense (or lead to a scientific revolution if not).

We argue that SKA all-sky surveys will allow us to measure the cosmic radio dipole almost as precisely as the CMB dipole. SKA1 will constrain the cosmic radio dipole direction with an accuracy better than 5 degrees, the full SKA within a degree (at 99% C.L.). This measurement could finally firmly establish or refute the commonly adopted assumption that the CMB and the overall LSS frames agree, and will have impact on a variety of cosmological observations, from the local measurement of H_0 to the calibration of CMB experiments. A tomography of the cosmic radio dipole might reveal a detailed understanding of local LSS.

In addition, studying the large-angular scales in SKA continuum and HI surveys might help resolve the puzzle of CMB anomalies and test the cosmological principle. Further large-scale structure issues, especially non-Gaussianity and relativistic corrections, are discussed in [14].

The ideas presented in this work only provide a flavor of SKA's potential to answer fundamental cosmological questions. Some of those ideas can already be tested by means of the SKA pathfinder experiments ASKAP, MeerKAT and LOFAR, but they cannot compete with SKA's survey speed and sensitivity. Thus SKA will be a unprecedented discovery and precision machine for modern cosmology.

References

[1] G. Hinshaw et al., Astrophys. J. Suppl. **180** (2009) 225 [arXiv:0803.0732].

[2] R. Maartens, Phil. Trans. Roy. Soc. Lond. A **369** (2011) 5115 [arXiv:1104.1300 [astro-ph.CO]].

[3] C. Clarkson, Comptes Rendus Physique **13** (2012) 682 [arXiv:1204.5505 [astro-ph.CO]].

[4] M. Ryle and R.W. Clarke, Mon. Not. Roy. Astron. Soc. **122** (1961) 349.

[5] P. A. R. Ade *et al.* [Planck Collaboration], arXiv:1303.5076 [astro-ph.CO].

[6] P. A. R. Ade *et al.* [Planck Collaboration], arXiv:1303.5082 [astro-ph.CO].

[7] P. A. R. Ade *et al.* [Planck Collaboration], arXiv:1303.5083 [astro-ph.CO].

[8] C. J. Copi, D. Huterer, D. J. Schwarz and G. D. Starkman, arXiv:1310.3831 [astro-ph.CO].

[9] C. J. Copi, D. Huterer, D. J. Schwarz and G. D. Starkman, arXiv:1311.4562 [astro-ph.CO].

[10] C. L. Bennett et al., Astrophys. J. Suppl. **208** (2013) 20 [arXiv:1212.5225 [astro-ph.CO]].

[11] J.-L. Starck, M. J. Fadili and A. Rassat, Astron. Astrophys. **550** (2013) A15 [arXiv:1210.6587 [astro-ph.CO]].

[12] A. Rassat et al., JCAP **1408** (2014) 006 [arXiv:1405.1844 [astro-ph.CO]].

[13] A. L. Erickcek, S. M. Carroll and M. Kamionkowski, Phys. Rev. **D 78** (2008) 083012 [arXiv:0808.1570 [astro-ph]]

[14] S. Camera et al., in "Advancing Astrophysics with the Square Kilometre Array", PoS(AASKA14)025

[15] P. Bull et al., in "Advancing Astrophysics with the Square Kilometre Array", PoS(AASKA14)024

[16] A. Raccanelli et al., in "Advancing Astrophysics with the Square Kilometre Array", PoS(AASKA14)031

[17] G. De Zotti, M. Massardi, M. Negrello and J. Wall, Astron. Astrophys. Rev. **18** (2010) 1.

[18] A. Raccanelli et al., Mon. Not. Roy. Astron. Soc. **424** (2012) 801 [arXiv:1108.0930 [astro-ph.CO]]

[19] G. F. R. Ellis and J. E. Baldwin, Mon. Not. Roy. Astron. Soc. **206** (1984) 377.

[20] C. Blake and J. Wall, Nature **416** (2002) 150 [astro-ph/0203385].

[21] C. Gibelyou and D. Huterer, Mon. Not. Roy. Astron. Soc. **427** (2012) 1994 [arXiv:1205.6476 [astro-ph.CO]].

[22] M. Rubart and D. J. Schwarz, Astron. Astrophys. **555** (2013) A117 [arXiv:1301.5559 [astro-ph.CO]].

[23] P. A. R. Ade *et al.* [Planck Collaboration], arXiv:1303.5087 [astro-ph.CO].

[24] F. Crawford, Astrophys. J. **692** (2009) 887 [arXiv:0810.4520 [astro-ph]].

[25] R. J. Wilman et al., Mon. Not. Roy. Astron. Soc. **388** (2008) 1335 [arXiv:0805.3413 [astro-ph]].

[26] M. Rubart, D. Bacon and D. J. Schwarz, Astron. Astrophys. **565** (2014) A111 [arXiv:1402.0376 [astro-ph.CO]].

[27] C. J. Copi, D. Huterer, D. J. Schwarz and G. D. Starkman, Adv. Astron. 2010 (2010) 847541 [arXiv:1004.5602 [astro-ph.CO]]

[28] E. Hivon et al., Astrophys. J. **567** (2002) 2 [arXive:0105302 [astro-ph]].

[29] P. Paykari, S. Pires, J.-L. Starck and A. H. Jaffe, arXiv:1306.3035 [astro-ph.CO].

[30] R. Maartens, G. -B. Zhao, D. Bacon, K. Koyama and A. Raccanelli, JCAP **1302**, 044 (2013) [arXiv: [astro-ph.CO]].

[31] A. Raccanelli, D. Bertacca, O. Dore and R. Maartens, "Large-scale 3D galaxy correlation function," arXiv:1306.6646 [astro-ph.CO].

[32] A. Raccanelli, D. Bertacca, R. Maartens, C. Clarkson and O. Doré, arXiv:1311.6813 [astro-ph.CO].

[33] C. Song and D.J. Schwarz, arXiv:1407.4682

[34] M. -N. Celerier, Astron. Astrophys. **353** (2000) 63 [astro-ph/9907206].

[35] P. Bull, T. Clifton and P. G. Ferreira, Phys. Rev. D **85**, 024002 (2012) [arXiv:1108.2222 [astro-ph.CO]].

[36] W. Valkenburg, V. Marra and C. Clarkson, Mon. Not. Roy. Astron. Soc. **438**, L6 (2014) [arXiv:1209.4078 [astro-ph.CO]].

[37] D. W. Hogg et al., Astrophys. J. **624** (2005) 54 [astro-ph/0411197].

[38] M. Scrimgeour et al., Mon. Not. Roy. Astron. Soc. **425**, 116 (2012) [arXiv:1205.6812 [astro-ph.CO]].

[39] P. Bull, P. G. Ferreira, P. Patel and M. G. Santos, arXiv:1405.1452 [astro-ph.CO].

[40] S. February, C. Clarkson and R. Maartens, JCAP **1303**, 023 (2013) [arXiv:1206.1602 [astro-ph.CO]].

[41] C. Clarkson, B. Bassett and T. H. -C. Lu, Phys. Rev. Lett. **101** (2008) 011301 [arXiv:0712.3457 [astro-ph]].

Chapter 4

Quadratic Estimators

Look up at the stars and not down at
your feet. Try to make sense of what
you see, and wonder about what makes
the universe exist. Be curious.
— Stephen Hawking

4.1 Comparison to Linear Estimators

Until now we were discussing different kinds of linear estimators. They worked by adding up all the available data points and thereby directly provided a dipole estimation. Those results needed to be modified for masking effects. The big advantage of this linear method is that it is very fast in terms of computational time. Hence, it is possible to investigate a great number of simulated radio maps and thereby understand the estimator better. For example the bias problem described in section 2.1 was found in this way. It was possible to make use of the resulting biased dipole amplitudes, since simulation showed that this bias can be estimated and understood. It was shown that the bias is not sufficient to explain the observed amplitude excess.

The so-called quadratic estimators work on another principle. They are comparing the observational data to a given model and test, how good the assumed model fits to the data. The biggest disadvantage of the quadratic estimators becomes immediately evident. One can only test a finite number of models to the data and is thereby restricted. This means one needs to make specific assumptions before applying the estimator. In this study, the underlying model will be that the radio sky is dominated by a monopole and a dipole contribution, with amplitude and direction for the latter. Assuming this model is valid for the investigated radio surveys, one needs to find all those parameters.

The monopole can be described by a single number m_0 which represents the mean density of radio sources per area on the sky. For a given survey such a mean density could be obtained directly by just dividing the number of sources by the given area. This approach turns out to have two problems. Firstly, the full radio survey contains also radio signals from the Milky Way. One can clearly see an excess in the number of radio sources near the galactic plane in the NVSS. Hence, this area is masked before further studies are performed. So the monopole will be obtained from a radio map, without the area around the galactic plane. Another problem is that the combination of a masked sky map and a dipole modulation within this map can influence the monopole. This effect is discussed in detail in section 2.1.

Those problems are avoided, when the monopole term is not directly obtained from the map but considered as part of the fit model. So one needs to fit at least four parameters: the monopole m_0, the dipole amplitude d as well as the dipole direction, parametrized by two angles φ and ϑ. In order to restrict the computational effort it is useful to first pixelate the radio catalogue. A pixel is defined by an area on a spherical map and to each pixel the number of sources found in that area is assigned. The pixels should all be distinct and chosen in a convenient way.

For this purpose the computer code HEALPix[1] was used. This program was created in order to analyse the CMB as a pixelated map with high resolution. It separates the sky into equally sized pixels, which is very useful for covering the angle parameter space in a uniform way. The number of total pixels across the sky N can be chosen by the so-called n_{side} number. For $n_{\text{side}} = 1$ the code separates the sky into 12 pixels. Increasing n_{side} by a factor of two corresponds to separating each pixel of a $n_{\text{side}}/2$ map into four new pixels of equal size. The relation between n_{side} and the number of pixels is in general given by $N = 12n_{\text{side}}^2$. One needs to decide carefully, how fine the resolution should be. Higher resolutions will enable a more precise measurement but on the other hand it will also increase the needed computational time significantly.

---

[1] Hierarchical Equal Area isoLatitude Pixelization http://healpix.jpl.nasa.gov

The big advantage of the quadratic estimator is that it searches for an actual dipole pattern on the sky. Imagine we have a radio sky, which is very isotropic everywhere expect for one small direction. In this direction we see much more sources than on the rest of the sky. With the linear estimator we would obtain a dipole term, since it is sensitive to an excess of sources on the sky, no matter what kind of distribution underlies this excess. But we are more interested in an anisotropic distribution that goes like a cosine. The quadratic estimator is much more useful in determine, whether a found distribution has really a dipolar pattern, as we can also measure the quality of the fit.

4.2 Method

First of all the catalogue will be pixelated by Healpix. Thereby one obtains a list of N entries with the corresponding pixel centre positions as well as the number of sources inside those pixels. Next a suitable mask is applied. For example one could ignore all sources inside a 10° degree strip of the galactic plane. But due to the pixelized map this translates into ignoring all pixels with a pixel centre that is closer than 10° to the galactic plane. Therefore the mask will not have straight edges. This effect must be considered when the shape of the masked is fixed. In the worst case, almost half a pixel may be inside the so-called masked area. Hence, the mask should be at least half a pixel-size larger than the area one wants to avoid.

Now one needs to decide which values for the four parameters m_0, d, φ and ϑ should be tested. For m_0 a useful approach is to first determine the mean number of sources per pixel. Even so this value cannot be used directly for m_0 (as described above), it will be a very good starting point. One can test a number of values close to this one. After some testing we found that a useful range to search is about 0.5% above and below the direct mean number of sources. This value is also motivated by theory, since the effect of the dipole, combined with the mask, on the monopole should be smaller than the dipole effect itself. In order to test the two dimensional parameter space of φ and ϑ we decided to translate those into pixel positions. When we have a Healpix map with a certain n_{side} value to test, we look at a list of the positions of all those pixels on the sky.

As dipole direction we then test all the pixel positions. The advantage here is that we obtain uniform sky coverage in both angular directions. Also it would not make much sense to test the parameter space at a higher resolution than the data map is given in. We also effectively reduce the number of parameters to three, since we test N different positions now and therefore the direction becomes one free parameter.

The hardest parameter to define an appropriate testing range for, is the dipole amplitude d. It is not possible to determine the best range to test this parameter a priori. Therefore we utilize what we learned from linear estimators as well as what we know from the expected kinetic dipole. We always start to test $d = 0$ and increase this parameter until about $d = 0.05$. The last value is significantly above the results obtained by linear estimators for the NVSS catalogue. If the resulting best-fit parameter turns out to be at this upper limit, one would be forced to test even higher values of d in order to find an even better set of parameters. During this study the mentioned case did never occur.

After those considerations, we end up with a three-dimensional space (since both angular coordinates are combined into one) that must be tested. For each point in this parameter space we calculate

$$\chi^2 = \sum_i \frac{\left(N_{o,i} - N_{m,i}\right)^2}{N_{m,i}} \ , \tag{4.1}$$

where i goes over all pixels that are not masked and $N_{o,i}/N_{m,i}$ are the number of sources in the ith pixel for the observed and the modelled case respectively. This χ^2 value will increase when the model does not give similar results as the tested data set. The number of sources in pixel i for the model are calculated via

$$N_{m,i} = m_0(1 + \vec{d} \cdot \vec{e_i}) \ , \tag{4.2}$$

with $\vec{e_i}$ being a unit vector pointing towards the centre of pixel i and $\vec{d}$ is the full dipole vector (with amplitude d and direction φ_i, ϑ_i). For each set of parameters one obtains a different result for χ^2 and those can be compared with each other. The parameter set leading to the smallest value of χ^2 is considered as the best-fit model. Hence, those parameters are the result of the quadratic estimator.

The quadratic estimator used by Blake & Wall (2002) works differently. They first calculated the spherical harmonic coefficients a_{lm} from the NVSS catalogue up to $l = 3$. The resulting coefficients were fitted to a dipole model, with three free parameters, the amplitude and two angles. Hence, their quadratic estimator operates in spherical harmonic space, while our directly fits the observed sources per pixels.

4.3 Simulations

Even though it is time-intensive in terms of computational time, we performed some simulations in order to test the quadratic estimator before applying it to real data. In this way we can determine a possible bias and also see how precisely we can expect this estimator to perform. We create the same kind of simulated maps like for the linear estimators, but this time we pixelate them. All tests in this section were performed with a HEALPix map at $n_{\text{side}} = 16$. For the simulated dipole we assumed $d = 0.018$, RA$= 154°$ and dec$= -2°$.

We tested the simulated maps with and without masked areas. When a mask was applied we removed pixels within 10° of the galactic plane and also removed pixels below dec$= -40°$. In this way we simulated the case we expect to use on the NVSS catalogue. The number of sources in the masked cases is smaller, but the number of sources per pixel stayed the same. The three cases here correspond to 185649, 1×10^6 and 2×10^6 sources on the whole sky. In order to reduce computation time, the same simulated maps were used for the full-sky and masked-sky cases.

In figure 4.1 we see the dipole amplitude for all three cases with and without a mask applied. The error bars correspond to the empirical variance, determined by 100 simulations for each measurement. We see that the dipole amplitudes are above the value an unbiased estimator should have shown. When the number of sources per pixel is increased, this bias decreases. At more than 600 sources per pixel the bias vanishes. Hence, we can argue that this bias is due to shot noise, like it was for the linear estimator.

Another feature we can see is that the estimated dipole amplitudes for the masked case are above those for the full-sky case. This can be explained by the shot noise contribution, since the masked sky always has a smaller

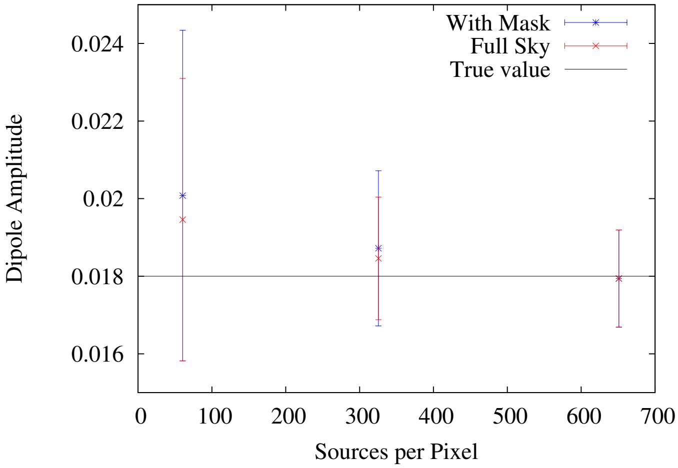

Figure 4.1: Comparison of the simulated and measured mean dipole amplitude with 100 runs. Assumed velocity of observer is $v = 1440\frac{\mathrm{km}}{\mathrm{s}}$ towards dec $= -2°$ and RA $= 154°$, for the masked case all pixels with dec $< -40°$ or $|b| < 10°$ are masked, pixel resolution is $n_{\mathrm{side}} = 16$. Error bars correspond to statistical variance for a single measurement.

number of total sources, compared to a full-sky observation with the same number of sources per pixel.

The error bars are smaller than those we got for a linear estimator by a factor of about 2/3. This suggests that the quadratic estimator will be able to perform a more precise measurement of the dipole amplitude. All in all the amplitude measurement works reasonably well in the simulated cases.

In figure 4.2 we see the resulting directions for the simulated maps. Here the quadratic estimator does not show any bias towards a certain direction, for both the full sky as well as the masked sky case. The higher empirical variance for the masked sky results can again be explained by the lower number of total sources and thereby increased shot noise.

One additional effect for the quadratic estimators is that the direction estimation is limited by the pixel resolution. Each simulation run will result

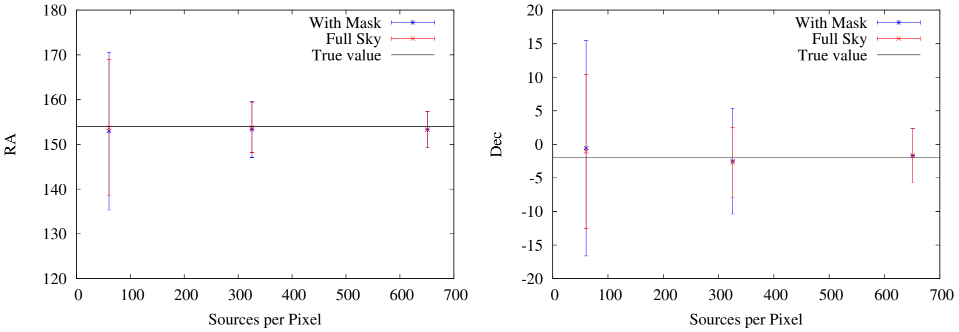

Figure 4.2: Comparison of the simulated and measured mean dipole directions with 100 runs. Assumed velocity of observer is $v = 1440 \frac{\mathrm{km}}{\mathrm{s}}$ towards dec $= -2^\circ$ and RA $= 154^\circ$, for the masked case all pixels with dec $< -40^\circ$ or $|b| < 10^\circ$ are masked, pixel resolution is $n_{\mathrm{side}} = 16$. Error bars correspond to statistical variance for a single measurement.

in a best fit, corresponding to the centre position of one pixel. Therefore one always needs to add half the spacing between two pixel centres to the error budget. The mean distance between two pixels for a resolution of $n_{\mathrm{side}} = 16$ is about 3.66° and therefore we added 1.83° as uncertainty to the simulated results later. The same goes for the dipole amplitude. This amplitude is measured with certain dipole values, which are 0.2×10^{-2} apart. Hence, we always need to add 0.1×10^{-2} to the resulting dipole amplitudes. Both effects can be reduced by increasing the resolution of the estimator, but this will also increase the computational time significantly.

For the linear estimator, we found biasing effects in amplitude and direction measurements, when the tested maps included masked areas. This is due to the fact that the linear estimator is not sensitive to the actual form of an anisotropic source distribution. For the quadratic estimator we do not see such an effect in figure 4.1 or 4.2. In principle this could be a special case. Hence, we also did simulations for the case of a simulated dipole near the edge of a mask, like in section 3.1. For the linear estimator, such setup leads to a significant directional bias.

	d	right ascension	declination
	(10^{-2})	$(^\circ)$	$(^\circ)$
Implemented	1.8	180	-40
Measured	$1.77 \pm 0.03 \pm 0.1$	$180.2 \pm 0.8 \pm 1.9$	$-36.7 \pm 0.9 \pm 1.9$

Table 4.1: Comparison of the implemented and measured mean dipole values for 99 runs with 10^6 sources each. Assumed velocity of observer is $v = 1440 \frac{\mathrm{km}}{\mathrm{s}}$, all pixels with $|\mathrm{dec}| > 40^\circ$ are masked, pixel resolution is $n_{\mathrm{side}} = 16$. Error bars correspond to statistical variance and resolution limitation.

In table 4.1 we see a comparison of the implemented dipole and the simulated measurement. The obtained dipole amplitude and right ascension values from the simulations fit very well to the implemented ones. The declination estimations seem to be a little bit too small. One point to mention is that the closest pixel to the implemented dipole position is at $\mathrm{RA} = 180^\circ$ and $\mathrm{dec} = -38.68^\circ$. Hence, we expect a better fit in right ascension and a small bias towards smaller declination values. Another point is that there will be a small shot noise contribution in every measurement. This can only have an effect inside the observed ring and therefore slightly bias the estimation to higher declination values, since no pixel with smaller values than $\mathrm{dec} = -40^\circ$ was taken into account. Since the measured declination value is still within two sigma of the simulated dipole direction, we do not consider this as a problem here.

All in all we do not see a significant masking bias for the quadratic estimator. This makes the quadratic estimator much more useful than the linear ones, since the resulting dipole values are expected to be unbiased (except a small shot noise bias towards higher dipole amplitudes for low numbers of sources). Due to resolution effects, we will need to include an extra error bar, but apart from this we expect smaller uncertainties for the quadratic estimator in comparison to the linear ones.

4.4 Result

With the quadratic estimator, we now have the means to compare the quality of different fits with each other, by utilizing the resulting values of χ^2. In other words, when different masks give different results, we now can evaluate, which map can be better described by a model based on monopole and dipole. Since different masks result in a different number of pixels, which are still accepted for the estimation, a direct comparison of the χ^2 values is not useful. Therefore we calculate χ^2/dof, where dof is the degrees of freedom of that fit. The number of pixels fitted depends on the mask and is labelled N_p. For each parameter we need to subtract one from the pixel number, to take into account that the parameters reduce the degrees of freedom of the fit. Each fit has three parameters (the two directions count as one parameter here, since they are merged in an ordered list of pixel positions) and we get $\text{dof} = N_p - 3$.

We used the quadratic estimator to analyse the NVSS catalogue. In order to obtain results that are convenient to compare to those of the linear estimators, we restricted ourselves to a lower flux limit of 25 mJy here. Our masks have two parameters, $|b|$ and dec_{mask}. The galactic plane is cut out by removing all pixels within $|b|$ degrees of the galactic plane. Higher values for $|b|$ will protect the estimation from galactic influences and therefore making the extragalactic dipole measurement more stable. On the other hand, too high values of $|b|$ will reduce the number of used sources and thereby increase the shot noise contribution. Hence, we will test different masking parameters and judge them, depending on the fit quality χ^2/dof. A good choice should be the lowest possible value of $|b|$, which does not increase χ^2/dof significantly.

Since the NVSS survey has no sources below declinations of $-40°$, we also need to ignore all pixels lying (at least partly) in this area. As described in section 1.6, the NVSS has used different configurations for different declinations. With the quadratic estimator we are now able to test, whether those different configurations influence the dipole measurement. Hence, we tested the quadratic estimator with different values for the lowest declination, where pixels where still accepted.

In table 4.2 we see the result of the quadratic estimator for a Healpix resolution of $n_{\text{side}} = 16$ for different masking values. One result that can be seen clearly is that $|b| = 5°$ leads to a very poor fit quality ($\chi^2/\text{dof} > 2$).

N_t	N_0	RA	dec	d	$\lvert b\rvert$	dec$_{\text{mask}}$	χ^2/dof
		(°)	(°)	(10^{-2})	(°)	(°)	
150397	109.82	87.19	41.81	2.6	5	0	3.5827
135524	**109.39**	**157.50**	**2.39**	**1.0**	**10**	**0**	**1.1879**
121278	109.43	154.69	-9.59	1.2	15	0	1.2096
107350	109.64	149.06	-19.47	1.4	20	0	1.2081
166440	109.65	129.38	-16.96	1.4	10	-10	1.3085
133604	109.79	129.38	-22.02	1.8	20	-10	1.2692
190429	109.67	140.63	-12.02	1.6	10	-20	1.2572
153841	109.39	140.63	-7.18	2.0	20	-20	1.2238
242031	110.01	115.31	35.69	2.4	5	-35	2.7554
220237	**109.68**	**143.44**	**-9.59**	**1.8**	**10**	**-35**	**1.2526**
178243	109.70	146.25	-22.02	2.2	20	-35	1.2223

Table 4.2: Results for the NVSS catalogue with the quadratic estimator with different masked areas and resolution $n_{\text{side}} = 16$. The boldface results will discussed in detail.

We can conclude that the galactic plane did have an impact in those cases. Since our model does not take our galaxy into account, the fit gets poor. For higher values of $|b|$ we do not see any significant dependence of χ^2/dof on this masking parameter. Therefore we assume, it is save to use a value of $|b| = 10°$.

Another effect of $|b|$ we can observe is that higher galactic cuts lead to higher dipole amplitudes. Here one needs to keep in mind that all estimates in table 4.2 are highly correlated, since the underlying data are always the NVSS catalogue. So we do not have a number of independent measurements of this effect, we see that it does not depend on dec$_{\text{mask}}$. The fits with higher $|b|$ values are also those with slightly lower χ^2/dof, indicating a better fit to the dipole model. On the other hand the number of sources is smaller, when the masked area is increased. Hence, a smaller value of $|b|$ generally leads to less shot noise contribution.

In table 4.3 the results of the quadratic estimator with a smaller resolution ($n_{\text{side}} = 8$) for the NVSS catalogue are given. For the masking of the galactic plane we see exactly the same effect like we saw for the higher resolution previously. The number of total sources with $n_{\text{side}} = 8$

N_t	N_0	RA	dec	d	$\|b\|$	$\mathrm{dec}_{\mathrm{mask}}$	χ^2/dof
		(°)	(°)	(10^{-2})	(°)	(°)	
147535	439.25	123.75	-4.78	1.0	5	0	3.6723
130811	438.22	157.50	-35.69	1.4	10	0	1.2715
118658	437.70	163.13	-30.00	1.4	15	0	1.2945
105642	437.99	146.25	-24.62	1.6	20	0	1.3294
167820	438.49	135.00	-35.69	1.6	10	-10	1.3074
137224	438.48	129.38	-19.47	2.2	20	-10	1.3129
192025	437.88	146.25	-24.62	1.6	10	-20	1.3046
157945	437.04	135.00	-4.78	2.0	20	-20	1.306
239548	439.39	140.63	0.00	1.4	5	-35	2.7906
215725	437.42	151.88	-19.47	1.6	10	-35	1.2870
177855	437.72	140.63	-19.47	2.2	20	-35	1.2802

Table 4.3: Results for the NVSS catalogue with the quadratic estimator with different masked areas and resolution $n_{\mathrm{side}} = 8$.

are slightly below those in table 4.2. This comes from the fact that we actually mask more area here, since the pixels are bigger. So over all we have less sources and this may also explain, why the χ^2/dof values are increased a little bit in comparison. Another effect is that we fit a cosine to a pixelated map. This fit will be best, when the pixel size is small so that the cosine describes the map in an optimal way. Hence, we will focus on the results with the higher ($n_{\mathrm{side}} = 16$) resolution from now on.

In order to estimate the error bars for the evaluated parameters we again utilize simulated radio maps. By implementing our resulted dipole vectors and creating 100 simulated maps each, we are able to determine the statistical variance of those simulations. This variance will then be added to the resolution limitation (1.83° in each direction and 0.1×10^{-2} in amplitude). Due to the time performing those simulations, we focused on only two of our measurements from above, which are both in bold face in the table. The first one is the second result in table 4.2, since it has the smallest χ^2/dof value. The second one will be the next to last case in table 4.2, since it hast the most sources included, without suffering from the galactic-plane bias.

First of all we see that the first case considered in table 4.4 shows con-

N_t	RA	dec	d	$\|b\|$	$\mathrm{dec}_{\mathrm{mask}}$	χ^2/dof
	(°)	(°)	(10^{-2})	(°)	(°)	
135524	158 ± 30	2 ± 38	1.0 ± 0.5	10	0	1.1879
220237	143 ± 13	-10 ± 16	1.8 ± 0.5	10	-35	1.2526

Table 4.4: Final results for the NVSS catalogue with the quadratic estimator with different masked areas and resolution $n_{\mathrm{side}} = 16$. The error bars represent the statistical variance of 100 simulations plus the resolution limit.

siderably higher directional error bars than the second. The main reasons are: (a) the comparably small dipole amplitude, which makes the direction estimation harder and (b) the lower total source number that leads to a larger shot noise contribution. Hence, this case may feature the best fit in terms of χ^2/dof, but in terms of uncertainty this result is not as good as the second one in table 4.4.

For both cases we run the quadratic estimator again, now with a finer grid in position space. The possible dipole directions were tested with $n_{\mathrm{side}} = 32$ now, while the catalogue itself was still pixelized with $n_{\mathrm{side}} = 16$. This will reduce the resolution limit of the estimated direction from 1.83° to 0.92° and hence the overall directional error bars went all down by 1°. Not increasing the map resolution limited the necessary computational time.

N_t	RA	dec	d	$\|b\|$	$\mathrm{dec}_{\mathrm{mask}}$	χ^2/dof
	(°)	(°)	(10^{-2})	(°)	(°)	
135524	159 ± 29	2 ± 37	1.0 ± 0.5	10	0	1.1870
220237	143 ± 12	-11 ± 15	1.8 ± 0.5	10	-35	1.2526

Table 4.5: Final results for the NVSS catalogue with the quadratic estimator with different masked areas and pixel resolution $n_{\mathrm{side}} = 16$. Dipole positions were tested on a $n_{\mathrm{side}} = 32$ grid. The error bars represent the statistical variance of 100 simulations (with grid resolution of $n_{\mathrm{side}} = 16$) plus the resolution limit.

We see that the results in table 4.5 are in very good agreement with the previous results. This verifies that our estimator is stable w.r.t. changing the grid. The obtained values of χ^2/dof changed only marginally. Hence, the finer grid did not improve the fit quality. The error bars are based on the same simulations as in table 4.4, since 100 simulations with the finer grid would have needed significantly more time and we expect no noticeable change in the resulting error estimation anyhow.

Our final result for the NVSS using the quadratic estimator described in this section is therefore a dipole with amplitude $(1.8 \pm 0.5) \times 10^{-2}$ towards $\mathrm{RA} = 143° \pm 12°$ and $\mathrm{dec} = -11° \pm 15°$. The amplitude is the same we got from the linear estimator with almost the same uncertainty. We take this as verification for both methods. Again the amplitude is significantly above the expectation $(0.48 \pm 0.04) \times 10^{-2}$ from the CMB dipole. This excess is therefore unlikely to be due to systematic effects of the two estimator types, since both resulted in the same amplitude.

In comparison to the linear estimator we obtained smaller error bars for the direction estimation. Within their one-sigma error bars both estimators agree on the dipole direction. Due to the masking bias in direction for the linear estimator, the results of the quadratic estimator are superior. The obtained declination is in very good agreement with the CMB expectation ($\mathrm{dec}_{\mathrm{CMB}} = -7°$). For the right ascension value we see a difference, but the CMB expectation ($\mathrm{RA}_{\mathrm{CMB}} = 168°$) is only marginally outside the two sigma contours of this estimation. Therefore we do not see a strong discrepancy between the CMB and the radio dipole direction using NVSS.

The WENSS catalogue (Rengelink et al. 1997) includes sources from a smaller area ($\approx \pi$) in comparison to the NVSS survey and has therefore less sources overall. Since WENSS represents a completely independent observation it is interesting to test this survey for the radio dipole, like it was done with a two-dimensional linear estimator in Rubart & Schwarz (2013) already. The quadratic estimator is able to estimate the full dipole direction of WENSS, not only the right ascension coordinate.

On the other hand the quadratic estimator might be sensitive to the fact that WENSS consists of two surveys: the main ($28° < \mathrm{dec} < 76°$) and the polar catalogue ($\mathrm{dec} > 72°$). This leads to a source density changing with declination. For the previously applied two-dimensional estimator, this characteristic was irrelevant, but for the quadratic estimator it may spoil the dipole measurement. Hence, we tested the WENSS catalogue (a) completely and (b) only with sources belonging to the main catalogue, i.e. we tested two different declination areas ($\mathrm{dec}_{\mathrm{area}}$). Additionally we masked all sources within 10° of the galactic plane ($|b| < 10°$) like we did for the NVSS.

N_t	RA	dec	d	$\lvert b\rvert$	$\mathrm{dec}_{\mathrm{area}}$	χ^2/dof
	(°)	(°)	(10^{-2})	(°)	(°)	
110821	149	-25	2.0	10	$35-90$	1.7743
85285	118 ± 39	-7 ± 24	1.6 ± 0.8	10	$35-65$	1.2191

Table 4.6: Results for the WENSS catalogue with the quadratic estimator with different masked areas and pixel resolution $n_{\mathrm{side}} = 16$. The error bars in the second case represent the statistical variance of 100 simulations plus the resolution limit.

In table 4.6 we see the dipole estimation results for the WENSS catalogue. The fit quality χ^2/dof for the first case is very poor in comparison to the second one and to the NVSS results. This is due to the combination of two distinct surveys to the full WENSS catalogue. Hence, the result for the whole WENSS catalogue is unfeasible for our purpose. The result for the main catalogue with declinations between 35° and 65° shows a significantly lower value of χ^2/dof, which is close the χ^2/dof values from the NVSS dipole estimations above. We ran simulations for that result only, in order to estimate the measurement uncertainty.

Due to the lower number of total sources as well as the low number of usable pixels (396), the resulting shot noise uncertainties for the WENSS dipole estimation are significantly higher than for the NVSS. Within their error bars both results are in agreement, the main difference being a different right ascension estimation, which is 25° apart. The estimations for declination and dipole amplitude for the WENSS and NVSS catalogue are remarkable close to each other.

The resulting right ascension for WENSS is in almost perfect agreement with the result from the linear estimator (Rubart & Schwarz 2013). The amplitude is lower for the quadratic estimator, which can be explained by (a) a different applied mask and (b) the fact that the quadratic estimator is more sensitive to the shape of an anisotropic source distribution than the linear estimator is. The final result for the WENSS dipole estimation has an amplitude of $(1.6 \pm 0.8) \times 10^{-2}$ towards RA $= 118° \pm 39°$ and dec $= -7° \pm 24°$. On the one hand this is in agreement with the CMB dipole but on the other hand the case of no dipole cannot be excluded from this estimation. In the end the WENSS catalogue provides not enough sources for effective dipole estimation.

Now we discuss the overall goodness of the presented fits. The first result in table 4.5 has the lowest value of χ^2/dof for all cases discussed here. The chi-square distribution can be used to evaluate the likelihood, to find a certain χ^2-value, given the degrees of freedom of the fit. We did this with the program "Mathematica" and found that the likelihood for this result is only $p = 5 \times 10^{-6}$. This means that the fit has a very poor quality. Even worse is the likelihood for the second row in table 4.5, which is only $p = 5 \times 10^{-14}$.

The reason for the poor fit qualities is that we modelled the distribution of sources across the sky only by monopole and dipole. Of course the universe cannot be described by those two multipoles only, but it features a much more complex distribution of matter. Local or large-scale structures, like discussed in chapter 1.2, are not part of our model. Hence, we do expect an increased χ^2 value for our estimator.

Our simulations did not include structure and hence they should provide a much better fit, for a pure mono- and dipole model. The resulting values of χ^2/dof for the two NVSS simulations mentioned above are χ^2/dof $=0.991 \pm 0.040$ (mean and statistical variance) for the first case in table 4.5 and $\chi^2/\mathrm{dof} = 0.998 \pm 0.033$ for the second. So we obtain almost perfect fits for our simulations.

The result using the WENSS catalogue has a p-value of 0.001915, which is much better than the ones from the NVSS fits. This is most likely due to the smaller number of sources and pixels. With less data it is harder to exclude a certain model with high significance and hence the p-value cannot be as small as in the previous cases. The simulation for the WENSS catalogue had a mean value of $\chi^2/\mathrm{dof} = 1.001 \pm 0.066$. Again the simulations provided better fits, since they did not include any structure effects.

We learn from this estimator that local structure is relevant and the effects of such structures on the dipole are discussed in the following chapter.

Chapter 5

Voids and Dipole

Something wicked this way comes.
— Shakespeare, Macbeth

5.1 Publication A&A 565, A111 (2014)

The following publication was written by the first author and edited by the second and third one. In this work, the effect local structure (i.e. a void) has on the radio dipole amplitude is discussed. It is shown that a void may increase the dipole amplitude without having an effect on the dipole direction.

In order to quantify this effect, local structures are modelled by spherical shells of equal densities. It is shown how the dipole amplitude contribution depends on the position of the observer relative to the structure's centre. The introduced formalism is tested with simulations and is well confirmed.

Observed voids are used in order to estimate the expected dipole amplitude contribution from such structures. It is shown that the effect from a single realistic void is not big enough to explain the observed excess in radio dipole estimations to full extent. But on the other hand, local structures do play a role and may explain a significant fraction of the excess.

In order to distinguish the contribution of local structure from a kinematic dipole, two effects were analysed. First of all it was shown that the line of sight dependence for both cases is identical, if the observer is inside such a structure. Secondly it was shown that local structure effects have frequency dependence. The latter effect may be used in order to distinguish a kinetic from a structure dipole.

A&A 565, A111 (2014)
DOI: 10.1051/0004-6361/201423583

Astronomy & Astrophysics

Impact of local structure on the cosmic radio dipole

Matthias Rubart[1], David Bacon[2], and Dominik J. Schwarz[1]

[1] Fakultät für Physik, Universität Bielefeld, Postfach 100131, 33501 Bielefeld, Germany
e-mail: `matthiasr@physik.uni-bielefeld.de`
[2] Institute of Cosmology and Gravitation, University of Portsmouth, Burnaby Road, Portsmouth PO1 3FX, UK

Received 6 February 2014 / Accepted 12 April 2014

ABSTRACT

We investigate the contribution that a local over- or under-density can have on linear cosmic dipole estimations. We focus here on radio surveys, such as the NRAO VLA Sky Survey (NVSS), and forthcoming surveys such as those with the LOw Frequency ARray (LOFAR), the Australian Square Kilometre Array Pathfinder (ASKAP) and the Square Kilometre Array (SKA). The NVSS has already been used to estimate the cosmic radio dipole; it was shown recently that this radio dipole amplitude is larger than expected from a purely kinematic effect, assuming the velocity inferred from the dipole of the cosmic microwave background. We show here that a significant contribution to this excess could come from a local void or similar structure. In contrast to the kinetic contribution to the radio dipole, the structure dipole depends on the flux threshold of the survey and the wave band, which opens an opportunity to distinguish the two contributions.

Key words. large-scale structure of Universe – radio continuum: galaxies – galaxies: clusters: general

1. Introduction

In recent years, the dipole anisotropy in radio surveys, such as the NVSS catalogue (Condon et al. 1998), has been investigated (e.g. Blake & Wall 2002; Singal 2011; Gibelyou & Huterer 2012; Rubart & Schwarz 2013; and Kothari et al. 2013). It appears that the cosmic radio dipole has a similar direction to the one found in the cosmic microwave background (CMB), but with a significantly higher amplitude (by a factor of three to four, based on different estimators and surveys, Singal 2011; Rubart & Schwarz 2013). In this work we investigate one possible effect which can increase the dipole amplitude observed in radio surveys, with respect to the CMB dipole.

There have recently been studies (e.g. Keenan et al. 2013 and Whitbourn & Shanks 2014) which claim that the local universe (i.e. on scales of 300 Mpc) has an atypically low density of galaxies. If we do live in such a region, what would we expect to see regarding the observed cosmic radio dipole? We are unlikely to be living in the very centre of such a void, so there will be some offset distance between us and the centre of the void, which we call $\boldsymbol{r}_{\mathrm{v}}$. If we imagine a sphere around the observer (in our case the Local Group), with a radius R_{o} greater than the void radius R_{v}, we will expect to see more galaxies in one direction than in the other.

It is likely that the Local Group moves towards the direction where we see more galaxies, due to their gravitational pull. This direction has been determined to be $(l, b) = (276° \pm 3°, 30° \pm 3°)$ (Kogut et al. 1993) in galactic coordinates. The CMB dipole, $(l, b) = (263.99° \pm 0.14°, 48.26° \pm 0.03°)$ from Hinshaw et al. (2009), is caused by the motion of the Sun relative to the CMB, while the radio dipole, $(l, b) = (248° \pm 28°, 46° \pm 19°)$ from Rubart & Schwarz (2013), can be expected to receive contributions from the motion of the solar system with respect to the CMB (kinetic dipole) and due to the uneven galaxy distribution (structure dipole). Within the current accuracy, the direction of the radio dipole agrees with the CMB direction as well as with the motion of the Local Group with respect to the CMB. Therefore we expect the contribution of a local void to the radio dipole to add up with the velocity dipole, resulting in a larger dipole amplitude in radio surveys.

The local structures considered in this work are not in conflict with the Copernican principle, as they are much smaller than the Hubble scale and thus a fine tuning of the position of the observer with respect to the centre of a void is not required. This is different to scenarios in which huge voids have been invoked to provide an alternative explanation of dark energy (e.g. Celerier 2000; Alnes et al. 2006; Alnes & Amarzguioui 2006).

In this work, we will investigate this chain of thought in a more quantitative manner. Our model will be discussed in Sect. 2, followed by detailed testing in Sect. 3. In Sect. 4 we will examine the effects of realistic voids on the dipole, and we will present our conclusions in Sect. 5.

2. Model

For simplicity we model the observed universe limited by a radius of R_{o} and with constant mean number density of sources everywhere (except in the area occupied by the void). Therefore the results of this section cannot directly be compared to radio surveys. The more realistic case of a flux limited observation, with certain number counts, is discussed in Sect. 4.

The configuration of our model can be seen in Fig. 1. We consider a density contrast $\delta(r)$ in a region with radius R_{v}, which we will call a void (but could be any amount of over- or under-density). We can restrict the calculation to the regions where $\delta(r) \neq 0$, as the contribution of the mean density to the dipole amplitude vanishes due to isotropy.

Article published by EDP Sciences

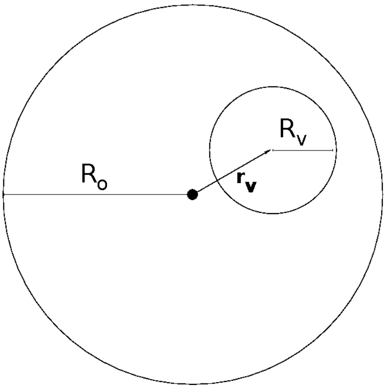

Fig. 1. Configuration of our model of the observed volume-limited universe (radius R_o) with a void of size R_v at distance r_v from the observer.

For the dipole measurement we use the linear estimator introduced by Crawford (2009),

$$\boldsymbol{d} = \frac{1}{N}\sum_{i=1}^{N} \hat{\boldsymbol{r}}_i, \tag{1}$$

where $\hat{\boldsymbol{r}}_i$ is the normalized direction of source i on the sky as seen by an observer in the centre of the observed universe. The fact that this estimator is linear is a big advantage here, since we can sum up the contributions of the background, of voids and of over-densities in an additive way. With a quadratic estimator this would not work out so trivially.

In order to simplify the integration, we pick a coordinate system centred on the void. The expectation of the observed dipole from the void, measured with the estimator (1), will be

$$\langle \boldsymbol{d} \rangle = \bar{\alpha} \int_0^{2\pi} \mathrm{d}\varphi \int_{-1}^{1} \mathrm{d}\cos\vartheta \int_0^{R_\mathrm{v}} \mathrm{d}r\, \delta(r) r^2 \frac{\boldsymbol{r} - \boldsymbol{r}_\mathrm{v}}{|\boldsymbol{r} - \boldsymbol{r}_\mathrm{v}|}\cdot \tag{2}$$

Here we have a normalization factor $\bar{\alpha}$.

As a first case, we assume a constant density contrast δ in the void, and an offset $\boldsymbol{r}_\mathrm{v}$ of the void in direction $\hat{\boldsymbol{z}}$,

$$\langle d_z \rangle = \bar{\alpha}\, \delta \int_0^{2\pi} \mathrm{d}\varphi \int_{-1}^{1} \mathrm{d}\cos\vartheta \int_0^{R_\mathrm{v}} \mathrm{d}r\, r^2 \frac{r\cos\vartheta - r_\mathrm{v}}{\sqrt{r^2 - 2\cos\vartheta r r_\mathrm{v} + r_\mathrm{v}^2}}\cdot \tag{3}$$

This leads to

$$\begin{aligned}\langle \boldsymbol{d} \rangle &= \frac{4\pi}{3}\bar{\alpha}\,\hat{\boldsymbol{r}}_\mathrm{v}\,\delta R_\mathrm{v}^3 \left[\Theta\left(R_\mathrm{v} - r_\mathrm{v}\right)\left(\frac{r_\mathrm{v}}{R_\mathrm{v}} - \frac{1}{5}\frac{r_\mathrm{v}^3}{R_\mathrm{v}^3}\right)\right. \\ &\quad \left. + \Theta\left(r_\mathrm{v} - R_\mathrm{v}\right)\left(1 - \frac{1}{5}\frac{R_\mathrm{v}^2}{r_\mathrm{v}^2}\right)\right],\end{aligned} \tag{4}$$

where Θ is the Heaviside function. This formula provides the dipole contribution of a top hat over- or underdensity for an observer inside or outside the void.

Our aim is to investigate void regions with arbitrary density contrast profiles $\delta(r)$. In order to do so, we can heuristically linearly add up a large number N of these voids to get to a smooth distribution $\delta(r)$.

The normalization factor $\bar{\alpha}$ in (4) can be found by the requirement that the integration over a sphere (with radius R_o bigger than the void size R_v) should equal unity,

$$1 = \bar{\alpha} 4\pi \left(\int_{R_\mathrm{v}}^{R_\mathrm{o}} \mathrm{d}r\, r^2 + \int_0^{R_\mathrm{v}} \mathrm{d}r\, r^2 (1 + \delta(r)) \right), \tag{5}$$

leading to

$$\bar{\alpha} = \frac{3}{4\pi} \frac{1}{R_\mathrm{o}^3 + 3\int_0^{R_\mathrm{v}} \mathrm{d}r\, r^2 \delta(r)}\cdot \tag{6}$$

We can see that the prefactor $\frac{3}{4\pi}$ cancels in (4). For convenience we introduce $\alpha = \frac{4\pi}{3}\bar{\alpha}$ for all following formulae.

Let us consider the limit of a distant void $r_\mathrm{v} \gg R_\mathrm{v}$. Then we obtain

$$\lim_{r_\mathrm{v} \gg R_\mathrm{v}} \langle d_z \rangle = \delta \frac{R_\mathrm{v}^3}{R_\mathrm{o}^3}\cdot \tag{7}$$

So the dipole amplitude due to a void depends on the density contrast of the void and on the fraction of volume it occupies in the observed universe.

For a realistic case of a flux limited observation of the universe, we need to generalise this formula to

$$\lim_{r_\mathrm{v} \gg R_\mathrm{v}} \langle d_z \rangle \approx \delta \frac{\tilde{N}_\mathrm{v}}{N_\mathrm{o}}\cdot \tag{8}$$

Here N_o is the number of sources in the observed universe and $\tilde{N}_\mathrm{v}$ is the number of sources we expect to see in the area occupied by the void, if it had the same mean number density as the rest of the universe. This number does depend on the flux limit, on the functional shape of the number counts and on the distance and size of the void.

2.1. *Observers outside the void*

Now we want to derive the expectation value of the dipole amplitude from voids with a density contrast $\delta(r)$, which is not constant. To do so, we will add up N concentric voids, resulting in a structure of N concentric shells, each with constant density contrast $\delta_i, i = 1, \ldots, N$. The shells are ordered by their radius, starting at the shell with the biggest radius (shell number 1).

We only look at the absolute value of $\langle \boldsymbol{d} \rangle$, since for symmetry reasons, the direction of this expectation value will always be $\hat{\boldsymbol{r}}_\mathrm{v}$. First we look at N voids as observed from outside the voids, thus $r_\mathrm{v} > R_\mathrm{v}$. The second term in (4) will give N terms, which can be written as

$$\begin{aligned}|d_z| &= \alpha \left[\delta_1 R_1^3 \left(1 - \frac{1}{5}\frac{R_1^2}{r_\mathrm{v}^2}\right) + (\delta_2 - \delta_1) R_2^3 \left(1 - \frac{1}{5}\frac{R_2^2}{r_\mathrm{v}^2}\right)\right. \\ &\quad \left. + \ldots + (\delta_N - \delta_{N-1}) R_N^3 \left(1 - \frac{1}{5}\frac{R_N^3}{r_\mathrm{v}^2}\right)\right]\cdot\end{aligned} \tag{9}$$

From this we obtain

$$\begin{aligned}|d_z| &= \alpha \delta_N R_N^3 \left(1 - \frac{1}{5}\frac{R_N^2}{r_\mathrm{v}^2}\right) \\ &\quad + \alpha \sum_{i=1}^{N-1} \delta_i \left(R_i^3 - \frac{1}{5}\frac{R_i^5}{r_\mathrm{v}^2} - R_{i+1}^3 + \frac{1}{5}\frac{R_{i+1}^5}{r_\mathrm{v}^2}\right)\cdot\end{aligned} \tag{10}$$

Now we take the difference in size between consecutive shells to be infinitesimally small, meaning $R_{i+1} = R_i - \epsilon$. Without loss of generality, we can put $R_1 = r_\mathrm{v}$ and therefore place the observer on the edge of the biggest void shell (if $r_\mathrm{v} > R_\mathrm{v}$ then $\delta(r)|_{r>R_\mathrm{v}} = 0$). The innermost void shell will have a vanishing radius and so $R_N = 0$. This leads to

$$|d_z| = \alpha \sum_{i=1}^{N-1} \delta_i \left(3R_i^2 \epsilon - \frac{R_i^4 \epsilon}{r_\mathrm{v}^2} \right), \tag{11}$$

which can be written in the form of an integral

$$|d_z| = \alpha \int_0^{r_\mathrm{v}} \mathrm{d}r\, \mathrm{r}^2 \delta(\mathrm{r}) \left(3 - \frac{\mathrm{r}^2}{\mathrm{r}_\mathrm{v}^2} \right). \tag{12}$$

This is the equation we have been seeking for the dipole observed by an observer outside the void.

2.2. Observers inside the void

Now we examine the case of N void shells, each of constant density, with $r_\mathrm{v} \leq R_\mathrm{v}$; the observer is inside the void. We have

$$\begin{aligned} |d_z| &= \alpha \left[\delta_1 \left(R_1^2 r_\mathrm{v} - \frac{1}{5} r_\mathrm{v}^3 \right) + (\delta_2 - \delta_1) \left(R_2^2 r_\mathrm{v} - \frac{1}{5} r_\mathrm{v}^3 \right) \right. \\ &\left. \quad + \ldots + (\delta_N - \delta_{N-1}) \left(R_N^2 r_\mathrm{v} - \frac{1}{5} r_\mathrm{v}^3 \right) \right]. \end{aligned} \tag{13}$$

This can be rewritten as

$$|d_z| = \alpha \delta_N \left(R_N^2 r_\mathrm{v} - \frac{1}{5} r_\mathrm{v}^3 \right) + \alpha \sum_{i=1}^{N-1} \delta_i \left(R_i^2 r_\mathrm{v} - R_{i+1}^2 r_\mathrm{v} \right). \tag{14}$$

Again we make the difference in size between consecutive void shells infinitesimally small, meaning $R_{i+1} = R_i - \epsilon$. The shell with the smallest radius that still includes the observer ($r_\mathrm{v} \leq R_\mathrm{v}$), will have $R_{vN} = r_\mathrm{v}$ and $\delta_N = \delta(r_\mathrm{v})$. The void shell with the biggest radius will have $R_1 = R_\mathrm{v}$. This leads to

$$|d_z| = \frac{4}{5} \alpha \delta(r_\mathrm{v}) r_\mathrm{v}^3 - 2\alpha r_\mathrm{v} \sum_{i=1}^{N-1} \delta_i R_{vi} \epsilon, \tag{15}$$

which can be written as an integral

$$|d_z| = \frac{4}{5} \alpha r_\mathrm{v}^3 \delta(r_\mathrm{v}) + 2\alpha r_\mathrm{v} \int_{r_\mathrm{v}}^{R_\mathrm{v}} \mathrm{d}r\, r \delta(r). \tag{16}$$

This is the form we have been seeking for the dipole observed when the observer is inside a void.

2.3. Structure dipole amplitude

When combining the results for an observer inside a void (Sect. 2.2) and those for an observer outside the void (Sect. 2.1), we need to be careful. The void shell at the position of the observer r_v and density contrast $\delta(r_\mathrm{v})$ has been counted in both cases. The formula for an observer outside the void (12) gives $\frac{4}{5}\alpha\delta(r_\mathrm{v}) r_\mathrm{v}^3$, which is the same result we find for the observer inside the void (16) with $\delta(r)|_{r<R_\mathrm{v}} = \delta(r_\mathrm{v})$. Therefore we need to subtract this term once when combining both cases. We obtain

$$\begin{aligned} \langle \boldsymbol{d} \rangle &= \alpha \hat{\boldsymbol{r}}_\mathrm{v} \int_0^{\min(r_\mathrm{v}, R_\mathrm{v})} \mathrm{d}r\, r^2 \delta(r) \left(3 - \frac{r^2}{r_\mathrm{v}^2} \right) \\ &\quad + \alpha \hat{\boldsymbol{r}}_\mathbf{v} \Theta(R_\mathrm{v} - r_\mathrm{v})\, 2 r_\mathrm{v} \int_{r_\mathrm{v}}^{R_\mathrm{v}} \mathrm{d}r\, r \delta(r). \end{aligned} \tag{17}$$

The upper boundary of the first integral is now the minimum of r_v and R_v, since in general it is not guaranteed that $r_\mathrm{v} < R_\mathrm{v}$.

3. Testing

We test our mathematical model with the help of computer simulations. The focus of the first subsection below is to verify the dependence of a dipole contribution on the three void parameters R_v, r_v and δ. Next we allow for a varying density contrast δ with respect to r. Up to this point, we assume a volume limited observation. The flux limited case, including realistic number counts, is discussed in Sect. 4, where we incorporate a radio sky simulation from Wilman et al. (2008).

3.1. Structures of constant density contrast

Let us first look at constant density contrasts $\delta(r) = \delta$ inside the void area. In order to test our calculations, we construct a simple simulation. We draw a random point (with the random number generator Mersenne Twister) inside a three dimensional sphere of radius R_o, which we set to $R_\mathrm{o} = 1$ (which fixes the physical scale). The points inside this sphere are uniformly distributed.

The next step depends on whether we have an underdensity ($\delta < 0$) or an overdensity ($\delta > 0$) of radius R_v. In the first case, we keep all points which are outside the void (this represents the average density of objects, i.e. $\delta = 0$). For each point inside the void, we draw a random number between 0 and 1. If this number is bigger than $\delta + 1$ we drop this point and turn to the next one. If, on the other hand, it is smaller than $\delta + 1$, we keep it and proceed to a new point (this algorithm is simply a Monte Carlo sampling between $\delta = -1$ and $\delta = 0$).

For the case $\delta > 0$, we keep all drawn points inside the overdensity, and draw random numbers ($0 \to 1$) for points outside the overdensity. Now we drop the point only if the random number is larger than $1/(1 + \delta)$. So we create a map with the desired densities inside and outside the over-/underdense region.

In this way we will draw N points in total, which will be used to measure $\boldsymbol{d}$ via (1). Due to the fact that we can only use finite values of N, our simulation will always have a certain amount of shot noise, whereas our calculations in Sect. 2 neglected noise. In Rubart & Schwarz (2013) the influence of this shot noise on the expectation value of a linear estimator is discussed. We compare the average outcome of several simulations with

$$\tilde{d} := \sqrt{\langle \boldsymbol{d} \rangle^2 + (0.92/\sqrt{N})^2}, \tag{18}$$

where the second term inside the square root comes from the shot noise contribution. For $\langle \boldsymbol{d} \rangle$ we can use the results discussed in Sect. 2, depending on the case we are simulating.

In Table 1 we see a comparison between our analytic expectation and the simulated results, for cases where the observer is inside the void. In order to quantify the performance of the theory we estimate the error by $2|(\tilde{d} - d_\mathrm{s})/(\tilde{d} + d_\mathrm{s})|$. We see in Table 1 that this error drops as the dipole values increase. This is due to the fact that in those cases the uncertainties due to shot noise are less important. For the case of $r_\mathrm{v} = 0.1$, $R_\mathrm{v} = 0.2$ and $\delta = -0.5$ we see an unusually high error. We repeated this configuration with 20 extra simulations and found an averaged value of $d_\mathrm{s} = 0.215 \times 10^{-2}$, which is very close to $\tilde{d}$; so we are confident that this relatively large disagreement arose by chance. In all other cases we see a good agreement between the calculated values and the simulated ones. If the dipole is large, the agreement becomes remarkably good. These results confirm the

Table 1. Comparison of analytic model and simulation for an observer inside a local spherical structure ($r_\mathrm{v} < R_\mathrm{v}$) with constant density contrast δ.

r_v	R_v	δ	$\tilde{d}$ (10^{-2})	d_s (10^{-2})	Error %
0.1	0.1	−1	0.12	0.13	8, 7
0.1	0.2	−1	0.39	0.41	2, 8
0.2	0.3	−1	1.69	1.71	1, 3
0.2	0.4	−1	3.25	3.28	0, 9
0.4	0.4	−1	5.47	5.47	0, 0
0.1	0.1	−0.5	0.10	0.11	10, 1
0.1	0.2	−0.5	0.21	0.17	20, 2
0.2	0.3	−0.5	0.84	0.84	0, 2
0.2	0.4	−0.5	1.57	1.54	2, 1
0.4	0.4	−0.5	2.65	2.68	1, 3
0.1	0.1	1	0.12	0.13	5, 7
0.1	0.2	2	0.75	0.76	1, 4
0.2	0.3	4	5.92	5.89	0, 5
0.2	0.4	5	11.52	11.50	0, 1
0.4	0.4	7	24.75	24.70	0, 2

Notes. The analytically calculated dipole is denoted by $\tilde{d}$. Each simulated dipole amplitude d_s is an average of 10 simulations with $N = 10^6$ sources each; the error is defined as $2|(\tilde{d} - d_\mathrm{s})/(\tilde{d} + d_\mathrm{s})|$.

Table 2. As Table 1, but for observers sitting outside the spherical structure.

r_v	R_v	δ	$\tilde{d}$ (10^{-2})	d_s (10^{-2})	Error %
0.1	0.1	−1	0.12	0.10	18.7
0.2	0.1	−1	0.13	0.13	3.3
0.3	0.2	−1	0.74	0.73	1.7
0.4	0.2	−1	0.77	0.77	0.9
0.4	0.4	−1	5.47	5.46	0.2
0.1	0.1	−0.5	0.10	0.11	7.4
0.2	0.1	−0.5	0.10	0.09	12.9
0.3	0.2	−0.5	0.38	0.40	5.8
0.4	0.2	−0.5	0.39	0.36	8.4
0.4	0.4	−0.5	2.65	2.65	0.1
0.1	0.1	1	0.12	0.12	3.2
0.2	0.1	2	0.21	0.21	2.3
0.3	0.2	4	2.83	2.81	0.6
0.4	0.2	5	3.66	3.66	0.1
0.4	0.4	7	24.75	24.70	0.2

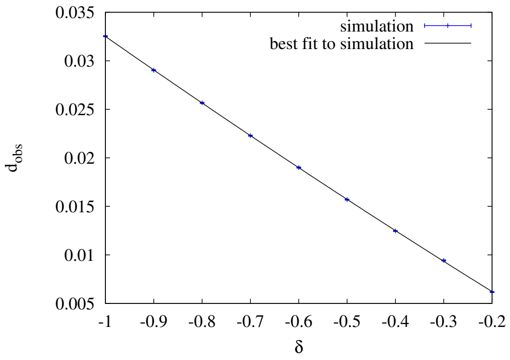

Fig. 2. Simulated dipole amplitudes. The graph is for a void with $R_\mathrm{v} = 0.4$ and $r_\mathrm{v} = 0.2$ for different values of δ, while the curve is the best fit. Each data point is the mean value of the dipole amplitude from 100 simulations with 10^6 sources each. The error bars represent the empirical variance of these simulations. For the fit a function $f(\delta) = \sqrt{\left(\delta \frac{a}{1+b\delta}\right)^2 + c^2}$ was used.

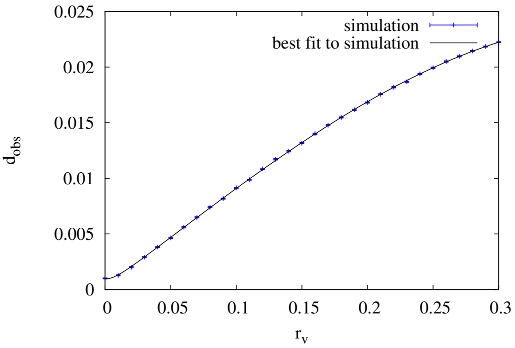

Fig. 3. Simulated dipole amplitudes. The graph is for a void with $R_\mathrm{v} = 0.3$ and $\delta = -1$ for different values of r_v. Each data point is the mean value of the dipole amplitude from 100 simulations with 10^6 sources each, while the curve is the best fit. The error bars represent the empirical variance of these simulations. For the fit, a function $g(r_\mathrm{v}) = \sqrt{(a\, r_\mathrm{v} - b\, r_\mathrm{v}^3)^2 + c^2}$ was used.

calculated expectation values of the dipole for voids with $r_\mathrm{v} \leq R_\mathrm{v}$ and constant density contrast δ.

In Table 2 we present the comparison for cases with $r_\mathrm{v} \geq R_\mathrm{v}$. Again we can see that the difference between calculation and simulation is quite small, and decreases as the dipole amplitude increases.

The simulated dipole amplitude can be plotted as a function of either r_v, R_v or δ. We present examples of simulations in Figs. 2–4, where we have fitted functions of the form (4) making use of the normalization factor (6) and including a shot noise contribution (18).

In all cases the fitted curve follows the simulated dipole amplitudes very well. The first case shows the dipole amplitude as a function of the density contrast δ; we see that the dependence on δ is approximately linear. Here we used a void of size $R_\mathrm{v} = 0.4$ and an offset distance of $r_\mathrm{v} = 0.2$; we expect from our theoretical model fit parameters of $\langle a \rangle = 0.0305$, $\langle b \rangle = 0.064$ and $\langle c \rangle = 0.92 \times 10^{-3}$. The values of our fit of $f(\delta)$ give us the parameters $a = 0.0303 \pm 0.0002$, $b = 0.066 \pm 0.005$ and $c = (0.92 \pm 0.05) \times 10^{-3}$, which are in excellent agreement.

For Fig. 3 we used 10^6 sources, a density contrast of $\delta = -1$ and a void radius of $R_\mathrm{v} = 0.3$; we expect $\langle a \rangle = 0.0925$, $\langle b \rangle = 0.206$ and $\langle c \rangle = 0.92 \times 10^{-3}$. The values of our fit of $g(r_\mathrm{v})$ give us the parameters $a = 0.0924 \pm 0.0002$, $b = 0.205 \pm 0.003$ and $c = (0.92 \pm 0.04) \times 10^{-3}$. Again, this is in very good agreement with our prediction. We can observe that the dipole increases strongly with the offset distance r_v. On the edge of the void, the increase becomes more modest.

The graph in Fig. 4 shows the behaviour of the dipole amplitude as a function of the void size R_v. Here we used a density contrast of $\delta = -0.25$ and an offset distance of $r_\mathrm{v} = 0.2$; we expect $\langle a \rangle = 0.2$, $\langle b \rangle = 0.25$ and $\langle c \rangle = 0.92 \times 10^{-3}$. The values of our fit of $h(R_\mathrm{v})$ give us the parameters $a = 0.205 \pm 0.006$, $b = 0.244 \pm 0.006$ and $c = (0.91 \pm 0.07) \times 10^{-3}$. We see that the parameters are in very good agreement with our prediction.

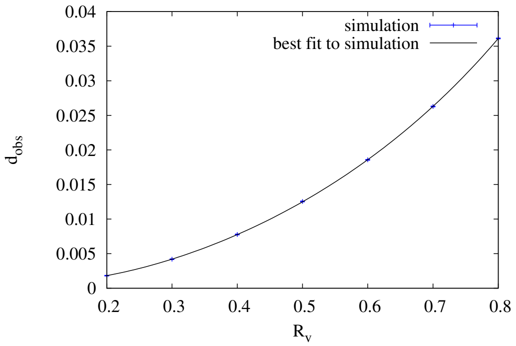

Fig. 4. Simulated dipole amplitudes. The graph is for a void with $r_\mathrm{v} = 0.2$ and $\delta = -0.25$ for different values of R_v. Each data point is the mean value of the dipole amplitude from 100 simulations with 10^6 sources each, while the curve is the best fit. The error bars represent the empirical variance of these simulations. For the fit, a function $h(R_\mathrm{v}) = \sqrt{\left(b\frac{a\,R_\mathrm{v}^2 - 0.2a^3}{1+b\,R_\mathrm{v}^3}\right)^2 + c^2}$ was used.

Table 3. Comparison for cases with offset distance r_v smaller than void radius R_v.

r_v	R_v	p	$\tilde{d}$ (10^{-2})	d_s (10^{-2})	Error %
0.2	0.4	1	0.96	0.96	0.2
0.3	0.5	1	2.16	2.18	0.7
0.2	0.4	2	1.49	1.51	1.4
0.3	0.5	2	3.42	3.44	0.4
0.2	0.4	3	1.82	1.83	0.2
0.3	0.5	3	4.24	4.25	0.2

Notes. The density contrast is of the form $\delta(r) = \frac{r^p}{R_\mathrm{v}^p} - 1$ and the calculated dipole is $\tilde{d}$. Each simulated dipole amplitude d_s is an average of 10 simulations with $N = 10^6$ sources each; the error is defined as $2|\frac{\tilde{d}-d_\mathrm{s}}{\tilde{d}+d_\mathrm{s}}|$.

We conclude from this section that formula (4) combined with (18) is in very good agreement with our simulations.

3.2. Arbitrary void profile

Now we would like to test whether formula (17) is also verified by our simulations. We consider density contrasts of the form $\delta(r) = \frac{r^p}{R_\mathrm{v}^p} - 1$ for r inside the void and $\delta(r) = 0$ outside. In all such cases the density contrast has the boundary values $\delta(0) = -1$ and $\delta(R_\mathrm{v}) = 0$. In such cases the integrals in (17) can be solved analytically. Results will be put into (18) in order to get $\tilde{d}$.

The simulation is similar to the one described in Sect. 3.1. We choose a random number for points inside the void. This time a point (with distance r from the void centre) is discarded if the random number is greater than r^p/R_v^p.

In Table 3 we see the comparison of our calculated dipole expectation with the simulation results for cases $r_\mathrm{v} < R_\mathrm{v}$, and in Table 4 for cases with $R_\mathrm{v} > r_\mathrm{v}$. Again we can observe the tendency to find improved agreement with the analytic model when the dipole amplitude is larger. In fact even for small dipole values we see a good agreement between the simulation and our calculation. Therefore we are satisfied that Eq. (17) is confirmed by our simulations.

Table 4. Comparison for cases with offset distance r_v larger than void radius R_v.

r_v	R_v	p	$\tilde{d}$ (10^{-2})	d_s (10^{-2})	Error %
0.4	0.2	1	0.21	0.21	1.9
0.5	0.3	1	0.65	0.69	4.7
0.4	0.2	2	0.32	0.31	2.8
0.5	0.3	2	1.04	1.05	1.0
0.4	0.2	3	0.40	0.42	5.1
0.5	0.3	3	1.30	1.30	0.0

Notes. The density contrast is of the form $\delta(r) = \frac{r^p}{R_\mathrm{v}^p} - 1$ and the calculated dipole is $\tilde{d}$. Each simulated dipole amplitude d_s is an average of 10 simulations with $N = 10^6$ sources each; the error is defined as $2|\frac{\tilde{d}-d_\mathrm{s}}{\tilde{d}+d_\mathrm{s}}|$.

4. Missing dipole contribution

Now we investigate the contribution which realistic void models can have on the observed radio dipole. Therefore we no longer assume a volume limited observation, but a flux limited one.

In Rubart & Schwarz (2013), a dipole amplitude $d_\mathrm{radio} = (1.8 \pm 0.6) \times 10^{-2}$ in the NVSS catalogue was reported, which is significantly above the prediction inferred from CMB measurements (Hinshaw et al. 2009) of $d_\mathrm{cmb} = (0.48 \pm 0.04) \times 10^{-2}$. Therefore we can infer a missing dipole contribution

$$\Delta\tilde{d} = \tilde{d}_\mathrm{radio} - d_\mathrm{cmb} = (1.3 \pm 0.6) \times 10^{-2}, \tag{19}$$

where the tilde indicates that the dipole amplitudes include correction factors, which are also be applied to the void dipole estimations below.

We would like to investigate whether it is possible to get a dipole contribution of this magnitude from a void model in which we are off-centre. We examine a void of the type described by Keenan et al. (2013). They report an observed void with a density contrast of about $-\frac{1}{3}$ up to redshifts of about $z = 0.07$. The influence of smaller voids, compared to Keenan et al. (2013), on the clustering dipole, was discussed e.g. by Bilicki & Chodorowski (2010).

Since we want to compare the void dipole d_void with the one derived from the NVSS catalogue, we cannot assume a constant density outside the void. The NVSS itself does not contain information about the distance of individual objects. In order to have a realistic redshift distribution, we used the semi-empirical S^3 simulation from Wilman et al. (2008) with an area of 400 square degrees. From this we obtained a catalogue of approximately 2800 radio sources with flux densities above 25 mJy at 1.4 GHz (the limit Rubart & Schwarz 2013, used for obtaining d_radio). This is now a flux limited observation, in contrast to the volume limited model in the previous section.

Now we modify our void simulation in the following way. Each data point will have a randomly chosen direction on the sky and a redshift distance chosen from the S^3 catalogue. Inside the void we will reduce the density of points in the way described in Sect. 3.1. So we are left with number counts outside the void, which are close to what is actually observed in the mean, and some density contrast $\delta(r)$ inside the void.

We would like to estimate the maximal contribution of such a void to the measured dipole amplitude. Therefore we choose

$r_v = R_v$, since this will give the biggest dipole amplitude for a void which includes the observer. As we consider r_v to be much less than the Hubble distance R_H, we can use the linear Hubble law to relate distances and redshift. The shot noise in this simulation should be suppressed, since we only want to know the pure contribution from the void (any possible shot noise is already taken into account by the error bars of $d_{\rm radio}$). So we choose the following parameters for our simulation, which uses the redshift information to infer the distance parameters: $R_v = 0.07 R_H$, $\delta = -1/3$ and $N = 10^7$. We carried out 50 runs of our simulation, and the average dipole we obtained is

$$d_{\rm void} = (0.0918 \pm 0.0023) \times 10^{-2}. \tag{20}$$

For $r_v = 0.06 R_H < R_v$ we obtained $d_{\rm void} = (0.0839 \pm 0.0026) \times 10^{-2}$. Lower values of r_v lead to lower dipole amplitudes.

Due to masking effects (incomplete sky coverage and galactic foreground) the dipole amplitude in Rubart & Schwarz (2013) was multiplied by $3/k$, where k was evaluated to be 1.34 for this case. In order to compare both dipole amplitudes, we also need to multiply $d_{\rm void}$ by this number,

$$\tilde{d}_{\rm void} = \frac{3}{k} d_{\rm void} = (0.21 \pm 0.01) \times 10^{-2}. \tag{21}$$

If we compare this $\tilde{d}_{\rm void}$ to the missing dipole Δd we can see that such a void can have a significant contribution to the observed radio dipole. When we consider the lower bound of $d_{\rm radio}$ we see that $\tilde{d}_{\rm void}$ could explain up to about a third of the missing radio dipole.

If we would like to explain the missing dipole contribution only by one void, this would need to be bigger and have a larger density contrast. One possible combination of void parameters would be $R_v = r_v = 0.11 R_H$ and $\delta = -0.6$. For this we found, with 50 simulations, an average dipole (including masking corrections, described above) of

$$\tilde{d}_{\rm void} = \frac{3}{k} d_{\rm void} = (0.72 \pm 0.01) \times 10^{-2}. \tag{22}$$

A similar result, $d = (0.69 \pm 0.01) \times 10^{-2}$, is obtained with the parameters $R_v = r_v = 0.15 R_H$ and $\delta = -1/3$. These void models are not particularly extreme. Another possibility would be to have a combination of different under- and over-densities, such as e.g. superclusters. The dipole of these different structures could add up to result in an amplitude which could potentially explain the whole missing dipole contribution.

4.1. Flux and frequency dependence

So far we only used the S^3 simulation with a lower flux density limit of 25 mJy. For future radio surveys we hope to be able to estimate the radio dipole with more sources and therefore we will need to apply a lower flux density limit. The effect of a change in this flux density limit for the dipole contribution of a void is not trivially estimated. On the one hand, a lower flux density limit means that we can see more distant sources then previously. This means that local structure becomes less important. On the other hand, a lower flux density limit will also lead to the detection of nearby galaxies, which have a low radio brightness. For those galaxies the void structure is important and we could expect an increase in the measured dipole amplitude. Both effects will vary in strength at different flux density ranges.

In order to estimate these effects, we again used the S^3 simulation from Wilman et al. (2008). We considered the two frequencies of 1.4 GHz (e.g. NVSS or a planned survey with ASKAP[1]) and 151 MHz (e.g. LOFAR[2]). A continuum survey with the SKA[3] will be likely to be collected at a frequency between these (e.g. 600 MHz). Again we used the void parameters from Keenan et al. (2013). This time we applied different flux density limits to see the dependence of the observed dipole amplitudes on the flux density limit.

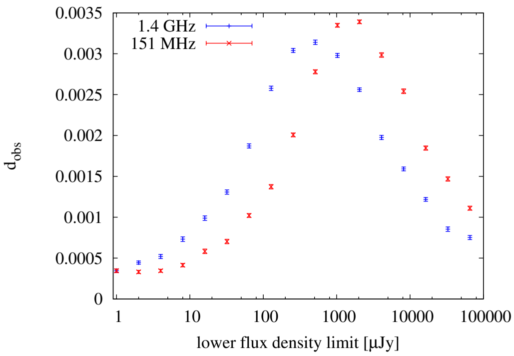

Fig. 5. Simulated dipole amplitudes for different flux limits. Each point is the average of 50 simulations with 10^7 sources each. The void used here has the parameters $R_v = r_v = 0.07 R_H$ and $\delta = -1/3$. The error bars represent the empirical variance of these simulations.

In Fig. 5 we see that the dependence of the measured dipole amplitudes from the flux density limit is quite complex. Notice that the flux limits shown cover almost five orders of magnitude. For flux density limits below 10 mJy, the dipole amplitudes increase very strongly until a maximum is reached around 1 mJy. The contribution of a local void for the dipole in a survey with a flux density limit of 1 mJy could be about three times as strong as it is for a limit of 25 mJy. This means that the effect of voids will become more important in future radio surveys. In principle it is possible to disentangle the kinetic dipole contribution from the structure dipole, since the kinetic dipole amplitude does not depend on the flux density limit (the shot noise does, but this will be taken into account by the error bars).

We can see that the general behaviour for both frequencies is the same. The main difference is in the position of the peak in the dipole amplitude. This comes from the fact that different radio source populations show up at different flux density limits for different frequencies. Due to this effect it seems possible to analyse the structure component of the radio dipole by using different frequencies and flux density limits. A kind of tomography of the local universe would be a possible application. Radio telescopes like LOFAR, ASKAP or SKA will be ideal to create the necessary radio catalogues at different frequencies for this purpose.

4.2. Line of sight dependence

It was shown by Singal (2011) that the amplitude of a linear dipole estimator (using the NVSS survey), for different areas of the sky, varies like $\cos(\theta)$, where θ is the angle measured between the line of sight and the dipole direction. This analysis is in agreement with the assumption that the radio dipole is dominated by a kinetic contribution.

---

[1] www.atnf.csiro.au/projects/askap/

[2] www.lofar.org

[3] www.skatelescope.org

We now discuss whether a radio dipole which is partly due to a contribution from a local void, would be in conflict with this observed behaviour or not. Therefore we investigate how the dipole amplitude from a void varies with respect to the angle θ (for simplicity we assume a constant density contrast inside the void here). Any prefactors, which do not depend on θ, are not relevant here.

The effect of a void-like structure on the dipole amplitude is proportional to the length of the line of sight inside the void. If we are inside the void, we need to add the forward and backward contribution, since a dipole estimator also picks up both parts. In order to find this length, we use the equation of a circle (radius R_v) with an offset of r_v in the x-direction

$$(x - r_\mathrm{v})^2 + y^2 = R_\mathrm{v}^2. \tag{23}$$

Using polar coordinates l, θ with $x = l\cos\theta, y = l\sin\theta$ we can transform this to

$$\frac{l}{R_\mathrm{v}} = \frac{r_\mathrm{v}}{R_\mathrm{v}}\cos(\theta) \pm \sqrt{\frac{r_\mathrm{v}^2}{R_\mathrm{v}^2}\cos\theta^2 + 1 - \frac{r_\mathrm{v}^2}{R_\mathrm{v}^2}}. \tag{24}$$

For the case $R_\mathrm{v} \le r_\mathrm{v}$ we subtract one solution from the other to get the distance between the two crossings of the line of sight with the void boundaries. Therefore the dipole signal is proportional to

$$f = \sqrt{\frac{r_\mathrm{v}^2}{R_\mathrm{v}^2}\cos\theta^2 + 1 - \frac{r_\mathrm{v}^2}{R_\mathrm{v}^2}}, \tag{25}$$

where f is now the fraction of the dipole effect in the direction θ, meaning $d \propto f$. For the case of an observer on the edge of the void ($r_\mathrm{v} = R_\mathrm{v}$), this simplifies to a cosine and therefore behaves exactly like a kinetic dipole.

For the case $R_\mathrm{v} \ge r_\mathrm{v}$ one solution of (24) is negative. For an observer inside the void the fraction of the dipole effect depends on the difference of the length of the line of sight in the forward and backward direction. Thus, we need to add up the two solutions of (24) and obtain

$$f = \cos\theta. \tag{26}$$

Therefore an observer inside a void sees an effect for the dipole estimation which behaves like a cosine. So we cannot distinguish this case from a kinetic dipole by its angular dependence.

In Fig. 6 we show the relation of f versus θ for different values of $r_\mathrm{v}/R_\mathrm{v}$. We see that this relation is steeper when the observer is outside the void ($r_\mathrm{v} > R_\mathrm{v}$). In future surveys, such an analysis can help to separate the kinetic dipole contribution from a structural component and also give an estimation of $r_\mathrm{v}/R_\mathrm{v}$.

The case investigated in this work is an observer living close to the edge of a void-like structure. This scenario cannot easily be distinguished from a pure kinetic dipole by this method, since both will behave like a cosine in angular dependence. Therefore the work of (Singal 2011) is not in conflict to the investigated scenario here.

5. Conclusion

We have been able to develop a model that can describe the influence of spherically symmetric local structures on linear dipole estimators. This model was tested and confirmed by computer simulations to a high level of accuracy. From this model we learn how the structure parameters (void size R_v, observer distance from the void centre r_v and void density contrast δ) influence the structure dipole amplitude.

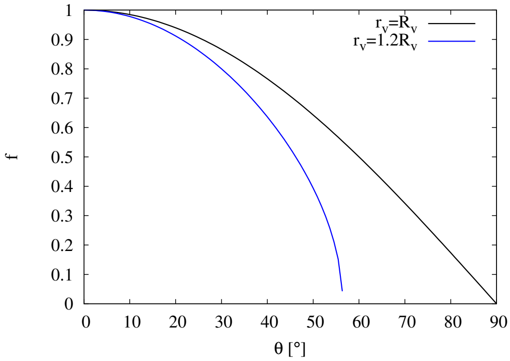

Fig. 6. Fraction of dipole effect f versus angle between dipole direction and line of sight θ for different ratios of the offset vector r_v to the void radius R_v.

Our analytical model requires a constant background density, which is a reasonable approximation at small redshifts. In order to include the effects of cosmic expansion and galaxy evolution, the dipole contribution for the realistic void model was estimated by means of simulations of the number counts of radio galaxies. Not included in this work are estimations of the dipole contribution from several galaxy clusters or other structures; because the dipole estimator is linear, these would just be a sum of terms similar to the ones calculated in this paper.

One might ask if a void as considered in this work would show up in the CMB. It is clear that the size of the effect will depend on the distance of the observer from the centre of the void. The CMB dipole will be maximally affected for an observer sitting at the edge of the void. There is no contribution to the CMB dipole if the observer sits in the centre and the effect would show up at much smaller angular scales if the observer were far away form the void. A CMB dipole would be induced by the integrated Sachs-Wolfe effect (or the Rees-Sciama effect if non-linear effects play a role) and thus the dynamics of the void profile would be important to determine its amplitude. Such structures have been studied previously, e.g. by Thompson & Vishniac (1987), Tomita (2000), Rakić et al. (2006), Inoue & Silk (2006), Maeda et al. (2011), Francis & Peacock (2010) and Rassat & Starck (2013). An order of magnitude estimate of the maximum possible effect (Panek 1992) gives

$$\Delta T/T \sim \delta^{3/2}\left(\frac{R_\mathrm{v}}{R_\mathrm{H}}\right)^3 \sim 2\times10^{-4} \tag{27}$$

for the model considered here. This shows that the void-like structure considered in this paper would not be in tension with the observed CMB dipole, but might contribute to the CMB anomalies at small multi-pole moments. A detailed study of this topic is beyond the scope of this work.

For the void model of Keenan et al. (2013) for our local environment, we have run simulations which include a radio sky model from Wilman et al. (2008). We found that such a void already has a significant effect on the dipole estimation for surveys like the NVSS. The dipole amplitude measured by the linear estimator from Rubart & Schwarz (2013) of this void is expected to be $\tilde{d}_\mathrm{void} = 0.21 \pm 0.01 \times 10^{-2}$. The discrepancy between radio and CMB dipole measurements can be relaxed by such a contribution, but the difference cannot be explained completely by the contribution from a single, realistic void. In forthcoming surveys, with lower flux density limits, the effect of local structure will become even more important.

Acknowledgements. M.R. and D.J.S. acknowledge financial support from the Friedrich Ebert Stiftung and from the Deutsche Forschungsgemeinschaft, grant RTG 1620 "Models of Gravity". D.B. is supported by UK Science and Technology Facilities Council, grant ST/K00090X/1. Please contact the authors to request access to research materials discussed in this paper.

References

Alnes, H., & Amarzguioui, M. 2006, Phys. Rev. D, 74, 103520
Alnes, H., Amarzguioui, M., & Gron, O. 2006, Phys. Rev. D, 73, 083519
Bilicki, M., & Chodorowski, M. J. 2010, MNRAS, 406, 1358
Blake, C., & Wall, J. 2002, Nature, 416, 150
Celerier, M.-N. 2000, A&A, 353, 63
Condon, J. J., Cotton, W. D., Greisen, E. W., et al. 1998, AJ, 115, 1693
Crawford, F. 2009, ApJ, 692, 887
Francis, C. L., & Peacock, J. A. 2010, MNRAS, 406, 14
Gibelyou, C., & Huterer, D. 2012, MNRAS, 427, 1994
Hinshaw, G., Weiland, J. L., Hill, R. S., et al. 2009, ApJS, 180, 225
Inoue, K. T., & Silk, J. 2006, ApJ, 648, 23
Keenan, R. C., Barger, A. J., & Cowie, L. L. 2013, ApJ, 775, 62
Kogut, A., Lineweaver, C., Smoot, G. F., et al. 1993, ApJ, 419, 1
Kothari, R., Naskar, A., Tiwari, P., Nadkarni-Ghosh, S., & Jain, P. 2013 [arXiv:1307.1947]
Maeda, K.-I., Sakai, N., & Triay, R. 2011, Cosmol. Astropart. Phys., 8, 26
Panek, M. 1992, ApJ, 388, 225
Rakić, A., Räsänen, S., & Schwarz, D. J. 2006, MNRAS, 369, L27
Rassat, A., & Starck, J.-L. 2013, A&A, 557, L1
Rubart, M., & Schwarz, D. J. 2013, A&A, 555, A117
Singal, A. K. 2011, ApJ, 742, L23
Thompson, K. L., & Vishniac, E. T. 1987, ApJ, 313, 517
Tomita, K. 2000, ApJ, 529, 26
Whitbourn, J. R., & Shanks, T. 2014, MNRAS, 437, 2146
Wilman, R. J., Miller, L., Jarvis, M. J., et al. 2008, MNRAS, 388, 1335

Chapter 6

Discussion and Outlook

> *a scientist's job is to ask questions.*
> – The Doctor, Dr. Who: City of Death

In this chapter we discuss the different results for the cosmic radio dipole, using the NVSS and the WENSS catalogues. In table 6.1 one sees the main result of the estimators used in this work as well as the results of some independent but related studies.

The dipole estimations for all methods used in this thesis (bold face in table 6.1) are in very good agreement with each other. The dipole amplitudes, estimated with the NVSS catalogue, are almost the same for the two linear and the quadratic estimators. The dipole direction obtained by the quadratic estimator differs slightly from one of the linear estimators, but since their one-sigma contours overlap, there is no tension between the results. Due to the biasing effects, concerning the linear estimators (discussed in chapter 2 and 3), we presume that the quadratic estimator result is the superior one. Additionally, the estimated error bars for the quadratic estimator are smaller in comparison.

For the WENSS catalogue we see again that the linear estimator gives a result in agreement with the quadratic one. The obtained right ascensions are almost exactly the same, while the declination can only be estimated with a quadratic estimator and hence cannot be compared. We see that the dipole amplitude is higher for the linear estimator. This can be explained to some degree by the amplitude bias, discussed in Rubart & Schwarz (2013). Due to the rather large error bars (caused mainly by the low number of total sources), the amplitudes are in no tension with each other. The directional uncertainty is also larger for this catalogue, due to the comparably low number of sources.

Source	Flux > (mJy)	N	RA (°)	dec (°)	d (10^{-2})
NVSS					
BW	25	$197,998$	158 ± 30	-4 ± 34	1.1 ± 0.3
SIF	25	$184,237$	159 ± 10	-7 ± 9	2.2 ± 0.6
3DS	**25**	$\mathbf{185,649}$	$\mathbf{158 \pm 19}$	$\mathbf{-2 \pm 19}$	$\mathbf{1.8 \pm 0.6}$
2DCG	**25**	$\mathbf{195,245}$	$\mathbf{155 \pm 14}$	...	$\mathbf{1.9 \pm 0.5}$
QE	**25**	$\mathbf{220,237}$	$\mathbf{143 \pm 12}$	$\mathbf{-11 \pm 15}$	$\mathbf{1.8 \pm 0.5}$
GH	15	$211,487$	117 ± 20	6 ± 14	2.7 ± 0.5
K e.a.	20	$\dots^{*}$	147 ± 8	-22 ± 10	1.5 ± 0.2
TJ	20	$\dots^{*}$	137 ± 8	20 ± 10	$(2.8 \pm 0.3)^{**}$
WENSS					
2DCG	**25**	$\mathbf{92,600}$	$\mathbf{117 \pm 40}$	...	$\mathbf{2.9 \pm 1.9}$
QE	**25**	$\mathbf{85,285}$	$\mathbf{118 \pm 39}$	$\mathbf{-7 \pm 24}$	$\mathbf{1.6 \pm 0.8}$
expected					
NVSS	...	...	168	-7	0.48 ± 0.04
WENSS	...	...	168	-7	0.42 ± 0.03

Table 6.1: Comparison of main results. Radio dipole from NVSS: BW (Blake & Wall 2002), SIF (Singal 2011) flux-weighted number counts, 3DS three-dimensional linear estimator, mask adopted from Singal (2011) (this work), 2DCG two-dimensional linear estimator, CG mask (this work), QE quadratic estimator (this work), GH (Gibelyou & Huterer 2012), K e.a. (Kothari et al. 2013) and TJ (Tiwari & Jain 2015) [* N was not mentioned in these studies / **due to an additional cut in polarization the amplitude obtained in this case cannot be compared directly, but is expected to be roughly 50% above the other results (see chapter 1.7).]; Radio dipole from WENSS: 2DCG two-dimensional linear estimator, CG mask (this work), QE quadratic estimator (this work). The expectations for a purely kinetic radio dipole are given at the bottom of the table.

We can nevertheless learn two important points from the analysis of the WENSS catalogue. Firstly, the results are in agreement with the dipole estimation from the NVSS. This reduces the chance of significant observational systematic errors. Secondly, with the WENSS catalogue we see a hint towards increased dipole amplitude in radio as well as a hint towards a directional offset towards smaller right ascension values. Considering only the WENSS results, those indications are not significant, due to their large uncertainties.

Comparing our NVSS-based results with related studies we find general agreement. All analysed estimators resulted in similar dipole directions and amplitudes. Differences are below two sigma, usually even below one sigma. This shows that the different estimators are consistent with each other, even so they are based on different principles. The estimator SIF (Singal 2011) is a special case, since it analyses the anisotropy in flux distribution across the sky. It was shown that the expected amplitude is the same like for the number counts.

Due to an additional cut in polarization, the TJ estimator (Tiwari & Jain 2015) gives a higher dipole amplitude. A direct comparison of amplitudes cannot be made yet, but the directional results are expected to point towards the same direction, like for the number count studies. Within the given uncertainties, this is the case. Results from GH (Gibelyou & Huterer 2012) may be a little bit different due to a) a lower flux limit and b) a different method for handling masked areas (in this case they were filled with random datapoints).

In Kothari et al. (2013) the same strategy for handling masked areas as in Gibelyou & Huterer (2012) was used, but their linear estimator is based on spherical harmonic coefficients. Also special attention was given to the number count slope. This does not affect the dipole amplitude itself, but velocity estimations based on the dipole amplitude. Even though the approaches are quite different, the discussed excess in dipole amplitude is consistent in all mentioned studies. So we have evidence for a cosmic radio dipole amplitude above the CMB expectation.

Taking a closer look at the χ^2 values of the quadratic dipole estimator revealed that the radio sky is not well described by a monopole and dipole term alone. We expect cosmic structure to play an important role in this context. A possible improvement of the quadratic estimator could be made by including higher multipoles or model the cosmic structure in a similar way and include this into the fitting algorithms. In Blake & Wall (2002) the quadro- and octopole were also fitted and local structure effects were reduced, by ignoring areas on the sky close to known nearby galaxies

(Saunders et al. 2000). Hence, the resulting dipole in Blake & Wall (2002) is consistent with our estimation, we expect both, the higher multipole fit and the local structure, to have no dominant effect. On the other hand they might be of the order of the above given uncertainties and hence could become relevant, when the shot noise can be reduced with future measurements.

Since the quadratic estimator developed in this work is already slow in terms of computational time, it would be desirable to refine our code. By utilizing parallel computation on several CPUs, a first step towards a faster code has been made in this work. Further enhancement could be achieved by an advanced search algorithm. So far we used a three-dimensional constant sized grid to find the best-fit parameters. An improvement could be to search on a rough grid first and then confine the detailed search to a smaller sector. Advanced searching techniques, like e.g. a Monte Carlo or a gradient-based algorithm, are imaginable, but need to be investigated carefully, whether obtained results are stable and reliable for this application. A faster code would allow for more complicated fitting models, like for example including a quadrupole contribution. One could also imagine fitting a catalogue with different monopole terms, depending on the survey sensitivity. The NVSS catalogue for example could be split into parts with the same configuration used. In each part the monopole may be slightly different.

For both catalogues an improved mask is possible. Removing the galactic plane was always done with a straight strip in galactic latitude. Modelling the form of the Milky Way may also allow for a smaller masking area and thereby increase the number of usable sources for the estimation. It is well know that strong radio sources do influence the observation of their direct neighbourhood on the sky, due to the limited dynamic range of telescopes. Hence, pixels including such bright sources on the sky could be masked. The effect of local structure can be investigated, by ignoring areas on the sky with known local structures. In Blake & Wall (2002) this was done for the whole analysis. The possible difference in resulting dipoles with and without areas near local extragalactic sources would be an interesting indicator for the structure dipole magnitude.

The frequency dependence of the structure contribution to the dipole can be used to distinguish it from the kinetic contribution. Especially future surveys with LOFAR or SKA will be able to provide catalogues with different frequencies bands, using the same telescope. In 2015 the release of the Multifrequency Snapshot Sky Survey [MSSS, Heald & LOFAR Collaboration (2014)] catalogue is expected, which observed at 60 MHz and 150 MHz, with 8 bands for both frequency ranges. Comparing the resulting dipoles at different frequencies and comparing those results to the NVSS dipole may reveal first insights to the contribution of structures. As discussed in section 3.2, a number count slope of $x \approx 1$ provides a kind of sweet spot, which supresses calibration effects on multipole estimations. For future measurement, one needs to keep in mind that a change in this slope parameter may affect the impact of calibration errors on the dipole estimation.

Future radio surveys will catalogue the radio sky with increased sensitivity and hence they will include a significantly higher number of radio sources. With more sources the shot noise contribution to all estimators will be reduced and thereby the uncertainties in the dipole estimations will be less. With smaller error bars we will be able to tell definitely, whether the cosmic radio dipole is in tension with the CMB dipole. If there is an additional contribution to the radio dipole, which is not seen in microwave, then it is very likely that the directions of both dipoles differ at least slightly. So far the error bars are too large to confirm such a difference. We just see a hint towards smaller right ascension for the radio dipole.

Unfortunately the direction of observed bulk flows is not known, since the kSZ effect does depend on $v_{\rm bulk}^2$ (Birkinshaw 1999). The axis however seems to coincide with the CMB dipole direction. There are two possible scenarios imaginable in the context of increased radio dipole amplitude. One is that the local universe is in coherent movement towards some very large structure. In this case the radio dipole would be increased, since it does observe the large structure as well as the kinetic movement. The second scenario is that the CMB does have an intrinsic dipole. In that case the assumed peculiar velocity of the Milky Way was incorrect. Such an error would influence the bulk flow measurement and could lead to an apparent coherent movement. So far it is not possible to confirm or reject those scenarios.

The observed Hubble expansion is sensitive to both scenarios. As discussed in section 1.3, the velocity inferred from the anisotropy in Hubble expansion found by Kalus et al. (2013) is of similar magnitude as the suspected bulk flow. Also the observed strange alignment of the quadrupole and octopole in CMB maps (Copi et al. 2013), which is in tension with the ΛCDM model, may be connected to those questions. Possibly this tension is lifted, when an intrinsic CMB dipole can be distinguished from the kinematic one. To investigate this scenario further could reveal interesting connections.

In order to resolve those speculations, a radio dipole estimation with high precision is needed. For this, future surveys will be utilized. The results presented in this thesis will be very useful, since they provide a deep understanding of different estimators. Improved measurements at other wavelengths will allow investigating the possible change of the dipole w.r.t. different cosmic distances.

Chapter 7

Conclusion

> *Eliminate all other factors, and the one which remains must be the truth.*
> – Sherlock Holmes, The Sign of Four
> by Arthur Conan Doyle

In this thesis we carefully analysed linear and quadratic dipole estimators of the cosmic radio dipole. We assumed that the radio sky can be well described by a combination of a monopole and a dipole, when the galactic plane is ignored. We assumed that radio sources, found outside the galactic plane in the NVSS or WENSS catalogue, have extragalactic origin.

The simple linear estimators do suffer from various biasing effects. Due to shot noise the obtained amplitudes are biased towards higher values. This problem can be handled by means of simulations. The masking bias in amplitude can also be handled, but not the directional one. Revealing those flaws is relevant, since most radio dipole studies utilized a linear estimator. The quadratic estimator developed during this work does not show those biasing effects, with the exception of the shot noise amplitude effect. Since this effect is understood and can be handled, the quadratic estimator is reliable for the dipole estimation and should be preferred to a linear estimator.

We found the radio dipole anisotropy in the NVSS at 1.4 GHz and were able to confirm those findings with a second radio catalogue, the WENSS at 345 MHz. In both cases the dipole direction is close (within 40°) to the CMB dipole and the amplitudes are higher by a factor of about four. This excess may be partially due to local structure. Such an effect was discussed in detail in section 5, particularly in combination with observed large local voids. In the end, the structure effect seems to be too small to explain the observed excess completely.

It is too early to settle the issue of the cosmic radio dipole finally. Future measurements, with more sources, are necessary in order to reduce shot noise. Calibration and masking effects must be taken into account and understood for future observations. The contribution of structure effects must be disentangled from the kinetic contribution. Further studies must be performed on the effect, a change in the assumed velocity of the Sun with respect to the CMB would have on other observations, like e.g. the bulk flow measurements or the anisotropy in Hubble expansion. The work presented in this thesis shows that it is important and interesting to pursue the cosmic radio dipole further.

A peculiar velocity of the Sun with respect to distant radio sources that differs significantly from the velocity obtained by the CMB measurement might reveal an intrinsic dipole anisotropy in the CMB. It is even imaginable that the radio dipole challenges the cosmological principle itself, the assumed perfect isotropy of the universe at largest scales may be in question and a deviation of this isotropy, on the per mille level, becomes imaginable.

Chapter 8

Acknowledgements

First of all, I want to thank my supervisor Dominik J. Schwarz, who guided my scientific education for over six years now. It has been a pleasure to be part of his group. I benefited greatly from all the discussions we had as well as from the various colloquia I was able to attend.

During my research visit at the ICG in Portsmouth I worked together with David Bacon and I want to thank him hereby very much for this interesting time and for all the valuable discussions we had. For helpful discussions via mail contact I want to thank Ashok Singal.

For plenty of interesting discussions and a very friendly working environment, I want to thank all the students and postdocs that I was able to get to know during my time as part of the cosmology group. Special thanks goes to Song for proofreading this thesis and Anne-Sophie for help with Healpy and the generation of maps of the NVSS and WENSS number counts. I also like to thank Susi and Gudrun for being the best secretaries possible.

I acknowledge financial support from Deutsche Forschungsgemeinschaft (DFG) under grants IRTG 881 'Quantum Fields and Strongly Interacting Matter' and RTG 1620 'Models of Gravity', as well as from the Friedrich Ebert Stiftung (FES). The grand by the FES also enabled me to visit the Institute of Cosmology and Gravitation (ICG) in Portsmouth.

This research has made use of NED, gnuplot, Kile, openMP, ubuntu as well as the Healpy and HEALPix (Górski et al. 2005) packages. I thank the WENSS team (http://www.astron.nl/wow/testcode.php) and the NVSS team (http://www.cv.nrao.edu/nvss/) for providing the corresponding radio catalogues.

Further gratitude goes towards my friends in and outside of the university, for providing me such a great time in the past years. Finally, I want to

thank my parents, who supported me during my whole educational time, from primary to graduate school. Without their constant encouragement I would never have been able to do my Ph.D.

Chapter 9

Appendix

Here, the main computer program segments used during the preparation of this thesis are presented. In each section, a short description of the purpose of the corresponding code is given. All code segments were used in a variation of different contexts, often combined with each other. For example the simulation code can be combined with the various estimators in order to test the estimators with simulated data. The codes can be run within other programs to estimate e.g. mean results of a large number of runs and/or the corresponding variance of those runs.

For convenience, the programs work in the spherical coordinate system instead of an equatorial one. This means $\varphi = \mathrm{RA}$ and $\vartheta = 90° - \mathrm{dec}$. Since the imported maps and simulations are usually using degrees, a conversion towards radian is necessary.

9.1 Functions

The following code represent the "anglecal.h" header file which is used in most of the later presented codes. It was designed for Rubart (2012) and remained useful for later projects.

```
#include <math.h>
#include <stdio.h>
#include <stdlib.h>


 const double torad = 0.017453292;
 const double todeg = 57.29577951;
 const double c = 299792.458 ; //km pro sec
```

```
//This function will calculate the angle between two
   positions on the sky given in spherical
   coordinates.
float anglebetween(float phi1,float theta1,float phi2
   ,float theta2)
{
    float beta=0;

    beta=todeg*acos(sin(theta1*torad)*cos(phi1*torad)
       *sin(theta2*torad)*cos(phi2*torad)+sin(theta1*
       torad)*sin(phi1*torad)*sin(theta2*torad)*sin(
       phi2*torad)+cos(theta1*torad)*cos(theta2*torad
       ));

    return(beta);
}

// This function will calculate the delta factor,
   which transforms the flux in rest frame to the
   flux in the observers frame
float delta(float theta, float v)

{
    float delta=0;

    delta=(1+(v/c)*cos(theta*torad))/(sqrt(1-pow((v/c
       ),2)));

    return(delta);
}

// This functions calculates the angle between a
   source and the dipole direction after the
   transformation to the observers frame has been
   applied
```

```
double newbeta(float theta,float v)
{
    float theta2=0;

    theta2=todeg*atan((sin(theta*torad)*sqrt(1-pow((v
       /c),2)))/((v/c)+cos(theta*torad)));
    if(theta2<0)
    {
        theta2= theta2+180;
    }


    return(theta2);
}
```

9.2 3DLinear

A precursor of the following code was used in Rubart (2012). It reads in a file containig a list of radio sources and creates an output file, in which the results are written. The form of the mask must be either inserted manually or can be coded in a priori. Only sources fulfilling certain criteria (i.e. being outside the mask and above the flux limit) are taken into account. This code does include an error estimation of the obtained results (Rubart & Schwarz 2013). In order to minimize numerical inaccuracies, the vector is summed in blocks of $10,000$ sources.

```
 // Reading the Data File
do
{
    fin = fopen(fin_name, "r");
    do
    {
            fscanf(fin,"%c",&dummy);
    }
    while(dummy!='\n');
    s=0;
    do
```

```
{

    fscanf(fin,"%f \t %f \t %f  \t %f \t %f \t %f
         \t %f \t %f",&phi,&newphi,&theta,&
        newtheta,&dummy1,&dummy2,&Flux,&newFlux);
    //Calculating the distance of the source to
        the galactic (b) and counter galactic (b2)
         planes.
    b=Todeg*asin(sin(Torad*deltaG)*sin(Torad*(90-
        newtheta))+cos(Torad*deltaG)*cos(Torad
        *(90-newtheta))*cos(Torad*(newphi-alphaG))
        );
    b2=Todeg*asin(sin(Torad*deltaG)*sin(Torad
        *(90-newtheta))+cos(Torad*deltaG)*cos(
        Torad*(90-newtheta))*cos(Torad*(newphi
        +180-alphaG)));
    if(b<0)
    {
    b=-1*b;
    }
    if(b2<0)
    {
    b2=-1*b2;
    }
    if(choiceb2==0)
    {
    b2=100;
    }

    if(m<10000)
    {
        // Adding source position to the sum, if
            masking and source limit criteria are
            fulfilled
        if(newFlux>=FluxLimit[j] && newtheta<=
            SDecLimit && b>=blimit && newtheta>=
            NDecLimit && b2>=blimit && newFlux<=(
```

```
        float)UFluxLimit)
    {
         VecSumX[s]+=  sin(newtheta*Torad)*cos(
             newphi*Torad);
         VecSumY[s]+=  sin(newtheta*Torad)*sin(
             newphi*Torad);
         VecSumZ[s]+=  cos(newtheta*Torad);
         i++;
         m++;
    }
}
else
{
    m=0;
    VecSumX[s+1]+=VecSumX[s];
    VecSumY[s+1]+=VecSumY[s];
    VecSumX[s]=0;
    VecSumY[s]=0;
    VecSumZ[s+1]+=VecSumZ[s];
    VecSumZ[s]=0;
    if(newFlux>=FluxLimit[j] && newtheta<=
        SDecLimit && b>=blimit && newtheta>=
        NDecLimit && b2>=blimit && newFlux<= (
        float)UFluxLimit)
    {
         VecSumX[s]+=  sin(newtheta*Torad)*cos(
             newphi*Torad);
         VecSumY[s]+=  sin(newtheta*Torad)*sin(
             newphi*Torad);
         VecSumZ[s]+=  cos(newtheta*Torad);
         i++;
    }

}

    do
    {
```

```
                fscanf(fin,"%c",&dummy);
            }
            while(dummy!='\n');

    }
    while(!feof(fin));
    if(m!=0)
    {
        VecSumX[s+1]+=VecSumX[s];
        VecSumY[s+1]+=VecSumY[s];
        VecSumZ[s+1]+=VecSumZ[s];
    }
    VecX[j]=VecSumX[s+1];
    VecY[j]=VecSumY[s+1];
    VecZ[j]=VecSumZ[s+1];
    nMax=i;
    i=0;
    fclose(fin);
    //Now the evaluation of the sum starts
            VecR[j]=sqrt(VecX[j]*VecX[j]+VecY[j]*VecY
               [j]+VecZ[j]*VecZ[j]);
            Vecphi[j]=atan(VecY[j]/VecX[j])*Todeg;
                VecTheta[j] = acos(VecZ[j]/VecR[j])*
                   Todeg;
                VecTheta[j]=90.0-VecTheta[j];
            if(VecY[j]<0 && VecX[j]>0)
            {
                Vecphi[j]+=360;
            }
            else if(VecY[j]>0 && VecX[j]<0)
            {
                Vecphi[j]=180+Vecphi[j];
            }
            else if(VecY[j]<0 && VecX[j]<0)
            {
                Vecphi[j]=180+Vecphi[j];
            }
```

```
            l=1;

            //Now the error estimation starts
            do
            {
            if(VecR[j]>=sqrt(2.0*nMax*log(1/(1-sigma[
               l]))/3.0 ))
            {
                error[l]=asin(sqrt(2.0*nMax*log(1/(1-
                   sigma[l]))/3.0 )/VecR[j])*Todeg ;
            }
            else
            {
                error[l]=666;
            }
            l++;
            }
            while(l<maxsigma);
// Output of results:
 fprintf(fout," %.0f  & $ %.1f $ & $ %.1f $ & $ %.0f
    $ & $ %.1f $ & $ %.1f $ & $ %.1f $ & $ %i $ & $
    %.4f $ \\\\ \n  ",FluxLimit[j],Vecphi[j],VecTheta
    [j],VecR[j],error[1],error[2],error[3],nMax
    ,((300*VecR[j])/((float)nMax)));// This 300
    (3*100) is the pure correction for the estimator
    without any masking. The factor 100 ist in order
    to give A_vel * 10^2

            j++;

}
 while(j<=nFlux);
 fclose(fout);
    return(0);}
```

9.3 2DLinear

This code is analogous to the previous one, but estimates the dipole direction only in two dimensions.

```
// Reading the Data File
do
{
    fin = fopen(fin_name, "r");
    do
    {
            fscanf(fin,"%c",&dummy);
    }
    while(dummy!='\n');
    s=0;
    do
    {
        fscanf(fin,"%f \t %f \t %f  \t %f \t %f \t %f
             \t %f \t %f",&phi,&newphi,&theta,&
            newtheta,&dummy1,&dummy2,&Flux,&newFlux);
        //Calculating the distance of the source to
            the galactic (b) and counter galactic (b2)
             planes.
        b=Todeg*asin(sin(Torad*deltaG)*sin(Torad*(90-
            newtheta))+cos(Torad*deltaG)*cos(Torad
            *(90-newtheta))*cos(Torad*(newphi-alphaG))
            );
        b2=Todeg*asin(sin(Torad*deltaG)*sin(Torad
            *(90-newtheta))+cos(Torad*deltaG)*cos(
            Torad*(90-newtheta))*cos(Torad*(newphi
            +180-alphaG)));

        if(b<0)
        {
        b=-1*b;
        }
        if(b2<0)
```

```
{
b2=-1*b2;
}
if(choiceb2==0)
{
b2=100;
}

if(m<10000)
{
// Adding source position to the sum, if masking and source limit criteria are fulfilled
    if(newFlux>=FluxLimit[j] && newtheta<=SDecLimit && b>=blimit && newtheta>=NDecLimit && b2>=blimit && newFlux<=(float)UFluxLimit)
    {
         VecSumX[s]+= sin(newtheta*Torad)*cos(newphi*Torad);
         VecSumY[s]+= sin(newtheta*Torad)*sin(newphi*Torad);
         i++;
        m++;
    }
}
else
{
    m=0;
    VecSumX[s+1]+=VecSumX[s];
    VecSumY[s+1]+=VecSumY[s];
    VecSumX[s]=0;
    VecSumY[s]=0;
    if(newFlux>=FluxLimit[j] && newtheta<=SDecLimit && b>=blimit && newtheta>=NDecLimit && b2>=blimit && newFlux<= (float)UFluxLimit)
```

```
        {
            VecSumX[s]+= sin(newtheta*Torad)*cos(
               newphi*Torad);
            VecSumY[s]+= sin(newtheta*Torad)*sin(
               newphi*Torad);
            i++;
        }

    }

        do
        {
            fscanf(fin,"%c",&dummy);
        }
        while(dummy!='\n');

}
while(!feof(fin));
if(m!=0)
{
    VecSumX[s+1]+=VecSumX[s];
    VecSumY[s+1]+=VecSumY[s];
}
VecX[j]=VecSumX[s+1];
VecY[j]=VecSumY[s+1];
nMax=i;
i=0;
fclose(fin);
         //Now the evaluation of the sum starts
        VecR[j]=sqrt(VecX[j]*VecX[j]+VecY[j]*VecY
           [j]);
        Vecphi[j]=atan(VecY[j]/VecX[j])*Todeg;
        if(VecY[j]<0 && VecX[j]>0)
        {
            Vecphi[j]+=360;
        }
        else if(VecY[j]>0 && VecX[j]<0)
```

```
            {
                Vecphi[j]=180+Vecphi[j];
            }
            else if(VecY[j]<0 && VecX[j]<0)
            {
                Vecphi[j]=180+Vecphi[j];
            }
            l=1;
             //Now the error estimation starts
            do
            {
            if(VecR[j]>=sqrt(2.0*nMax*log(1/(1-sigma[
               l]))/3.0  ))
            {
                error[l]=asin(sqrt(2.0*nMax*log(1/(1-
                   sigma[l]))/3.0  )/VecR[j])*Todeg  ;
            }
            else
            {
                error[l]=666;
            }
            l++;
            }
            while(l<maxsigma);
// Output of results
 fprintf(fout," %.0f  & $ %.1f $ & $ %.0f $ & $ %.1f
    $ & $ %.1f $ & $ %.1f $ & $ %i $ & $ %.4f $ \\\\
    \n  ",FluxLimit[j],Vecphi[j],VecR[j],error[1],
    error[2],error[3],nMax,((300*VecR[j])/((float)
    nMax))); // This 300 (3*100) is the pure
    correction for the estimator without any masking.
     The factor 100 ist in order to give A_vel * 10^2
            j++;

}
 while(j<=nFlux);
 fclose(fout);
```

```
return(0);}
```

9.4 Simulation

In various occasions during this work simulated radio maps were used. Therefore the random number generator "MersenneTwister" was implemented. The derivation of the used equations is shown in Rubart & Schwarz (2013). The following code can be used in combination with an estimator or to create stand-alone files containing simulated radio maps, which cotain a kinetic dipole anisotropy. The number counts are modelled as a perfect power law with slope x here, but could also be imported from an outside source, like e.g. the simulation from Wilman et al. (2008).

```
// Drawing a random source
alpha = mtrand1()*360;
Delta = Todeg*acos(1-2*mtrand1());   // 90-acos(2*
    mtrand1()-1)*180/M_PI;
a = mtrand1();
Flux = lFlimit*pow((1-a),x);
    // Simulating the dipole signal
    beta=anglebetween(alpha,Delta,Dipolephi,
        Dipoletheta);
    gamma=delta(beta,velocity);
    beta2=newbeta(beta,velocity);
    newFlux=Flux*pow(gamma,(1+SI));
    t=sin((beta-beta2)*Torad)/(sin((beta-beta2)*Torad
        )+sin(beta2*Torad));
    r=sqrt(1-2*t+2*pow(t,2)+2*(1-t)*t*cos(beta*Torad)
        );
    newdelta=Todeg*acos((cos(Delta*Torad)*(1-t)+t*cos
        (Dipoletheta*Torad))/r);
    z=(sin(Delta*Torad)*sin(alpha*Torad)*(1-t)+t*sin(
        Dipoletheta*Torad)*sin(Dipolephi*Torad))/(r*
        sin(newdelta*Torad));
            if(abs(z)<1.0)
            {
```

```
            if((sin(Delta*Torad)*cos(
                alpha*Torad)*(1-t)+t*sin(
                Dipoletheta*Torad)*cos(
                Dipolephi*torad))>0)
            {
            newalpha=Todeg*asin(z);
            if(newalpha<0)
            {
            newalpha+=360;
            }
            }
            else
            {
        newalpha=-1*Todeg*asin(z)+180;
            }
}
else
{
            if(z<0)
            {
        newalpha=270.0;
            }
            else
            {
        newalpha=90.0;
            }
    }
```

9.5 Masking

As discussed in Rubart & Schwarz (2013), the linear estimators do have an amplitude bias due to masking. This can be corrected for, utilizing the following code. The basic idea is to simulate a radio map with a certain implemented dipole. This map will be used for estimating the dipole with and without a mask. The proportion of both results can be used as the estimation of the bias factor k. With this code it is possible to mask areas with declinations above NDecLimit and below SDecLimit. All sources within blimit of the galactic plane or the counter galactic plane (if choise b2=1 was made) are masked too.

```
//Calculating the distance of the source to the
    galactic (b) and counter galactic (b2) planes.
b=Todeg*asin(sin(Torad*deltaG)*sin(Torad*(ninty-
    newdelta))+cos(Torad*deltaG)*cos(Torad*(ninty-
    newdelta))*cos(Torad*(newalpha-alphaG)));
b2=Todeg*asin(sin(Torad*deltaG)*sin(Torad*(ninty-
    newdelta))+cos(Torad*deltaG)*cos(Torad*(ninty-
    newdelta))*cos(Torad*(newalpha+ninty+ninty-alphaG)
    ));
                    if(b<0)
                    {
                    b=-1*b;
                    }
                    if(b2<0)
                    {
                    b2=-1*b2;
                    }
                    if(choiceb2==0)
                    {
                    b2=100;
                    }
     if(newFlux>=FluxLimit && newdelta<=SDecLimit &&
         newdelta>=NDecLimit && b>=bLimit && b2>=bLimit
         )
     {
          VecX+= sin(newdelta*Torad)*cos(newalpha*Torad
              );
          VecY+= sin(newdelta*Torad)*sin(newalpha*Torad
              );
          VecZ+= cos(newdelta*Torad);
          F++;
     }
     if(newFlux>=FluxLimit && f<NF)
```

```
    {
        VecX2+= sin(newdelta*Torad)*cos(newalpha*
            Torad);
        VecY2+= sin(newdelta*Torad)*sin(newalpha*
            Torad);
        VecZ2+= cos(newdelta*Torad);
        f++;
    }

  }
  while(F<NF);
        F=0;
    f=0;
// Evaluating the sum and saving each result

            VecR[c]=sqrt(VecX*VecX+VecY*VecY+VecZ*
                VecZ);
                VecR[c]=VecR[c]/(float)NF;
                MeanA+=VecR[c];
        //      MeannMax+=(float)nMax;
                VecR2[c]=sqrt(VecX2*VecX2+VecY2*VecY2
                    +VecZ2*VecZ2);
                VecR2[c]=VecR2[c]/(float)NF;
                MeanA2+=VecR2[c];
        //      MeannMax2+=(float)nMax;
        //      fprintf(fout,"%i \t %f \n",Nnow,VecR[
            c]);
            printf("%i \t bei %i \n",c,NF);
                c++;

        }
while(c<NR);

// Calculating the Mean Amplitude Results

                MeanA=MeanA/(float)(NR+1);
                MeanA2=MeanA2/(float)(NR+1);
```

```
        //       MeannMax=MeannMax/(float)(NR+1);
// Output
        fprintf(fout,"Full Sky results:   %f \n",
           MeanA2);
        fprintf(fout,"Masked Sky results:  %f \n",
           MeanA);
        fprintf(fout,"Masking values: South Dec %f,
           North Dec %f, b= %f,  \n Number of Runs: %
           i and Number of sources: %i",SDecLimit,
           NDecLimit,bLimit,NR,NF);
```

9.6 Calibration

In section 3.2 the effect of calibration errors on linear estimator was discussed. The results in that section are based simulations including the following code. At the start a simulated map must be created or imported. This code includes different version of the declination depends of the calibration error.

```
        mue=newFlux;  // Change this for systematic
           bias

        u1 = sqrt(-2*log(mtrand1()));
        u2 = 2*M_PI*mtrand1();
        u3 = u1*cos(u2);  // This is standart normal
           distributed random number

        //newFlux2 = sigma*u3*newFlux+mue;    // for
           isotropic case !!
        newFlux2 = (sigma/(cos((newdelta-60)*Torad)))
           *u3*newFlux+mue;    //For cosine depending
           case, simple version
        // Following for cosine depending case with
           changing sensitivity
```

```
        //n=(int)log(cos((newdelta-30)*Torad))/log(
           change);
        //newFlux2 = (sigma/(cos((newdelta-30)*Torad)
           *cos((newdelta-30)*Torad))-n*sigma*(1.0/(
           change*change)-1.0))*u3*newFlux+mue;  //
           for Testing so far only  sigma = sqrt(
           sigma_1 + sigma_2/cos(delta -
           delta_telescope)^2),  Be aware of lower
           flux limit now with 3 sigma may not be
           enough.

        // Continue with normal estimation now
        // Measuring the dipole with and without
           calibration error for comparison possible

}
```

9.7 Chisquare

The following header file is used for the latter presented quadratic estimtor. The sum in this code is calculated parallized with OpenMP, a open multi core parallisation code. In this way more than one CPU can be utilized, reducing the needed computational time.

```
#include <iostream>
#include <omp.h>
#include <math.h>
#include <vector>


float Chisquare(std::vector<double>* Data, float
   Phi_d, float Theta_d, float Ampli_d, float N_0) {

        float result, sum, deltaG, alphaG;
        float S_d, s_d, C_d, c_d;
        bool firstinthread = true;
        sum=0;
```

```
        S_d=sin(Theta_d);
        s_d=sin(Phi_d);
        C_d=cos(Theta_d);
        c_d=cos(Phi_d);

        // Data[2] und Data[1] contain the positions!
        #pragma omp parallel for firstprivate(
            firstinthread) reduction(+:sum)   // The
            code for startung the sum on multiple
            cores
        for (int i=0; i<Data[0].size(); i++) {

                float N_model=N_0*(1+Ampli_d*(sin(
                    Data[2][i])*cos(Data[1][i])*S_d*
                    c_d+sin(Data[2][i])*sin(Data[1][i
                    ])*S_d*s_d+cos(Data[2][i])*C_d));

                sum+=pow((Data[0][i]-N_model),2)/
                    N_model;
        };

        result=sum;///(float)(Data[0].size()-1);
        return result;
}
```

9.8 Quadratic

The quadratic estimators discussed in chapter 4 are based on the following code. Imported file must be a map pixelized by HEALPIx. The flux limit must have been applied before pixelisation allready. Also a file containing the positions that should be tested must be imported.

```
 // Reading the Position Data File
        fNside = fopen(fNside_name, "r");
        fout=fopen(fout_name,"w");
                do
    {
```

```
        fscanf(fNside,"%f, %f \n",&theta,&phi);
        //printf("%f %f %i \n", phi*Todeg, theta*
           Todeg,Position[0].size());
        Position[0].push_back(theta);
        Position[1].push_back(phi);
        }
    while(!feof(fNside));
        fclose(fNside);
        fin=fopen(fin_name,"r");
        do
    {
        fscanf(fin,"%f %f %f \n",&theta,&phi,&N);
//      printf("%f %f %f \n", phi, theta, N);

        DataTMP[0].push_back(N);
        DataTMP[1].push_back(phi);
        DataTMP[2].push_back(theta);

        }
    while(!feof(fin));
fclose(fin);

std::cout << "Number of Pixel before Masking: " <<
   DataTMP[0].size() << " " << DataTMP[1].size() << "
    " << DataTMP[2].size() << " And Number of
   Positions to test is " << Position[0].size() << '\
   n';

for (int i=0; i<DataTMP[0].size(); i++) {
        // Calculate distances to galactic and
           counter galactic plane
        b=asin(sin(deltaG)*sin(M_PI/2.0-DataTMP[2][i
           ])+cos(deltaG)*cos(M_PI/2.0-DataTMP[2][i])
           *cos((DataTMP[1][i]-alphaG)));
        b2=asin(sin(deltaG)*sin((M_PI/2.0-DataTMP[2][
           i]))+cos(deltaG)*cos((M_PI/2.0-DataTMP[2][
           i]))*cos(DataTMP[1][i]+M_PI-alphaG));
```

```
if(b<0)
{
b=-1*b;
}
if(b2<0)
{
b2=-1*b2;
}
if(choiceb2==0)
{
b2=100;
}
// Only saving data points outside the mask
if(DataTMP[2][i]<=SDecLimit && b>=blimit &&
   DataTMP[2][i]>=NDecLimit && b2>=blimit)
        {
        Data[0].push_back(DataTMP[0][i]);
        Data[1].push_back(DataTMP[1][i]);
        Data[2].push_back(DataTMP[2][i]);
        }
}

std::cout << "Number of Pixel after Masking:
   " << Data[0].size() << " " << Data[1].size
   () << " " << Data[2].size() << '\n';

for (int i=0; i<Data[0].size(); i++) {
        //Data[1][i]*=M_PI/180;
        //Data[2][i]*=M_PI/180;

        total+=Data[0][i];

}

mean = total/(float)Data[0].size();
```

```
Nstart = 0.995*mean;
Nend = 1.005*mean;
// This can be changed for finer or less fine
     grids
Nstep = (Nend-Nstart)/(float)(2*PrecisionN);
   // PrecisionN determines number of tested
   Mean values
Minimum=Chisquare(Data,0,0,0.5,10); //
   starting value
std::cout<< "File Number:" <<File << '\n';

//Testing Models on a grid starts
for(float N_0=Nstart; N_0<Nend; N_0+=Nstep){

for (float d=0; d<0.05; d+=0.002){

for (float i=0; i<Position[0].size(); i+=1){

        Sum=Chisquare(Data,Position[1][i],
            Position[0][i],d,N_0);
        //        std::cout << "current
            Chisquare is " << Sum << " at Phi=
             " << i << " and Theta= " << j <<
            '\n';
        if(Sum<Minimum){
        Minimum=Sum;
        M_Phi=Position[1][i]*Todeg;
        M_Theta=Position[0][i]*Todeg;
        M_d=d;
        M_N_0=N_0;
        //std::cout << "current Minimum is "
            << Sum << " with mean N of " <<
            M_N_0 << " at Position Phi= " <<
            M_Phi << " , Theta= " << M_Theta
            << " and a Dipole Amplitude of "
            << M_d << '\n';
        }
```

```
                }
                }
        }
// After this the best fit is determined and will be
   displayed
std::cout << Minimum << " with mean N of " << M_N_0
   << " at Position Phi= " << M_Phi << " , Theta= "
   << M_Theta << " and a Dipole Amplitude of " << M_d
    << " for " << total << " sources" <<'\n';
// Results may also be saved in a File
```

9.9 Local Structure Dipole

In Rubart et al. (2014) we simulated the dipole contribution from local structures. The following code was used to create those maps, which then were tested using the linear estimators. One can choose between creating an underdense or overdense structure of arbirtray size.

```
do
  {
  Rbin=0;
  if(Density<=1.0)   // For an underdensity
  {
  do
        {
        Phi=360*mtrand1();
        Theta = Todeg*acos(1-2*mtrand1());
        fscanf(fin,"%f %f \n",&flux,&distance); //
           flux and distance to observer is imported
                if(feof(fin))
                {
                fclose(fin);
                fin = fopen(fin_name, "r");
                }
        RX=distance*cos(Torad*Phi)*sin(Torad*Theta);
        RY=distance*sin(Torad*Phi)*sin(Torad*Theta);
```

```
        RZ=distance*cos(Torad*Theta);
        D_x=RX-Offset*sin(Dipoletheta*Torad)*cos((
            Dipolephi+180)*Torad);
        D_y=RY-Offset*sin(Dipoletheta*Torad)*sin((
            Dipolephi+180)*Torad);
        D_z=RZ+Offset*cos(Dipoletheta*Torad);
        D_lum=sqrt(D_x*D_x+D_y*D_y+D_z*D_z); //
            Distance to the structure centre
                if(D_lum<Void)
                {
                        bias=mtrand1();
                        //Density=(radius*radius*
                            radius)/(Void*Void*Void);
                            // For not constant
                            densities, implemented
                            function here
                                if(bias<Density)
                                {
                                Rbin=1;
                                }
                }
                else
                {
                Rbin=1;
                }
                if(flux<(float)FluxLimit)
                {
                Rbin=0;
                }
        }
        while(Rbin==0);
}
else // for an overdensity
{
        do
        {
        Phi=360*mtrand1();
```

```
 Theta = Todeg*acos(1-2*mtrand1());
 fscanf(fin,"%f %f \n",&flux,&distance);
         if(feof(fin))
         {
         fclose(fin);
         fin = fopen(fin_name, "r");
         }
RX=distance*cos(Torad*Phi)*sin(Torad*Theta);
RY=distance*sin(Torad*Phi)*sin(Torad*Theta);
RZ=distance*cos(Torad*Theta);
D_x=RX-Offset*sin(Dipoletheta*Torad)*cos((
    Dipolephi+180)*Torad);
D_y=RY-Offset*sin(Dipoletheta*Torad)*sin((
    Dipolephi+180)*Torad);
D_z=RZ+Offset*cos(Dipoletheta*Torad);
D_lum=sqrt(D_x*D_x+D_y*D_y+D_z*D_z); //
    Abstand zum Void Zentrum
         if(D_lum>Void)
         {
                 bias=mtrand1();
                 //Density=(radius*radius*
                    radius)/(Void*Void*Void);
                    // For not constant
                    densities, implemented
                    function here
                 if(bias<1.0/Density)
                   {
                   Rbin=1;
                   }
         }
         else
         {
         Rbin=1;
         }
         if(flux<(float)FluxLimit)
         {
         Rbin=0;
```

```
                        }
            }
while(Rbin==0);
}

newdelta=Theta;
newalpha=Phi;
// now the normal estimation can start
```

Bibliography

Ahn, C. P., Alexandroff, R., Allende Prieto, C., et al. 2014, The Tenth Data Release of the Sloan Digital Sky Survey: First Spectroscopic Data from the SDSS-III Apache Point Observatory Galactic Evolution Experiment, Astrophysical Journal, Supplement, 211, 17

Atrio-Barandela, F., Kashlinsky, A., Ebeling, H., Fixsen, D. J., & Kocevski, D. 2014, Probing the Dark Flow signal in WMAP 9 yr and PLANCK cosmic microwave background maps, ArXiv e-prints

Baleisis, A., Lahav, O., Loan, A. J., & Wall, J. V. 1998, Searching for large-scale structure in deep radio surveys, Monthly Notices of the RAS, 297, 545

Bennett, C. L., Banday, A. J., Gorski, K. M., et al. 1996, Four-Year COBE DMR Cosmic Microwave Background Observations: Maps and Basic Results, Astrophysical Journal, Letters, 464, L1

Birkinshaw, M. 1999, in American Institute of Physics Conference Series, Vol. 476, 3K cosmology, ed. L. Maiani, F. Melchiorri, & N. Vittorio, 298–309

Blake, C. & Wall, J. 2002, Detection of the velocity dipole in the radio galaxies of the nrao vla sky survey, Nature, 416, 150

Braude, S. Y., Lebedeva, O. M., Megn, A. V., Ryabov, B. P., & Zhouck, I. N. 1969, The spectra of discrete radio sources at decametric wavelengths-I, Monthly Notices of the RAS, 143, 289

Braun, R., Bourke, T., & Green, J. W. 2014, SKA1 Science Priority Outcomes, http://astronomers.skatelescope.org/wp-content/uploads/2014/09/SKA-SCI-PRI-002-AppendixA.pdf

Burke, B. & Graham-Smith, F. 2010, An introduction to radio astronomy (Cambridge University Press)

Condon, J. J., Broderick, J. J., & Seielstad, G. A. 1989, A 4.85 GHz sky survey. I - Maps covering delta between 0 and + 75 deg, Astronomical Journal, 97, 1064

Condon, J. J., Cotton, W. D., Greisen, E. W., et al. 1998, The NRAO VLA Sky Survey, Astronomical Journal, 115, 1693

Condon, J. J., Griffith, M. R., & Wright, A. E. 1993, The Parkes-MIT-NRAO surveys. IV - Maps for the Southern Survey covering delta in the range -88 to -37 deg, Astronomical Journal, 106, 1095

Conklin, E. K. 1969, Velocity of the Earth with Respect to the Cosmic Background Radiation, Nature, 222, 971

Copi, C. J., Huterer, D., Schwarz, D. J., & Starkman, G. D. 2013, Large-scale alignments from WMAP and Planck, ArXiv e-prints

Courteau, S. & van den Bergh, S. 1999, The Solar Motion Relative to the Local Group, Astronomical Journal, 118, 337

Crawford, F. 2009, Detecting the Cosmic Dipole Anisotropy in Large-Scale Radio Surveys, Astrophysical Journal, 692, 887

Einasto, M., Tago, E., Jaaniste, J., Einasto, J., & Andernach, H. 1997, The supercluster-void network I. The supercluster catalogue and large-scale distribution, Astronomy and Astrophysics, Supplement, 123, 119

Ellis, G. F. R. & Baldwin, J. E. 1984, On the expected anisotropy of radio source counts, Monthly Notices of the RAS, 206, 377

Fanaroff, B. L. & Riley, J. M. 1974, The morphology of extragalactic radio sources of high and low luminosity, Monthly Notices of the RAS, 167, 31P

Fixsen, D. J., Cheng, E. S., Gales, J. M., et al. 1996, The Cosmic Microwave Background Spectrum from the Full COBE FIRAS Data Set, Astrophysical Journal, 473, 576

Fixsen, D. J. & Kashlinsky, A. 2011, Probing the Universe's Tilt with the Cosmic Infrared Background Dipole, Astrophysical Journal, 734, 61

Freedman, W. L., Madore, B. F., Gibson, B. K., et al. 2001, Final Results from the Hubble Space Telescope Key Project to Measure the Hubble Constant, Astrophysical Journal, 553, 47

Gibelyou, C. & Huterer, D. 2012, Dipoles in the sky, Monthly Notices of the RAS, 427, 1994

Górski, K. M., Hivon, E., Banday, A. J., et al. 2005, HEALPix: A Framework for High-Resolution Discretization and Fast Analysis of Data Distributed on the Sphere, Astrophysical Journal, 622, 759

Hauser, M. G., Arendt, R. G., Kelsall, T., et al. 1998, The COBE Diffuse Infrared Background Experiment Search for the Cosmic Infrared Background. I. Limits and Detections, Astrophysical Journal, 508, 25

Heald, G. & LOFAR Collaboration. 2014, in American Astronomical Society Meeting Abstracts, Vol. 223, American Astronomical Society Meeting Abstracts 223

Hubble, E. 1929, A Relation between Distance and Radial Velocity among Extra-Galactic Nebulae, Proceedings of the National Academy of Science, 15, 168

Huchra, J. P., Macri, L. M., Masters, K. L., et al. 2012, The 2MASS Redshift Survey Description and Data Release, Astrophysical Journal, Supplement, 199, 26

Jones, M. & Lambourne, J. 2003, Galaxies and Cosmology (Cambridge University Press)

Kalus, B., Schwarz, D. J., Seikel, M., & Wiegand, A. 2013, Constraints on anisotropic cosmic expansion from supernovae, Astronomy and Astrophysics, 553, A56

Kashlinsky, A., Atrio-Barandela, F., Kocevski, D., & Ebeling, H. 2008, A Measurement of Large-Scale Peculiar Velocities of Clusters of Galaxies: Results and Cosmological Implications, Astrophysical Journal, Letters, 686, L49

Kothari, R., Naskar, A., Tiwari, P., Nadkarni-Ghosh, S., & Jain, P. 2013, Dipole anisotropy in sky brightness and source count distribution in radio NVSS data, ArXiv e-prints 1307.1947

Maartens, R. 2011, Is the Universe homogeneous?, Royal Society of London Philosophical Transactions Series A, 369, 5115

Maller, A. H., McIntosh, D. H., Katz, N., & Weinberg, M. D. 2003, The Clustering Dipole of the Local Universe from the Two Micron All Sky Survey, Astrophysical Journal, Letters, 598, L1

Osborne, S. J., Mak, D. S. Y., Church, S. E., & Pierpaoli, E. 2011, Measuring the Galaxy Cluster Bulk Flow from WMAP Data, Astrophysical Journal, 737, 98

Paciesas, W. S., Meegan, C. A., Pendleton, G. N., et al. 1999, The Fourth BATSE Gamma-Ray Burst Catalog (Revised), Astrophysical Journal, Supplement, 122, 465

Peebles, M. 1980, The Large-Scale Structure of the Universe (Princeton University Press)

Peebles, P. J. E. & Wilkinson, D. T. 1968, Comment on the Anisotropy of the Primeval Fireball, Physical Review, 174, 2168

Penzias, A. A. & Wilson, R. W. 1965, A Measurement of Excess Antenna Temperature at 4080 Mc/s., Astrophysical Journal, 142, 419

Pilkington, J. D. H. & Scott, J. F. 1965, A survey of radio sources between declinations 20 deg and 40 deg, Memoirs of the RAS, 69, 183

Planck Collaboration, Adam, R., Ade, P. A. R., et al. 2015a, Planck 2015 results. I. Overview of products and scientific results, ArXiv e-prints

Planck Collaboration, Adam, R., Ade, P. A. R., et al. 2015b, Planck 2015 results. VIII. High Frequency Instrument data processing: Calibration and maps, ArXiv e-prints

Planck Collaboration, Ade, P. A. R., Aghanim, N., et al. 2014a, Planck 2013 results. XVI. Cosmological parameters, Astronomy and Astrophysics, 571, A16

Planck Collaboration, Ade, P. A. R., Aghanim, N., et al. 2014b, Planck intermediate results. XIII. Constraints on peculiar velocities, Astronomy and Astrophysics, 561, A97

Planck Collaboration, Ade, P. A. R., Aghanim, N., et al. 2015c, Planck 2015 results. XIII. Cosmological parameters, ArXiv e-prints

Planck Collaboration, Aghanim, N., Armitage-Caplan, C., et al. 2014c, Planck 2013 results. XXVII. Doppler boosting of the CMB: Eppur si muove, Astronomy and Astrophysics, 571, A27

Rengelink, R. B., Tang, Y., de Bruyn, A. G., et al. 1997, The Westerbork Northern Sky Survey (WENSS), I. A 570 square degree Mini-Survey around the North Ecliptic Pole, Astronomy and Astrophysics, Supplement, 124, 259

Rowan-Robinson, M., Sharpe, J., Oliver, S. J., et al. 2000, The IRAS PSCz dipole, Monthly Notices of the RAS, 314, 375

Rubart, M. 2012, Master thesis: Cosmology with upcoming radio continuum surveys: Analysing and modifying European Square Kilometre Array Design Study Simulated Skies. (Universität Bielefeld)

Rubart, M., Bacon, D., & Schwarz, D. J. 2014, Impact of local structure on the cosmic radio dipole, Astronomy and Astrophysics, 565, A111

Rubart, M. & Schwarz, D. J. 2013, Cosmic radio dipole from NVSS and WENSS, Astronomy and Astrophysics, 555, A117

Saunders, W., Sutherland, W. J., Maddox, S. J., et al. 2000, The PSCz catalogue, Monthly Notices of the RAS, 317, 55

Schwarz, D. J., Bacon, D., Chen, S., et al. 2015, Testing foundations of modern cosmology with SKA all-sky surveys, ArXiv e-prints

Singal, A. K. 2011, Large Peculiar Motion of the Solar System from the Dipole Anisotropy in Sky Brightness due to Distant Radio Sources, Astrophysical Journal, Letters, 742, L23

Singal, A. K. 2014, Comment on "Cosmic radio dipole from NVSS and WENSS", Astronomy and Astrophysics, 568, A63

Skrutskie, M. F., Cutri, R. M., Stiening, R., et al. 2006, The Two Micron All Sky Survey (2MASS), Astronomical Journal, 131, 1163

Slipher, V. M. 1917, Nebulae, Proceedings of the American Philosophical Society, 56, 403

Sparke, L. & Gallagher, J. 2000, Galaxies in the Universe: An Introduction (Cambridge University Press)

Tiwari, P. & Jain, P. 2015, Dipole anisotropy in integrated linearly polarized flux density in NVSS data, Monthly Notices of the RAS, 447, 2658

Tully, R. B., Courtois, H., Hoffman, Y., & Pomarède, D. 2014, The Laniakea supercluster of galaxies, Nature, 513, 71

Tully, R. B., Courtois, H. M., Dolphin, A. E., et al. 2013, Cosmicflows-2: The Data, Astronomical Journal, 146, 86

Tully, R. B. & Fisher, J. R. 1977, A new method of determining distances to galaxies, Astronomy and Astrophysics, 54, 661

Varenius, E., Conway, J. E., Martí-Vidal, I., et al. 2015, Subarcsecond international LOFAR radio images of the M82 nucleus at 118 MHz and 154 MHz, Astronomy and Astrophysics, 574, A114

Watkins, R. & Feldman, H. A. 2015, Large-scale bulk flows from the Cosmicflows-2 catalogue, Monthly Notices of the RAS, 447, 132

Watkins, R., Feldman, H. A., & Hudson, M. J. 2009, Consistently large cosmic flows on scales of $100h^{-1}$Mpc: a challenge for the standard ΛCDM cosmology, Monthly Notices of the RAS, 392, 743

Wilman, R. J., Miller, L., Jarvis, M. J., et al. 2008, A semi-empirical simulation of the extragalactic radio continuum sky for next generation radio telescopes, Monthly Notices of the RAS, 388, 1335

Wright, E. L., Eisenhardt, P. R. M., Mainzer, A. K., et al. 2010, The Wide-field Infrared Survey Explorer (WISE): Mission Description and Initial On-orbit Performance, Astronomical Journal, 140, 1868

Yoon, M., Huterer, D., Gibelyou, C., Kovács, A., & Szapudi, I. 2014, Dipolar modulation in number counts of WISE-2MASS sources, Monthly Notices of the RAS, 445, L60